



1 **The Human Brain Connectome Weighted by the Myelin Content**  
2 **and Total Intra-Axonal Cross-Sectional Area of White Matter**  
3 **Tracts**

4  
5 **Short title:**  
6

7 Mark C. Nelson<sup>1,2</sup>, Jessica Royer<sup>1,2</sup>, Wen Da Lu<sup>2,3</sup>, Ilana R. Leppert<sup>2</sup>, Jennifer S.W. Campbell<sup>2</sup>,  
8 Simona Schiavi<sup>4</sup>, Hyerang Jin<sup>1,2</sup>, Shahin Tavakol<sup>1,2</sup>, Reinder Vos de Wael<sup>1,2</sup>, Raul Rodriguez-  
9 Cruces<sup>1,2</sup>, G. Bruce Pike<sup>5</sup>, Boris C. Bernhardt<sup>1,2</sup>, Alessandro Daducci<sup>4</sup>, Bratislav Misic<sup>1,2</sup>, and  
10 Christine L. Tardif<sup>1,2,3</sup>

11 *<sup>1</sup>Department of Neurology and Neurosurgery, McGill university, Montreal, QC, Canada. <sup>2</sup>McConnell Brain Imaging Centre, Montreal*

12 *Neurological Institute and Hospital, Montreal, QC, Canada. <sup>3</sup>Department of Biomedical Engineering, McGill University, Montreal, QC, Canada.*

13 *<sup>4</sup>Department of Computer Science, University of Verona, Verona, Italy. <sup>5</sup>Hotchkiss Brain Institute and Departments of Radiology and Clinical*  
14 *Neuroscience, University of Calgary, Calgary, Canada.*

15

16 Corresponding Author: Mark C Nelson, [mark.nelson3@mail.mcgill.ca](mailto:mark.nelson3@mail.mcgill.ca)

17

18 Keywords: connectomics; network neuroscience; structural connectivity; functional connectivity;  
19 white matter; myelin; microstructure-weighted imaging

20

21 **ABSTRACT**

22 A central goal in neuroscience is the development of a comprehensive mapping between  
23 structural and functional brain features which facilitates mechanistic interpretation of brain  
24 function. However, the interpretability of structure-function brain models remains limited by a

25 lack of biological detail. Here, we characterize human structural brain networks weighted by  
26 multiple white matter microstructural features including total intra-axonal cross-sectional area  
27 and myelin content. We report edge-weight-dependent spatial distributions, variance, small-  
28 worldness, rich club, hubs, as well as relationships with function, edge length and myelin.  
29 Contrasting networks weighted by the total intra-axonal cross-sectional area and myelin content  
30 of white matter tracts, we find opposite relationships with functional connectivity, an edge-  
31 length-independent inverse relationship with each other, and the lack of a canonical rich club in  
32 myelin-weighted networks. When controlling for edge length, networks weighted by either  
33 fractional anisotropy, radial diffusivity or neurite density show no relationship with whole-brain  
34 functional connectivity. We conclude that the co-utilization of structural networks weighted by  
35 total intra-axonal cross-sectional area and myelin content could improve our understanding of the  
36 mechanisms mediating the structure-function brain relationship.

37

## 38 **AUTHOR SUMMARY**

39 For computational network models to provide mechanistic links between brain structure and  
40 function, they must be informed by networks in which edge weights quantify structural features  
41 relevant to brain function. Here, we characterized several weighted structural networks capturing  
42 multiscale features of white matter connectivity including total intra-axonal cross-sectional area  
43 and myelin density. We describe these networks in terms of edge weight distribution, variance  
44 and network topology, as well as their relationships with each other, edge length and function.  
45 Overall, these findings support the joint use of structural networks weighted by the total intra-  
46 axonal cross-sectional area and myelin content of white matter tracts in structure-function

47 models. This thorough characterization serves as a benchmark for future investigations of  
48 weighted structural brain networks.

49

50

## 51 **INTRODUCTION**

52 The quest to relate human structural and functional brain networks spans the spectrum of spatial  
53 scale and repertoire of data modalities absolutely. At the macroscale, the human brain can be  
54 modeled as an anatomical network of discrete neuronal populations (nodes) interconnected by  
55 white matter fibers (edges) (Sporns, 2011). Coordinated spatiotemporal patterns of neuronal  
56 activity unfolding upon this structural backbone are fine-tuned by white matter microstructure  
57 (Hodgkin & Huxley, 1952; Huxley & Stämpfli, 1949; Moore et al., 2020; Pumphrey & Young,  
58 1938) and form the basis of cognition and behavior (Biswal et al., 1995; Greicius et al., 2003;  
59 Hampson et al., 2006; Liégeois et al., 2019; S. M. Smith et al., 2009; Martijn P. Van Den Heuvel  
60 et al., 2009). Increasingly, MRI facilitates *in vivo* measurement of multi-scale properties of both  
61 brain structure (e.g., (Alexander et al., 2019; Drakesmith et al., 2019; Jeurissen et al., 2017;  
62 Mancini et al., 2020)) and function (e.g., (Finn et al., 2019; Friston, 2011; Gordon et al., 2017;  
63 Liu et al., 2022)). Diffusion MRI streamline tractography and resting-state functional MRI are  
64 often respectively used to estimate structural and functional connectivity (SC & FC) networks.  
65 Network science provides a framework to bring these fundamentally different substrates into a  
66 common space where their features can be quantified (Fornito et al., 2016; Sporns, 2010; Suárez  
67 et al., 2020) and used to probe the mechanisms mediating human brain function (e.g., (Cabral et  
68 al., 2017; Fornito et al., 2015)).

69  
70 SC network edges can be weighted by a range of MRI-derived metrics quantifying white matter  
71 microstructural features relevant to brain function including: voxel-level estimates of tissue  
72 diffusivity (e.g., (Caeyenberghs et al., 2016)), neurite density (H. Zhang et al., 2012), axon  
73 diameter distributions (Alexander et al., 2010; Assaf et al., 2008), myelin content (Heath et al.,  
74 2018; Mancini et al., 2020), and the g-ratio (ratio of inner/outer diameters of myelinated axons)  
75 (Stikov et al., 2011, 2015); as well as tract/bundle-level measures of axonal cross-sectional area  
76 (Daducci, Dal Palù, et al., 2015; R. E. Smith et al., 2015). Subsets of these metrics have been  
77 investigated using a microstructure-weighted connectomics approach (Boshkovski et al., 2021;  
78 Caeyenberghs et al., 2016; Deligianni et al., 2016; Frigo et al., 2020; Mancini et al., 2018;  
79 Messaritaki et al., 2021; Schiavi et al., 2020; M. P. van den Heuvel et al., 2010; Martijn P. van  
80 den Heuvel & Sporns, 2011; F. C. Yeh et al., 2016). We aim to extend this work by providing a  
81 comprehensive assessment of the fundamental characteristics of a range of standard and state-of-  
82 the-art weighted structural brain networks including a network weighted by myelin.

83  
84 The networks considered here can be grouped into two classes: those computed with tractometry  
85 (S Bells et al., 2011) and those computed directly from the streamline weights in a tractogram  
86 i.e., streamline-specific. We consider three examples of the latter: (1) the number of streamlines  
87 (NoS); and two methods which optimize the streamline weights in a tractogram to increase  
88 specificity for white matter structural features (2) spherical-deconvolution informed filtering of  
89 tractograms (SIFT2) (R. E. Smith et al., 2015) and (3) convex optimization modeling for  
90 microstructure informed tractography (COMMIT) (Daducci et al., 2013; Daducci, Dal Palù, et  
91 al., 2015). SIFT2 and COMMIT were designed to overcome known limitations of streamline

92 counts (Girard et al., 2014; Jones, 2010; Jones et al., 2013). While the edge weights in all three  
93 networks generally capture white matter features relevant to connection strength, SIFT2 and  
94 COMMIT more specifically quantify the total intra-axonal cross-sectional area of white matter  
95 tracts (henceforth referred to as “edge caliber”). To date, COMMIT and SIFT2 have not been  
96 compared to NoS with uniform connection density (Frigo et al., 2020; Schiavi et al., 2020; C. H.  
97 Yeh et al., 2016). Thus, it remains unclear how the edge weights themselves affect network  
98 topology.

99  
100 In contrast, tractometry allows network edge weights to be derived from any volumetric brain  
101 image that is co-registered to the tractogram. This increase in methodological flexibility comes at  
102 the expense of anatomical specificity. Tractometry is unable to resolve the separate contributions  
103 of individual fiber populations to the aggregate value of a voxel. Given that an estimated ~90%  
104 of white matter voxels at typical diffusion MRI resolutions (~2mm) contain multiple fiber  
105 populations (Jeurissen et al., 2012), the quantitative link between white matter microstructure  
106 and essentially all tractometry-derived edge weights is biased by partial volume effects.

107  
108 In this work, tractometry is combined with a diffusion tensor model (Basser, 1995; Basser et al.,  
109 1994) to derive networks weighted by FA (fractional anisotropy) and RD (radial diffusivity),  
110 which respectively quantify the degree of diffusion anisotropy (i.e., directional dependence) and  
111 diffusion magnitude perpendicular to the major axis. The crossing fiber problem described above  
112 is also known to limit the ability of diffusion tensor models to quantify white matter features (De  
113 Santis et al., 2014; Jacques Donald Tournier et al., 2011). Additional tractometry networks  
114 examined here include a network weighted by ICVF (intracellular volume fraction) computed

115 with NODDI (Neurite Orientation Dispersion and Density Imaging) (H. Zhang et al., 2012), as  
116 well as a network weighted by the longitudinal relaxation rate  $R_1$  ( $1/T_1$ ) derived from a  
117 quantitative  $T_1$  map. The edge weights in this network are myelin-weighted as  $R_1$  has been  
118 shown to correlate with histology-derived myelin content (Mancini et al., 2020; Mottershead et  
119 al., 2003).

120  
121 This characterization of weighted structural brain networks is carried out as follows: (1) within-  
122 network features of edge weight distribution and variance; (2) edgewise relationships with FC,  
123 edge length and myelin ( $R_1$ ); and (3) topological features of small-worldness, rich club and  
124 network hubs. Importantly, uniform binary connectivity is enforced across all weighted network  
125 variants i.e., the underlying binary connectivity map is identical. This allows the edge weights  
126 themselves to drive the characterization.

127

128

## 129 **RESULTS**

130 In 50 healthy adults (27 men;  $29.54 \pm 5.62$  years; 47 right-handed), structural brain networks were  
131 estimated from multi-shell diffusion MRI data with probabilistic tractography. Each subject's  
132 structural network was used to compute 8 SC networks (**Table 1**) in which edges were weighted  
133 by: NoS, SIFT2, COMMIT, FA, RD, ICVF,  $R_1$  and LoS (edge length computed as the mean  
134 length of streamlines). NoS, SIFT2, COMMIT and LoS correspond to streamline-specific  
135 metrics, whereas networks weighted by FA, RD, ICVF and  $R_1$  were computed using tractometry.  
136 The edge weights in NoS, SIFT2 and COMMIT networks were normalized by node volume.  
137 Additionally, a static FC network was derived for each subject by zero-lag Pearson cross-

138 correlation of nodewise resting-state time series. Unless otherwise stated, all results shown  
 139 correspond to networks parcellated with the Schaefer-400 cortical atlas (Schaefer et al., 2018)  
 140 and include 14 subcortical nodes.  
 141

<u>Short name</u>	<u>Long name</u>	<u>Method</u>	<u>Data source</u>	<u>Interpretation</u>
<b>LoS</b>	Length of Streamlines	streamline-specific	diffusion MRI	Mean length of the streamlines connecting two nodes
<b>NoS</b>	Number of Streamlines	streamline-specific	diffusion MRI	Number of streamlines connecting two nodes; connection strength
<b>SIFT2</b>	Spherical-deconvolution Informed Filtering of Tractograms	streamline-specific	diffusion MRI	Fiber density from spherical deconvolution summed across streamlines; connection strength
<b>COMMIT</b>	Convex Optimization Modeling for Microstructure Informed Tractography	streamline-specific	diffusion MRI	Total intra-axonal cross-sectional area summed across streamlines; connection strength
<b>R<sub>1</sub></b>	longitudinal relaxation rate	tractometry	multi-modal (diffusion + relaxometry)	$R_1=1/T_1$ ; index of tissue myelin content
<b>FA</b>	Fractional Anisotropy	tractometry	diffusion MRI	Diffusion directional dependence
<b>RD</b>	Radial Diffusivity	tractometry	diffusion MRI	Diffusion perpendicular to the principal axis
<b>ICVF</b>	Intra-Cellular Volume Fraction	tractometry	diffusion MRI	Neurite density

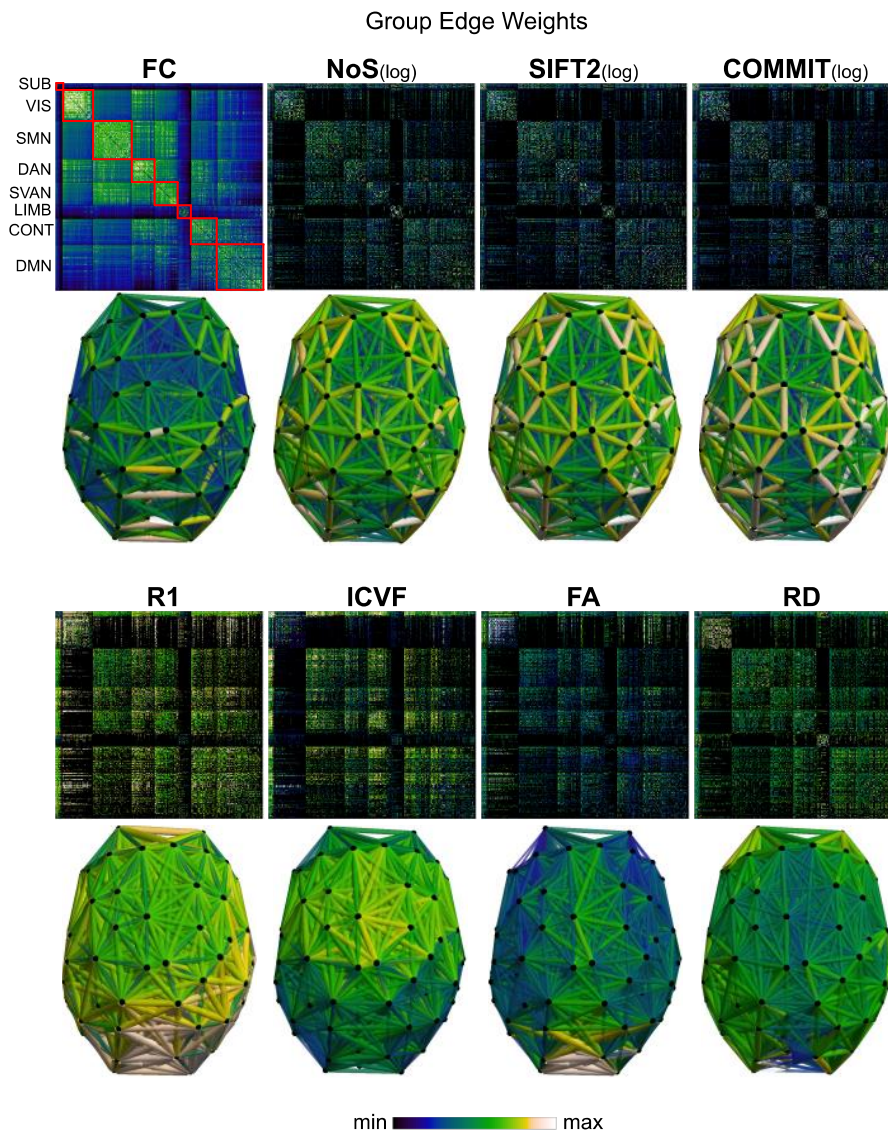
142 Table 1. Summary of structural network weights.

143  
 144

### 145 *Structural Brain Networks Vary in the Distribution of Their Edge Weights*

146 Group-level networks weighted by NoS, SIFT2 and COMMIT show spatially distributed patterns  
 147 of high magnitude edge weights and noticeably accentuate within-module connectivity (**Figure**  
 148 **1**). Modules correspond to the 7-canonical resting-state networks (Thomas Yeo et al., 2011) plus  
 149 the subcortex. These patterns are hallmarks of FC networks and are observed in the FC network  
 150 shown here. The contrast between high and low magnitude edge weights is most evident in  
 151 COMMIT. By comparison, the spatial variation of edge weight distribution in the tractometry

152 networks is smoother with more pronounced regional concentrations.  $R_1$  is highest in the edges  
 153 connecting the visual module to itself and to the rest of the brain; and lowest within the  
 154 subcortex and between the subcortical and limbic modules. The surface plot shows the highest  
 155 concentration of  $R_1$  in the white matter projections of posterior cortical regions.  
 156



157  
 158 **Figure 1.** Edge Weight Spatial Distribution. Connectivity matrices of group-level edge weights for FC  
 159 (functional connectivity), NoS (number of streamlines), SIFT2 (spherical-deconvolution informed filtering  
 160 of tractograms), COMMIT (convex optimization modeling for microstructure informed tractography),  $R_1$

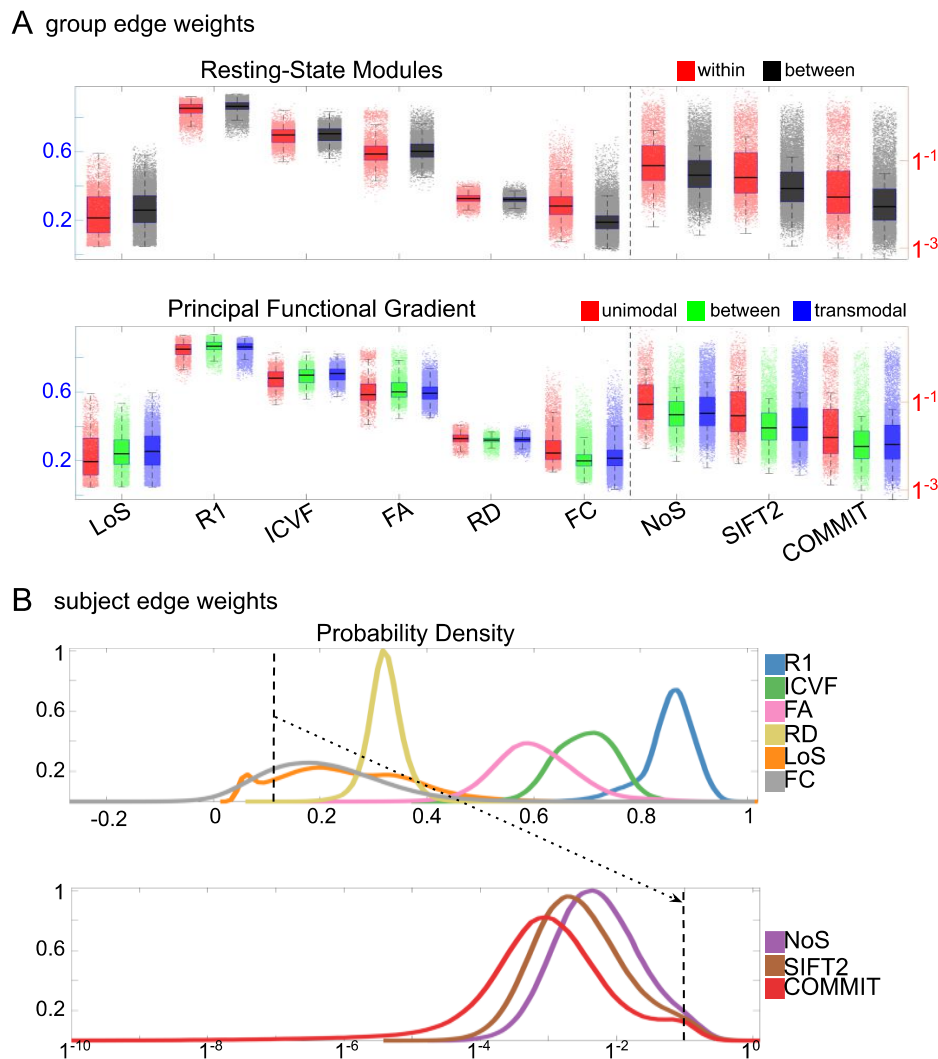


161 *(longitudinal relaxation rate), ICVF (intra-cellular volume fraction), FA (fractional anisotropy), RD*  
162 *(radial diffusivity) and LoS (mean length of streamlines). Each network is composed of 414 nodes as*  
163 *defined by the Schaefer-400 cortical parcellation and 14 subcortical ROIs. Nodes are grouped into the*  
164 *canonical resting state modules (Thomas Yeo et al., 2011) plus the subcortex: SUB (subcortex), VIS*  
165 *(visual), SMN (somatomotor), DAN (dorsal attention), SVAN (salience ventral attention), LIMB (limbic),*  
166 *CONT (control), and DMN (default mode). 3D cortical surfaces (shown below) of group-level edge*  
167 *weights in the Schaefer-100 parcellation generated with BrainNet Viewer (Xia et al., 2013). Edge*  
168 *diameter and color indicate weight magnitude. The edge weights in NoS, SIFT2 and COMMIT networks*  
169 *were  $\log_{10}$  transformed for visualization.*

170

171 Group-level edge weight distributions are summarized with respect to two important  
172 organizational patterns of brain function (**Figure 2A**): within and between resting state modules  
173 (Thomas Yeo et al., 2011); and along the principal functional gradient (Margulies et al., 2016).  
174 NoS, SIFT2 and COMMIT mirror FC in both plots with greater edge weight magnitude within  
175 module, especially within unimodal modules.  $R_1$ , ICVF, FA and RD generally mirror LoS with  
176 the reverse trend: higher between module and lowest in unimodal modules. This suggests that  
177 tractometry-derived networks may be influenced by edge length to a greater extent.

178



179

180 **Figure 2.** Edge Weight Distribution. (A) Distribution of group-level edge weights binned by: (top) within  
 181 and between module; (bottom) unimodal, transmodal and between. Unimodal is defined as the VIS and  
 182 SMN modules. Transmodal is defined as the DMN, CONT, DAN and SVAN modules. (B) Probability  
 183 density of pooled subject-level edge weight distributions. R<sub>1</sub>, ICVF, FA, RD, LoS and FC are shown on a  
 184 linear x-axis (top), and NoS, SIFT2 and COMMIT are shown on a logarithmic x-axis (bottom). All  
 185 networks were normalized to the range [0 1] by dividing by the subject-level max for visualization.

186

187 Subject-level edge weight distributions in R<sub>1</sub>, ICVF, FA and RD are near-normal and network-  
 188 specific (**Figure 2B**). They differ in both the magnitude (R<sub>1</sub> > ICVF > FA > RD) and dynamic  
 189 range (FA & ICVF > R<sub>1</sub> & RD) of their edge weights. In contrast, NoS, SIFT2 and COMMIT  
 190 distributions are highly skewed and tend to be much lower in magnitude (dashed line). This

191 effect is greatest in COMMIT suggesting that the optimization performed by COMMIT exerts a  
192 stronger scaling effect than SIFT2. These results support the conclusion that the structural  
193 networks considered here quantify subsets of white matter features which are at least partially  
194 non-overlapping.

195

196

### 197 *Edge Weights in Streamline-Specific Networks Are More Variable*

198 Edge weight variance was quantified using the Quartile Coefficient of Dispersion (CQD) due to  
199 its robustness to outliers and skewed data. The CQD is computed from the 1<sup>st</sup> and 3<sup>rd</sup> quartiles as:

$$200 \text{CQD} = (Q_3 - Q_1) / (Q_3 + Q_1).$$

201

202 *Intra-subject* variance is roughly 2-fold greater in NoS, SIFT2 and COMMIT relative to LoS and  
203 FC; and an order of magnitude greater than R<sub>1</sub>, ICVF, FA and RD in all subjects (**Figure 3A**).

204 COMMIT is the highest overall. Subjects are more tightly clustered in all weighted SC networks,  
205 relative to FC: *intra-subject* CQD values span roughly a 4-fold greater range in FC. This

206 suggests that individual diversity of functional connectivity is not necessarily reflected in the  
207 variability of their structural networks. These patterns are repeated for *inter-subject* variance.

208 However, FC shows a small subset of highly variable edges with roughly 4-fold greater CQD

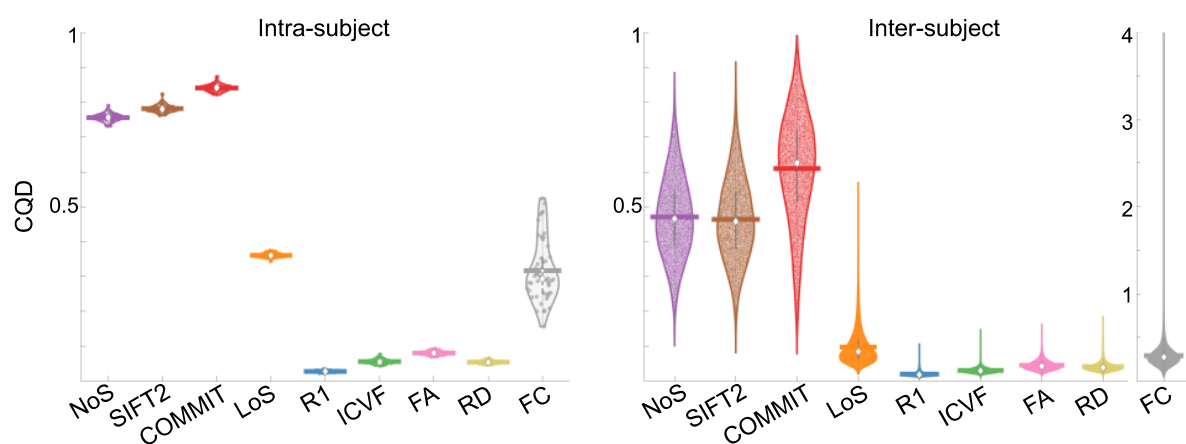
209 than the maximum values observed in COMMIT i.e., the most subject-specific connections are

210 functional. The very low edge weight variability in R<sub>1</sub>, ICVF, FA and RD is in part due to the

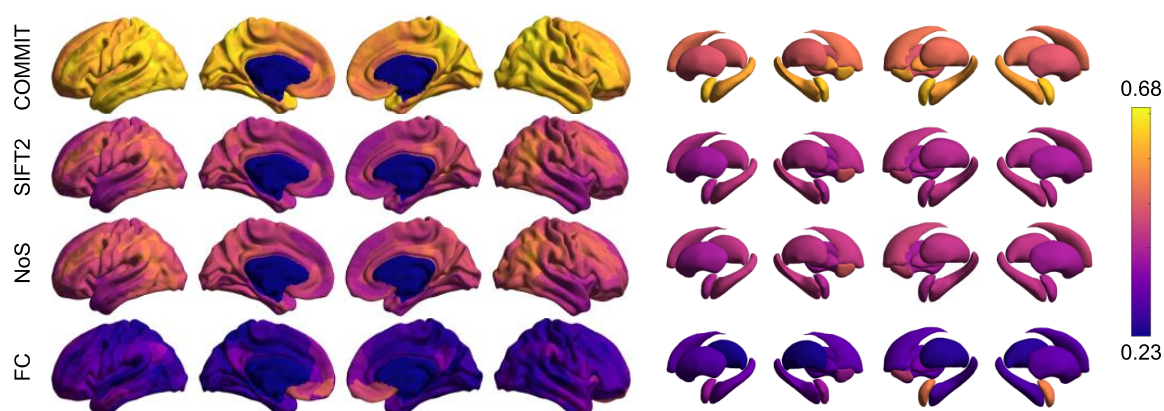
211 widespread blurring effect (partial voluming) resulting from the tractometry computation.

212

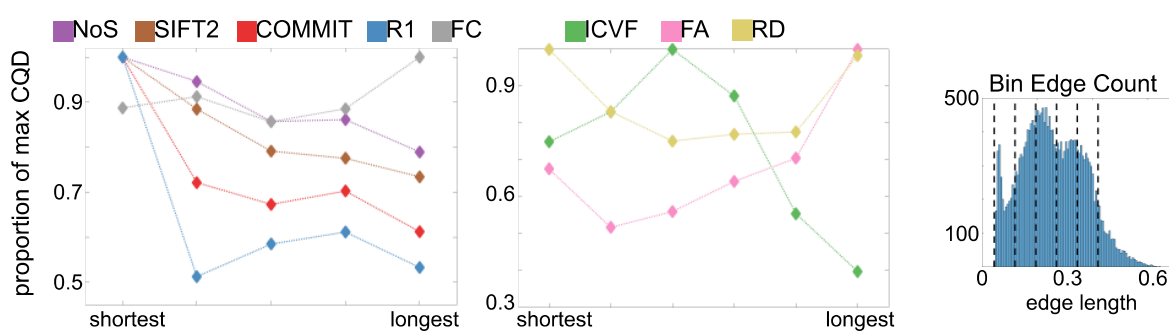
## A subject edge weight variability



## B edgewise mean inter-subject variance



## C group edge weight variance across edge length bins



213

214 **Figure 3. Edge Weight Variability.** Variability is quantified using the coefficient of quartile dispersion215 (CQD). (A) Violin distributions of *intra-subject* (left) and *inter-subject* (right) edge weight variance.216 Colored data points respectively correspond to individual subjects ( $N=50$ ) and edges ( $N=8549$ ). (B)

217 Surface projections of edgewise mean inter-subject variance for cortical nodes in the Schaefer-400

218 *parcellation (left) and 14 subcortical nodes (right). Cortical and subcortical surfaces were respectively*  
219 *generated with BrainSpace (Vos de Wael et al., 2020) and ENIGMA toolboxes (Larivière et al., 2021).*  
220 *(C) The proportion of within-network max CQD is shown across edge length bins for FC, NoS, SIFT2,*  
221 *COMMIT and  $R_1$  (left), as well as ICVF, FA and RD (middle). Edge weights are grouped into 6 bins*  
222 *according to edge length, as illustrated by the histogram (right). The edges of bins 1-5 were linearly*  
223 *spaced of width,  $w$ . The edges of the final bin were of width  $3w$ .*

224

225 In general, *inter-subject* edge weight variance is more spatially distributed in SC networks  
226 relative to FC (**Figure 3B**). COMMIT shows the highest mean CQD over the entire cortex and  
227 subcortex. NoS, SIFT2 and COMMIT all show lateral-medial and posterior-anterior cortical  
228 gradients. Mean CQD in FC shows the highest concentration in medial inferior frontal cortex and  
229 to a lesser extent, the expected pattern of high variance in association cortex. The most variable  
230 subcortical regions include the hippocampus, amygdala and accumbens.

231

232 Many features of brain networks (e.g., connection probability, weight magnitude) are known to  
233 vary with edge length. Here, we examined the relationship between edge weight variability and  
234 edge length by computing the CQD within subsets of group-level edge weights binned according  
235 to their edge length (**Figure 3C**). Edge weight variance in NoS, SIFT2, COMMIT and  $R_1$  is  
236 highest in the shortest edges and decreases with edge length. ICVF roughly follows the same  
237 pattern. FA and RD instead show the highest variability in the longest edges. Overall, the edge  
238 weights in streamline-specific SC networks (NoS, SIFT2 and COMMIT) show greater contrast  
239 both within and across subjects. SC networks show network-dependent relationships between  
240 edge weight variance and edge length. Shorter edges are more variable in myelin- and

241 connection strength-weighted networks, and longer edges are more variable in networks with  
242 edge weights derived from a diffusion tensor model.

243

244 To complement the above results, a supplemental analysis was performed using intraclass  
245 correlation to quantify edge weight variance within each edge weight (**Figure S9**).

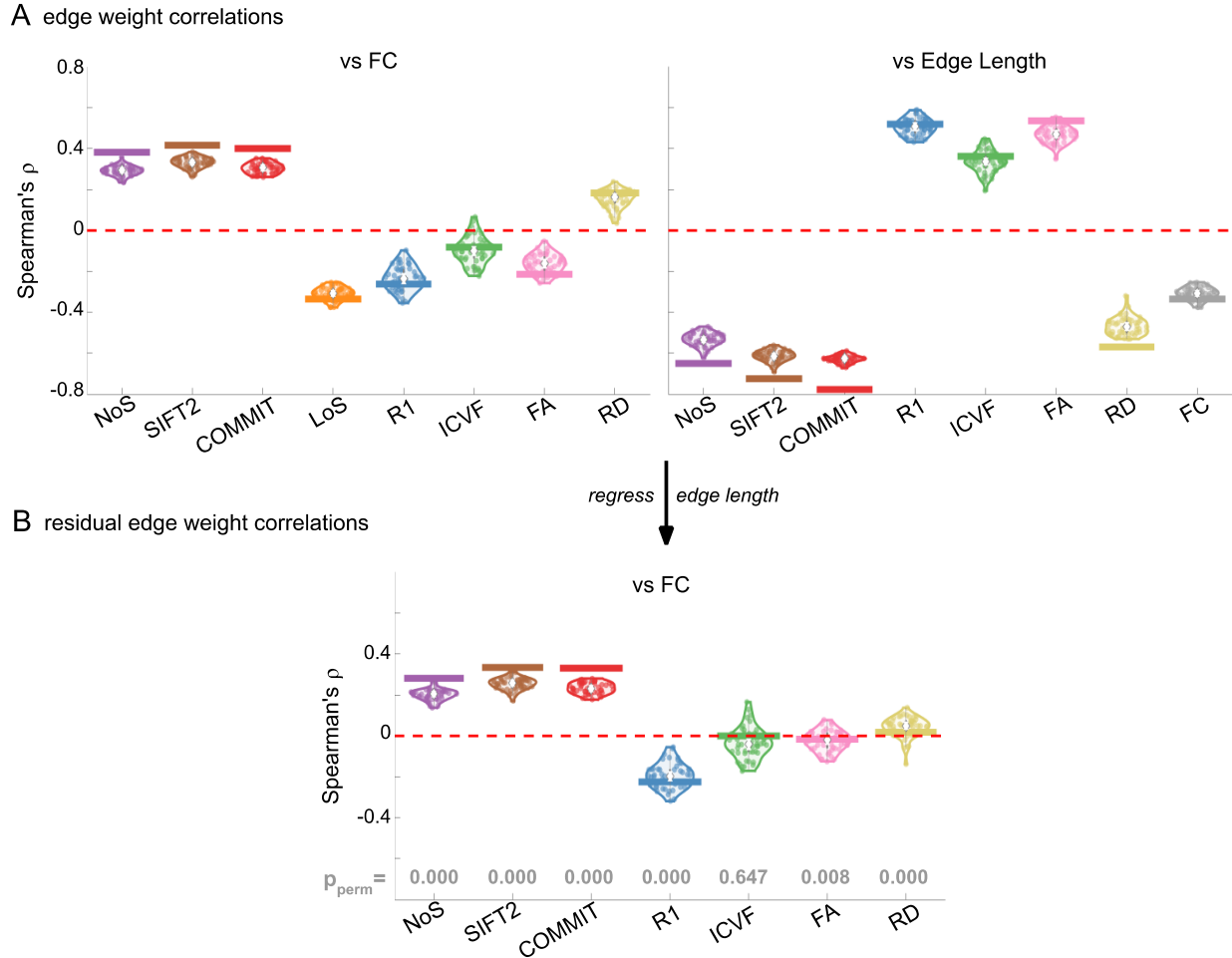
246

247

### 248 *Opposing Correlations with Function in Connection-Strength- & Myelin-Weighted Networks*

249 Shifting to inter-network edge weight relationships shows that SC networks are differentially  
250 related to FC (**Figure 4A**). Importantly, we also see that all brain networks (SC and FC) are  
251 strongly and differentially related to edge length at the subject and group levels. Correlations  
252 with edge length are negative for NoS, SIFT2, COMMIT, RD and FC; and positive for  $R_1$ ,  
253 ICVF, and FA. Correlation magnitude is strongest in group-level COMMIT ( $\rho \approx -0.8$ ). To  
254 account for this strong obscuring effect, we recomputed correlations using residual edge weights  
255 following linear regression of edge length (**Figure 4B**). NoS, SIFT2 and COMMIT remain  
256 positively associated (group-level  $\rho \approx 0.35$ ) and  $R_1$  remains negatively associated with FC  
257 (group-level  $\rho \approx -0.22$ ). Correlation magnitude was reduced following linear regression of edge  
258 length in all cases. ICVF, FA and RD are reduced to 0 suggesting that they may not be useful in  
259 modeling whole-brain FC. These results support the idea that  $R_1$ -weighted SC networks provide  
260 complementary information to NoS, SIFT2 and COMMIT about the brain structure-function  
261 relationship.

262



263

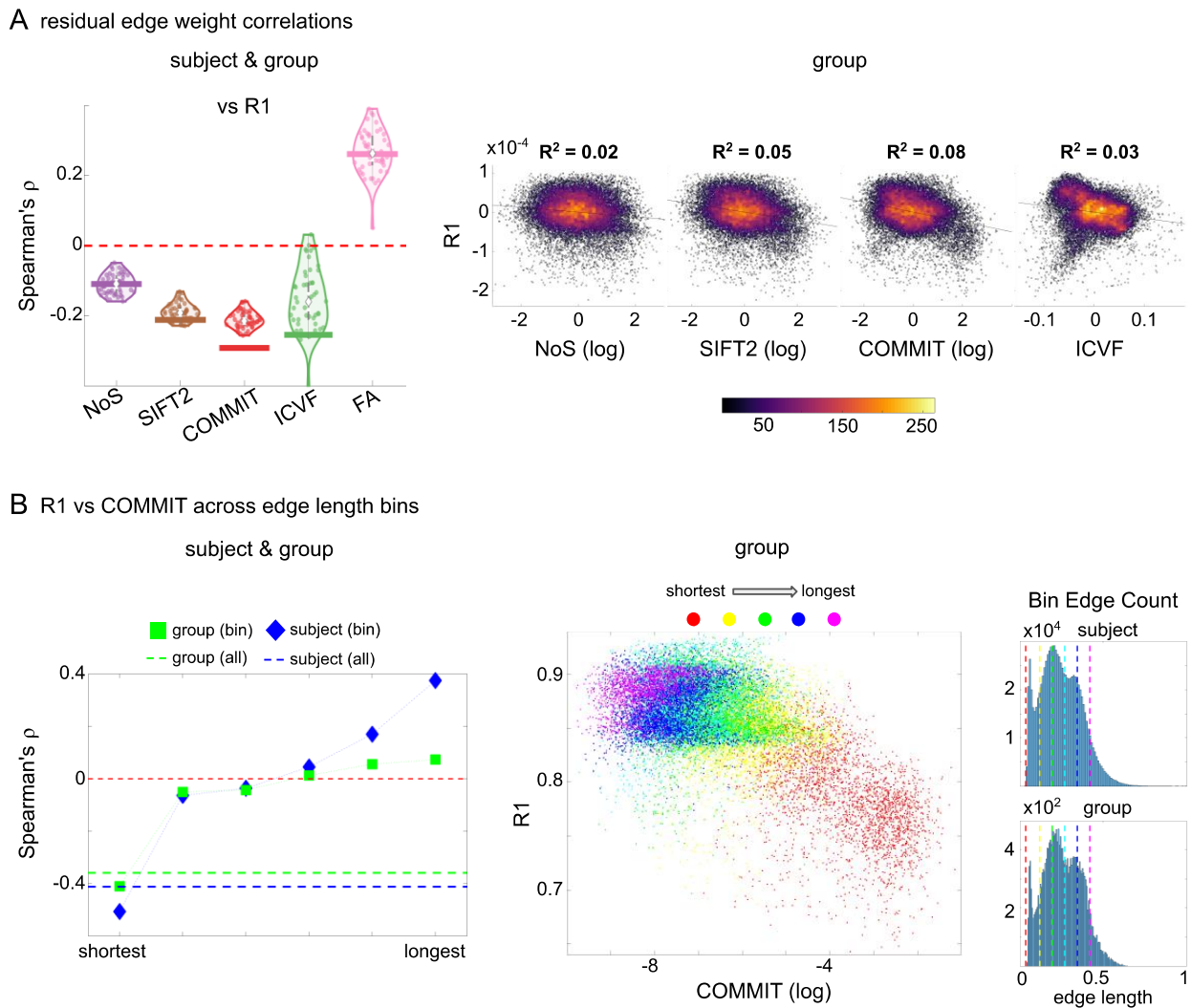
264 **Figure 4.** Edge Weight Correlations with FC and Edge Length. (A) Violin distributions of edgewise  
 265 Spearman's rank correlations of all networks with FC (left) and edge length (right). (B) Violin  
 266 distributions of edgewise Spearman's rank correlations of residual edge weights in all networks with  
 267 residual edge weights in FC. Residual edge weights were computed by linear regression of edge length.  
 268 Colored data points and bars respectively indicate subject-level and group-level correlations.  $P_{perm}$  gives  
 269 the one-sided p-value obtained from permutation testing (Figure S7).

270

271

272 **Edge Caliber and Myelin Content are Inversely Related**

273 Here, we ask how  $R_1$ , which we refer to as the myelin-weighted network, is related to the  
 274 connection-strength-weighted network COMMIT. Edge-length regressed residual edge weights  
 275 in NoS, SIFT2 and COMMIT show a negative association with  $R_1$  residuals for all subjects and  
 276 at the group level, which is strongest in COMMIT (group-level  $\rho \approx -0.29$ ) (**Figure 5A**). This  
 277 suggests an edge-length independent inverse relationship between white matter structural  
 278 features related to connection strength and myelin content.  
 279



280

281 **Figure 5. The Myelin-Dependence of Structural Brain Networks.** (A) Violin distributions (left) of  
 282 edgewise Spearman's rank correlations with the myelin-weighted network  $R_1$ . Residual edge weights are



283 compared following linear regression of edge length. Colored data points and bars respectively indicate  
284 subject-level and group-level correlations. Heat scatter plots (right) of group-level residual edge weights  
285 in  $R_1$  as a function of NoS (left), SIFT2 (left middle), COMMIT (right middle) and ICVF (right). The best  
286 fit linear curve is shown in black, and  $R^2$  (coefficient of determination) is reported. Data color indicates  
287 density. Permutation testing provided a one-sided  $p$ -value of  $P_{perm} = 0.000$  for all edgewise correlations  
288 (Figure S8). (B) Line plot (left) of edgewise Spearman's rank correlation of edge weights in  $R_1$  vs  
289 COMMIT across edge length bins. Group-level and subject-level are respectively shown in green and  
290 blue. The square and diamond markers connected by dotted lines show binned correlation values, and the  
291 horizontal dashed green and blue lines mark the correlation values for all edges pooled together. Scatter  
292 plot (middle) of group-level edge weights in  $R_1$  as a function of COMMIT with data points colored by bin  
293 identity. Histograms (right) illustrating subject- and group-level edge length bins.

294  
295 Computing correlations of edge weights (not residuals) within edge-length bins allows the  
296 inverse relationship between  $R_1$  and COMMIT to be traced to the shortest edges of the network  
297 (group  $\rho \approx -0.40$ , subject  $\rho \approx -0.50$ ). As edge length increases, this relationship is reduced to 0,  
298 then becomes strongly positive in the longest subject-level edges ( $\rho \approx 0.39$ ). The scatter plot of  
299 group-level  $R_1$  vs COMMIT (middle) shows decreasing COMMIT and increasing  $R_1$  with  
300 increasing edge length. All together, these results support an inverse relationship between the  
301 edge caliber and myelin content of a given white matter tract. This can be partly explained by the  
302 differential dependence of these structural features on edge length: longer tracts tend to be more  
303 myelinated with lower total intra-axonal cross-sectional area. However, this relationship is robust  
304 to controlling for edge length supporting an intrinsic dependence between these white matter  
305 features.

306

307 In addition, we show that our  $R_1$ -weighted network corresponds well with a previously reported  
308 (Boshkovski et al., 2021)  $R_1$ -weighted structural connectome (**Figure S13**).

309

310

### 311 *Divergent Small-Worldness, Hubness and Rich Club in Weighted Structural Networks*

312 In this final section, we apply network analysis tools (Rubinov & Sporns, 2010) based on graph  
313 theory (Fornito et al., 2013; Sporns, 2018) to group-level weighted SC networks. This facilitates

314 high-level interpretation of general features of network communication such as integrative vs

315 segregative processing and the economy of network organization. Although the high material

316 and metabolic cost of brain tissue naturally tends to favor local connectivity (high clustering),

317 short overall network path length is achieved through a small number of relatively expensive

318 long-range connections (Bullmore & Sporns, 2012). These edges and the nodes they interlink

319 form a densely connected network core known as the rich club (Martijn P. van den Heuvel &

320 Sporns, 2011). While the general proclivity for high local clustering gives rise to segregated

321 functional modules, the rich-club nodes act as network communication hubs supporting inter-

322 modular integration (Collin et al., 2014; de Reus & van den Heuvel, 2014; Griffa & Van den

323 Heuvel, 2018; Kim & Min, 2020; Martijn P. van den Heuvel & Sporns, 2013). Thus, small-world

324 network topology (high clustering and low path length) (Bassett & Bullmore, 2006, 2017)

325 supports both integrative and segregative processing at a minimum of wiring cost, and the

326 underlying scaffold of hub brain regions tend to show high centrality, low path length (high

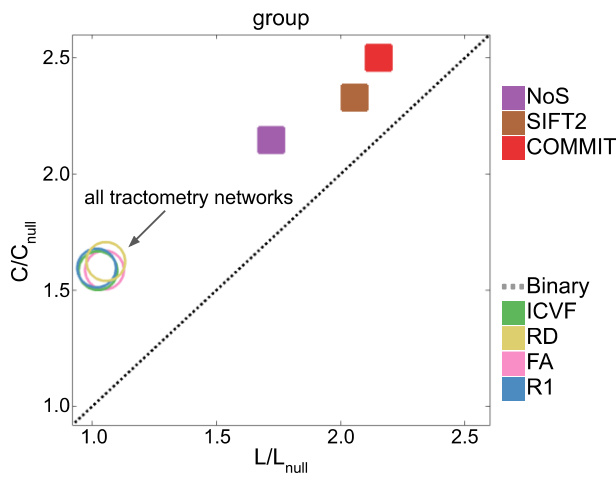
327 closeness) and low clustering (M. P. van den Heuvel et al., 2010).

328

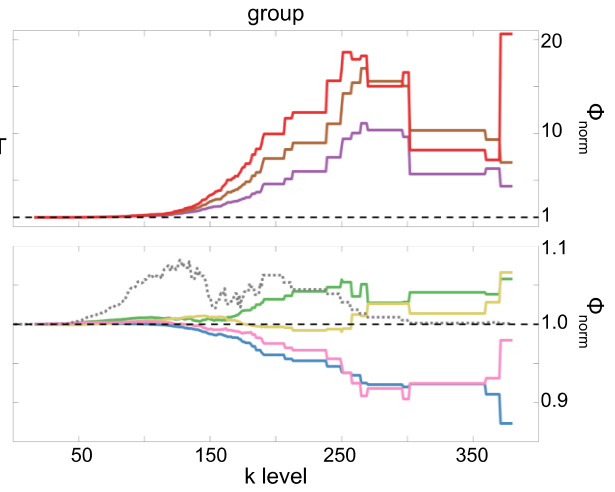
329 Here, we report normalized small-worldness, normalized rich-club curves and nodal hubness  
330 (**Figure 6**). Normalized small-worldness ( $S$ ) is computed as the quotient of normalized measures  
331 of clustering coefficient ( $C/C_{\text{null}}$ ) and path length ( $L/L_{\text{null}}$ ).

332

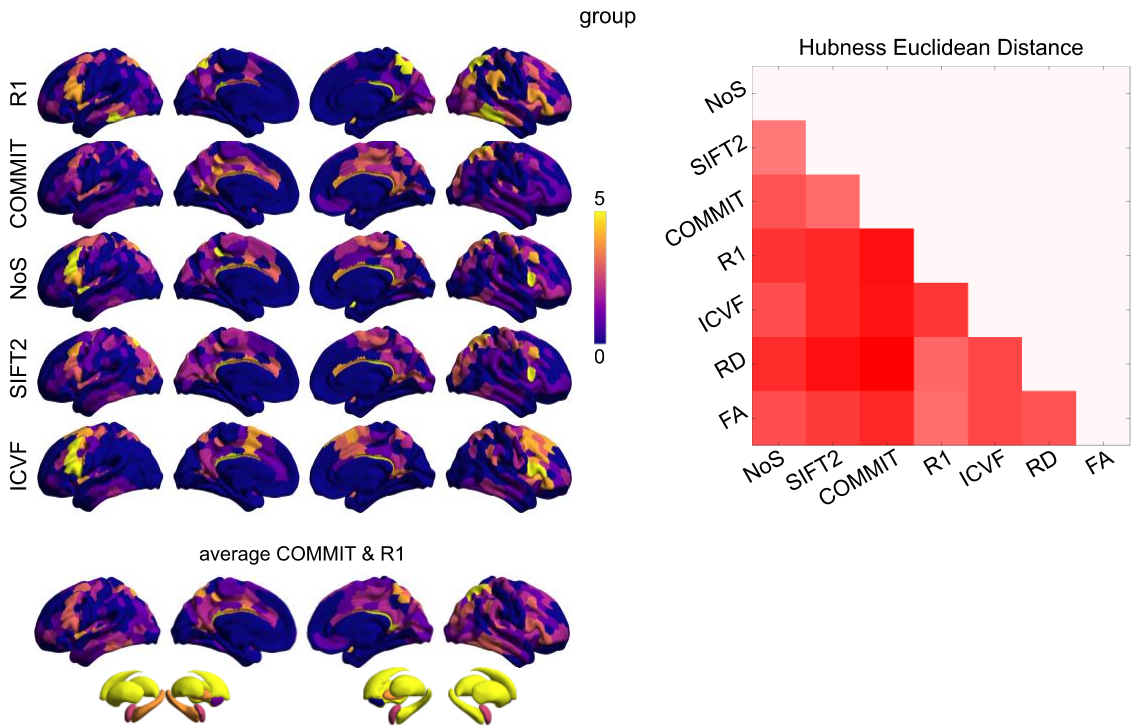
A normalized small-worldness



B normalized rich club



C normalized hubness



333

334 **Figure 6. Group-Level Network Topology.** (A) Small-worldness was estimated in all structural networks:

335 clustering coefficient was normalized within each node, averaged across nodes ( $C/C_{null}$ ), then plot as a

336 function of normalized characteristic path length ( $L/L_{null}$ ). Topology measures averaged across 50 degree

337 and strength preserving null networks were used for normalization. Networks above the identity line

338 (dotted black) are characterized by the small world attribute. Tractometry networks are indicated by the

339 arrow. (B) Normalized rich-club curves are shown for COMMIT, NoS and SIFT2 (top), as well as ICVF,

340 *RD, FA and R<sub>1</sub> (bottom). A single binary network (dotted gray line) is also shown (bottom) as binary*  
341 *connectivity was uniform across weighted networks. The normalized rich-club coefficient ( $\phi_{norm}$ ) was*  
342 *computed across the range of degree ( $k$ ) and normalized against 1000 null networks (degree preserving*  
343 *for binary and degree and strength preserving for weighted networks). A  $\phi_{norm}$  value  $> 1$  (horizontal*  
344 *dashed black lines) over a range of  $k$  indicates the presence of a rich club. (C) Nodewise hubness scores*  
345 *are projected onto Schaefer-400 cortical and 14-ROI subcortical surfaces. Scores (0-5) were computed*  
346 *for each node as +1 point for all nodes in top 20% strength, betweenness, closeness and eigenvector*  
347 *centrality, as well as bottom 20% clustering coefficient. The matrix (right) shows the Euclidean distance*  
348 *between all pairs of nodal hubness vectors.*

349

350 All group-level weighted SC networks show the normalized small-world property ( $S > 1$ ) of  
351 higher clustering and lower path length than would be expected by chance (**Figure 6A**). Small-  
352 worldness is highest in COMMIT ( $S \approx 2.5$ ) and lowest in R<sub>1</sub>, ICVF, FA and RD ( $S \approx 1.6$ ). In  
353 contrast, all weighted SC networks did not show a canonical rich club (**Figure 6B**). Relative to  
354 the tractometry and binary SC networks, the normalized rich-club coefficient ( $\phi_{norm}$ ) was much  
355 higher in magnitude in NoS, SIFT2 and COMMIT. A rich club was detected in these networks  
356 across a large range of degree ( $k$ ) levels ( $150 < k < 300$ ).  $\phi_{norm}$  was maximal at  $k \approx 265$  in  
357 COMMIT. A rich club was also detected across a similar range of  $k$  levels in ICVF and across  $k$   
358 in the range [250 300] for RD, albeit with much lower magnitude  $\phi_{norm}$ . However, no clear rich  
359 club was observed in R<sub>1</sub> or FA. In fact, the rich-club curves for these networks are roughly  
360 symmetric about the  $\phi_{norm} = 1$  line relative to COMMIT. A densely connected core was of course  
361 recovered in all weighted SC networks (uniform binary connectivity), but these results suggest  
362 that its interconnecting edges were consistently weaker than would be expected by chance in R<sub>1</sub>

363 and FA. By comparison, a rich club was observed in the binary SC network across the very large  
364 range of  $k$  [50 300]. This supports two important concepts: (1) SC network edge weights can  
365 provide an additional layer of information useful for refining the topology of binary SC; and (2)  
366 different methods for computing SC network edge weights yield diverse network topology.

367

368 Weighted SC networks show network-dependent spatial topology of hubness scores (**Figure**  
369 **6C**). The COMMIT and R1 averaged surface shows prominent hubs distributed throughout the  
370 brain including the fronto-parietal network. Nearly all of the subcortex showed a hubness score  
371 of 4 or greater in all networks. The Euclidean distance between hubness score vectors (right) was  
372 lower for COMMIT and SIFT2 than for either network with NoS. Of the streamline-specific  
373 networks, NoS was more similar to both R1 and IVCF. Overall, these results illustrate the  
374 considerable impact that edge weighting can have on network topology.

375

376

## 377 **DISCUSSION**

378 Structure-function brain models provide a flexible framework for investigating the mechanistic  
379 relationship between human brain structure and function *in vivo*, yet the interpretability of these  
380 models is currently limited by a lack of biological detail. Here, we assemble a thorough  
381 characterization of structural brain networks weighted by a range of quantitative MRI metrics  
382 capturing the macro- and microscopic features of white matter tracts. Notable trends included:  
383 (1) greater edge weight contrast and skewed (heavy-tailed) distributions in the streamline-  
384 specific networks NoS, SIFT2 and COMMIT; (2) whole-brain correlations with FC in networks  
385 weighted by connection strength (positive) and myelin (negative) which were robust to

386 controlling for edge length; (3) whole-brain inverse relationships with myelin for networks  
387 weighted by connection strength and neurite density independent of edge length; and (4) the  
388 absence of a rich club in  $R_1$  and FA networks. All weighted SC networks showed a strong spatial  
389 dependence and small-world architecture. Collectively, these results support the overall  
390 conclusion that SC networks weighted by edge caliber (e.g., SIFT2 and COMMIT) and myelin  
391 (e.g.,  $R_1$ ) can be used to quantify non-overlapping subsets of white matter structural features  
392 related to FC supporting their joint utilization in modeling function.

393

394

### 395 *Interpretable Measures of Connection Strength Provided by COMMIT and SIFT2*

396 A principal goal of this work is to identify what, if any, advantage over NoS is provided by the  
397 global optimization methods SIFT2 and COMMIT. NoS has previously been used to inform the  
398 strength of interregional coupling in computational models of function (e.g., (Honey et al.,  
399 2009)). However, important limitations restrict model interpretation. Besides suffering from a  
400 range of biases related to the position, size, shape and length of white matter tracts (Girard et al.,  
401 2014), NoS varies as a function of tracking parameters limiting its specificity for white matter  
402 structural features (Jones, 2010; Jones et al., 2013).

403

404 SIFT2 and COMMIT reportedly restore the quantitative link between connectome edge weights  
405 and white matter structural features related to connection strength. COMMIT and SIFT2 solve  
406 for the effective cross-sectional area (i.e., signal fraction) of each streamline using different  
407 approaches. COMMIT uses the global diffusion signal to optimize these values, whereas SIFT2  
408 seeks to fit the streamline density throughout the white matter to the fiber densities estimated

409 using spherical deconvolution. Thus, while both methods rely on the simplifying assumption that  
410 streamline features are invariant along their length, SIFT2 additionally requires that the estimates  
411 of fiber density derived from the fiber orientation distribution (FOD) are biologically accurate.

412

413 These networks also differ in the computation of their edge weights: SIFT2 is computed as the  
414 simple sum of streamline weights, whereas COMMIT is computed as the length-weighted-sum  
415 of streamline weights. Indeed, our analysis methods do not permit us to make strong claims as to  
416 the relationship between these methodological differences and our observed results, however we  
417 do show that both SIFT2 and COMMIT display comparable but not identical fundamental  
418 characteristics to NoS. This supports the use of SIFT2 or COMMIT in place of NoS as a measure  
419 of connection strength, which brings with it improved biological interpretability.

420

421

### 422 *Myelin Complements Connection Strength in Predicting FC*

423 Despite the differences between COMMIT, SIFT2 and NoS; our results indicate that their edge  
424 weights show roughly equivalent positive correlations with FC over the whole brain.  $R_1$  was  
425 negatively correlated with FC. Significant evidence indicates a link between cerebral myelin and  
426 FC including: a relationship between intracortical myelin and FC (Huntenburg et al., 2017;  
427 Wang et al., 2019); the prediction of cognition (Sonya Bells et al., 2017; Caeyenberghs et al.,  
428 2016) and FC-derived components (Messaritaki et al., 2021) using myelin-sensitive metrics; and  
429 a relationship between damaged myelin sheaths and greater conduction delays in multiple  
430 sclerosis (Sorrentino et al., 2022). At the cellular-level, myelin contributes to conduction velocity  
431 (Huxley & Stämpfli, 1949), metabolic support (Nave & Werner, 2014) and plasticity (Gibson et



432 al., 2018), all of which could be argued to support brain function. Myelin plasticity in particular  
433 can be described in terms of “activity-dependence”, whereby an increase in the functional  
434 activity of a given circuit stimulates cellular signaling cascades promoting greater myelination  
435 (Douglas Fields, 2015; Mount & Monje, 2017). Coupled with our results, this complex mix of  
436 functional roles supports the idea that structure-function models will be improved by integrating  
437 measures of myelin and connection strength.

438

439

#### 440 *An Opposing Relationship with Edge Length for Edge Caliber and Myelin Content*

441 When controlling for edge length, we found an inverse relationship between  $R_1$  and COMMIT  
442 over the whole brain in all subjects and at the group level. This suggests that the aggregate g-  
443 ratio (ratio of inner/outer diameters of myelinated axons) of a white matter tract may increase  
444 with edge caliber. At the cellular-level, the diameter of an axon and the thickness of its myelin  
445 sheath show nearly a linear relationship over a broad range of smaller diameter axons which  
446 becomes increasingly nonlinear as axon diameter increases (Berthold et al., 1983; Hildebrand &  
447 Hahn, 1978). In general, increasing axon diameter tends to outpace increasing myelin thickness  
448 i.e., g-ratio tends to increase with increasing axon caliber (Hildebrand & Hahn, 1978). Our  
449 findings suggest that this cellular-level principle may extend to the systems level: increases in  
450 edge caliber tend to outpace changes in the myelin content resulting in a concomitant increase in  
451 the g-ratio of white matter tracts.

452

453 We localized the inverse relationship between  $R_1$  and COMMIT to the shortest edges suggesting  
454 that the g-ratio was the highest in the shortest connections. This result is supported by a previous

455 imaging study showing the highest g-ratio in “local” connections (Mancini et al., 2018). In  
456 general, we found that  $R_1$  increased and COMMIT decreased with increasing edge length, which  
457 aligns with previously reported results of higher  $R_1$  and fewer streamlines for the white matter  
458 connections between transmodal regions (Boshkovski et al., 2021). Both of these trends fit well  
459 with theories of brain wiring economy in which the energetic cost of maintaining biological  
460 material increases with connection length (Bullmore & Sporns, 2012). This natural pressure acts  
461 to reduce the total axonal volume of longer white matter bundles. Increasing the myelin content  
462 of longer tracts comes at a cost as well, but this may be at least partially offset as increasing  
463 myelin content reduces the total membrane surface area along which expensive electrochemical  
464 gradients must be maintained (Bullmore & Sporns, 2012). Although, a cost-benefit analysis of  
465 the energetics of myelination concluded that the energetic cost of myelin maintenance outweighs  
466 any savings on action potentials (Harris & Attwell, 2012). This suggests that higher myelination  
467 of longer edges may be better explained as a mechanism to provide trophic support (Nave &  
468 Werner, 2014) to vital inter-regional connections (Martijn P. Van Den Heuvel et al., 2012) or to  
469 reduce conduction delays.

470  
471

### 472 ***Edge Weight Variance Decreases with Edge Length in Most Weighted Structural Networks?***

473 White matter features related to myelin content, connection strength and neurite density tend to  
474 become more consistent across tracts as tract length increases. Greater variability in the weights  
475 of the shortest connections could result from a higher proportion of false positive streamlines  
476 influencing these edge weights. For SIFT2 and COMMIT, streamline weight computation  
477 becomes increasingly unstable with decreasing length as fewer voxels contribute to the fit.

478 However, this result could also be explained more generally by contrasting the roles of shorter  
479 and longer connections in the brain. Shorter white matter tracts connect brain regions near each  
480 other in space e.g., within the same module. Just as we might expect the characteristics of  
481 smaller roads and streets (e.g., width, building materials, markings, signs, sidewalks, etc.) to vary  
482 by neighborhood and city, we might also expect the morphology of shorter white matter  
483 connections to change as the functional specialization of any given region or module changes.  
484 On the other hand, longer tracts (i.e., the freeways of the brain) may overlap more in both their  
485 functional role and morphological features relative to shorter connections, hence lower edge  
486 weight variability. Breaking with the above pattern, FA and RD showed the highest edge weight  
487 variance in the longest connections. Given that structural measures derived using a voxel-wise  
488 diffusion tensor model are particularly sensitive to the white matter “architectural paradigm”  
489 (Jones et al., 2013), these results suggest that white matter features related to fiber orientation  
490 and geometry actually diverge with increasing tract length. Note that we are unable to say  
491 decisively whether the edge weight variance measured in these structural and functional brain  
492 networks corresponds to true signal or noise. The inclusion of scan-rescan data (e.g., as in  
493 (Amico & Goñi, 2018)) could support stronger conclusions as to the source of this variability.

494

495

#### 496 ***The Absence of a Rich Club in Structural Networks Weighted by $R_1$ and FA***

497 Group-level  $R_1$  and FA did not show a normalized weighted rich club for any degree  $k$ . Higher  
498 myelination in the white matter tracts connecting rich club nodes has previously been reported  
499 (Collin et al., 2014); however, methodological differences limit comparability. A rich club has  
500 previously been reported in FA-weighted networks using similar methods to ours (Martijn P. van

501 den Heuvel & Sporns, 2011). The source of this disagreement could potentially be attributed to  
502 differences in our tractography algorithm, parcellation or null network computation.

503

504 In weighted rich-club detection, the identification of a densely connected core is independent of  
505 edge weight (depends only on node degree), but the designation of this subnetwork as a rich club  
506 requires that it contains a higher-than-chance proportion of the strongest edges from the full  
507 network. Indeed, this is the case over a broad range of degree  $k$  for COMMIT. Over the same  
508 range of  $k$ , the normalized rich-club curves for  $R_1$  and FA are inverted about the threshold value  
509 of 1 with respect to COMMIT. This implies that the subnetwork found at a given  $k$  in this range  
510 contains edges which tend to show higher COMMIT and lower  $R_1$  edge weights than expected  
511 by chance. We previously showed edgewise inverse correlations between  $R_1$  and COMMIT  
512 which were robust to controlling for edge length. We also showed that  $R_1$  and FA are positively  
513 correlated under these same conditions. In this light, it is not surprising that the edges connecting  
514 rich-club nodes tend to show opposite trends in  $R_1$ - and FA-weighting with respect to COMMIT.  
515 Nonetheless, it is possible that the lack of a rich club in our myelin-weighted network is an  
516 artifact of tractometry. Future work will attempt to replicate this result using myelin-weighted  
517 networks computed with a different methodology (Schiavi et al., 2022).

518

519

### 520 ***Replication Across Parcellation Resolution and in a Second Dataset***

521 In this report, we have chosen to feature data in the Schaefer-400 cortical parcellation plus 14  
522 subcortical nodes. However, there is little consensus on the best brain atlas, and the optimal  
523 choice likely depends on the specifics of your data and the question being investigated. In a

524 supplementary analysis, we replicated our results across 100-900 node Schaefer cortical atlases.  
525 We found that residual edgewise correlations with FC (**Figure S1**) and  $R_1$  (**Figure S2**), as well  
526 as normalized rich club and normalized small worldness (**Figure S3**) were robust to parcellation  
527 resolution. In contrast, the spatial topography of high-hubness brain regions appears qualitatively  
528 dependent on parcellation granularity, although further analyses would be necessary to draw  
529 stronger conclusions (**Figure S4**).

530

531 An independent multimodal dataset was also used to replicate the main SC results including the  
532 residual edgewise correlations with  $R_1$  and the relationship between  $R_1$  and COMMIT across  
533 edge length bins (**Figure S5**), as well as all network topology results (**Figure S6**).

534

535

### 536 *Limitations*

537 Streamline tractography is known to suffer from several important biases including both false  
538 positive and negative streamlines, which can influence downstream analyses (Maier-Hein et al.,  
539 2017; Schilling et al., 2019; Sotiropoulos & Zalesky, 2019; Zalesky et al., 2016). Through  
540 probabilistic tractography, we opted to minimize false negatives while maximizing false  
541 positives. This allowed us to implement careful streamline- and edge-filtering strategies in post-  
542 processing to address this known bias. Still, without a ground truth, we cannot quantify the  
543 extent to which we were successful in mitigating this issue, nor can we guarantee that we did not  
544 erroneously filter true positive streamlines or edges. All processing and filtering methods were  
545 consistent and network density was uniform across weighted structural networks. Thus, any  
546 major tractography bias should be as homogeneous as possible across networks.

547  
548 Tractometry-derived brain networks suffer from widespread partial volume effects due to  
549 crossing and kissing fibers in a majority of white matter voxels. The net effect of this bias is well  
550 understood and is apparent in our results and previous work (De Santis et al., 2014; Schiavi et  
551 al., 2022). Nonetheless, this method was included here as our goal was to characterize widely  
552 used structural connectivity methods. New techniques for reducing this bias are currently being  
553 developed which allow for the estimation of tract-specific microstructural features (e.g.,  
554 (Barakovic, Girard, et al., 2021; Barakovic, Tax, et al., 2021; De Santis et al., 2016; Leppert et  
555 al., 2021, 2023; Schiavi et al., 2022)).

556  
557 We were unable to assess repeatability in this work as we did not have scan-rescan data.  
558 However, reproducibility has already been assessed for NODDI (Chung et al., 2016; Lehmann et  
559 al., 2021), MP2RAGE-derived T1 maps (Marques et al., 2010), diffusion-tractography-based  
560 structural connectivity (Bonilha et al., 2015), as well as COMMIT and SIFT2 tractogram  
561 filtering (Koch et al., 2022). The reproducibility of the tractometry features ( $R_1$ , FA, RD, ICVF)  
562 will mainly depend on these previous steps and the accuracy of the spatial alignment of the  
563 multi-modal data.

564  
565 In this work, we have attempted to thoroughly examine the fundamental properties of a wide  
566 range of standard and state-of-the-art metrics for quantifying white matter brain structure.  
567 However, the scope of possible methods and their respective variants is too broad to treat  
568 thoroughly in a single body of work. In particular, track-weighted imaging (Calamante, 2017;  
569 Calamante et al., 2010, 2012) and fixel-based analysis (Dhollander et al., 2021; Raffelt et al.,

570 2015, 2017) provide state-of-the-art solutions to the challenge of quantifying white matter  
571 structural features in the presence of crossing fibers.

572

573

## 574 ***Conclusion***

575 We presented a thorough characterization of weighted SC networks. Overall, our findings  
576 support the joint use of SC networks weighted by connection strength and myelin in predicting  
577 FC. In particular, using the COMMIT or SIFT2 algorithms to quantify connection strength  
578 shows promise to improve model interpretability relative to NoS. Beyond  $R_1$ , there is a wide  
579 array of myelin sensitive metrics that could be used to compute useful myelin-weighted  
580 networks. The integration of this microstructure-weighted connectivity approach into structure-  
581 function models will advance the mechanistic interpretation of both the function and dysfunction  
582 of the living human brain.

583

584

## 585 **MATERIALS and METHODS**

586 These data are available for download (<https://portal.conp.ca/dataset?id=projects/mica-mics>). See  
587 Royer et al. (Royer et al., 2022), Cruces et al. (Cruces et al., 2022) for full details of data  
588 acquisition and processing. All data processing and analysis code is openly available at  
589 <https://github.com/TardifLab/Weighted-SC-Networks>.

590

591

## 592 ***Data Acquisition & Preprocessing***

593 Multimodal MRI data was collected in 50 healthy volunteers at 3 Tesla on a Siemens Magnetom  
594 Prisma-Fit scanner equipped with a 64-channel head coil as follows:

- 595 • T<sub>1</sub>-weighted (T<sub>1w</sub>) anatomical: 3D magnetization-prepared rapid gradient-echo sequence  
596 (MP-RAGE; 0.8mm isotropic; TR = 2300ms; TE = 3.14ms; TI = 900ms; iPAT =  
597 2; partial Fourier = 6/8)
- 598 • Multi-shell diffusion-weighted imaging (DWI): 2D pulsed gradient spin-echo echo-planar  
599 imaging sequence consisting of three shells with b-values 300, 700, and 2000s/mm<sup>2</sup> and  
600 diffusion directions 10, 40, and 90, respectively (1.6mm isotropic; TR = 3500ms, TE =  
601 64.40ms; multi-band factor = 3). b<sub>0</sub> images were also acquired with reverse phase  
602 encoding direction to facilitate distortion correction of DWI data.
- 603 • 7 minutes of resting-state functional MRI: multi-band accelerated 2D-BOLD gradient  
604 echo echo-planar sequence (3mm isotropic; TR = 600ms, TE = 30ms; mb factor = 6; flip  
605 angle = 52°). Two spin-echo images with AP and PA phase encoding were additionally  
606 acquired (3mm isotropic; TR = 4029ms; TE = 48ms; flip angle=90°).
- 607 • Quantitative T<sub>1</sub> relaxometry data was acquired with a 3D-MP2RAGE sequence (Marques  
608 et al., 2010) (0.8mm isotropic; TR = 5000ms, TE = 2.9ms, TI<sub>1</sub> = 940ms, T<sub>12</sub> = 2830ms;  
609 iPAT = 3; partial Fourier = 6/8). This was used to compute a T<sub>1</sub> map which was sampled  
610 to estimate the edge weights in R<sub>1</sub> (1/T<sub>1</sub>) networks (myelin-weighted).

611

612 The multi-modal processing pipeline *micapipe* (Cruces et al., 2022)

613 (<https://micapipe.readthedocs.io/>) was used to preprocess diffusion, anatomical, and functional

614 images. T<sub>1w</sub> images were deobliqued, reoriented to standard neuroscience orientation (LPI),

615 corrected for intensity non-uniformity (Tustison et al., 2010), intensity normalized and skull



616 stripped. Subcortical segmentations were performed with FSL FIRST (Jenkinson et al., 2012;  
617 Patenaude et al., 2011) and tissue types were classified using FSL FAST (Y. Zhang et al., 2001).  
618 A five-tissue-type image segmentation was generated for anatomically constrained tractography  
619 (R. E. Smith et al., 2012). Cortical surface segmentations were generated with FreeSurfer 6.0  
620 (Dale et al., 1999; Fischl, Sereno, & Dale, 1999; Fischl, Sereno, Tootell, et al., 1999).

621  
622 Diffusion preprocessing was performed in native DWI space using tools from MRtrix3 (J.  
623 Donald Tournier et al., 2012, 2019) and proceeded in the following sequence: (1) image  
624 denoising (Cordero-Grande et al., 2019; Veraart, Fieremans, et al., 2016; Veraart, Novikov, et  
625 al., 2016); (2) two  $b=0$ s/mm<sup>2</sup> volumes with reverse phase encoding were used to correct for  
626 susceptibility distortion, head motion, and eddy currents via FSL's eddy and TOPUP tools  
627 (Andersson et al., 2003; Andersson & Sotiropoulos, 2016; S. M. Smith et al., 2004); and (3) B1+  
628 bias-field correction (Tustison et al., 2010). This pre-processed data was used to estimate multi-  
629 shell and multi-tissue response functions for constrained spherical-deconvolution (Christiaens et  
630 al., 2015; Dhollander et al., 2016, 2019; Jeurissen et al., 2014) followed by intensity  
631 normalization. Non-linear registration was performed with ANTs (Avants et al., 2008) to co-  
632 register anatomical images to DWI space.

633  
634 Resting-state fMRI pre-processing entailed discarding the first five TRs, reorientation (LPI),  
635 motion correction by registering all volumes to the mean, and distortion correction using main  
636 phase and reverse phase field maps. Nuisance signal was removed using an ICA-FIX (Salimi-  
637 Khorshidi et al., 2014) classifier and by spike regression using motion outlier outputs from FSL  
638 (Jenkinson et al., 2012). Volumetric timeseries were averaged for boundary-based registration

639 (Greve & Fischl, 2009) to native Freesurfer space and mapped to individual surfaces using  
640 trilinear interpolation. Spatial smoothing (Gaussian, FWHM = 10mm) was applied to native-  
641 surface and template-mapped cortical timeseries.

642

643

#### 644 *Tractography and Microstructural Metrics*

645 To estimate structural connectomes, anatomically constrained tractography (R. E. Smith et al.,  
646 2012) was performed on the normalized white matter FOD image using the probabilistic  
647 algorithm iFOD2 (J.-D. Tournier et al., 2010). Tractograms of 5 million streamlines were  
648 generated by seeding the gray-white matter interface using the following parameters:  
649 maxlength=400, minlength=10, angle=22.5, step=0.5, cutoff=0.06, backtrack, crop\_at\_gmwmi  
650 (gray-matter-white-matter interface). These tractograms were filtered in a two-stage process. (1)  
651 a temporary whole-brain connectome weighted by NoS was computed then decomposed into its  
652 composite streamlines to derive a new tractogram in which any streamline which failed to  
653 connect two gray matter ROIs in the temporary connectome was excluded. This “streamline-  
654 filtering” step typically resulted in approximately a 5% decrease in the size of the tractogram  
655 (~250k streamlines removed) and was undertaken to ensure that these erroneous streamlines did  
656 not affect the COMMIT model. Streamline-filtered tractograms were used to compute NoS and  
657 were used as inputs to both the SIFT2 and COMMIT models. COMMIT was run using a Stick-  
658 Zeppelin-Ball forward model and default settings (see <https://github.com/daducci/COMMIT>). (2)  
659 Any streamline with a COMMIT weight  $< 1e^{-12}$  (machine precision 0) was interpreted as a false  
660 positive and filtered from the tractogram. This streamline-level COMMIT-filtering step typically  
661 resulted in greater than a 90% decrease in the size of the tractogram with most containing

662 between ~300-600k streamlines. COMMIT-filtered tractograms were used not only in the  
663 computation of COMMIT, but all tractometry networks as well. This additional filtering step was  
664 performed on COMMIT streamline weights only (not SIFT2) to reduce the impact of false  
665 positive streamlines in tractometry networks as much as possible.

666  
667 In a supplemental analysis, the COMMIT streamline weights were additionally used in the  
668 computation of edge weights in tractometry-derived networks by performing a COMMIT-  
669 weighted average of a given tractometry metric (e.g., FA) over streamlines for each node pair  
670 **(Figure S10-S12)**.

671

672

### 673 *Construction of Weighted Structural Networks*

674 The streamline-specific SC networks were computed in the following manner: (1) NoS as the  
675 summed streamline count; (2) LoS as the mean streamline length; (3) SIFT2 as the sum of SIFT2  
676 streamline weights; and (4) COMMIT as the length-weighted sum of COMMIT streamline  
677 weights as in (Schiavi et al., 2020). Explicitly, edgewise entries in COMMIT-weighted networks  
678 were computed as:

$$679 \quad \alpha_{ij} = \frac{\sum_{k=1}^{N_{ij}} (x_{ij}^k * l_k)}{\bar{L}_{ij}},$$

680 where  $\alpha_{ij}$  is the edge weight between nodes  $i$  and  $j$ ;  $\bar{L}_{ij}$  is the mean streamline length;  $N_{ij}$  is the  
681 number of streamlines;  $x_{ij}^k$  is the COMMIT weight of streamline  $k$ ; and  $l_k$  is its length. Edge  
682 weights in NoS, SIFT2 and COMMIT were normalized by node volume.

683

684 SC networks weighted by FA, RD, ICVF (H. Zhang et al., 2012) and  $R_1$  were derived using  
685 multi-modal tractometry (S Bells et al., 2011). Streamline weights were computed by: (1) co-  
686 registering the tractogram and desired image; and (2) sampling the voxel-level aggregate value  
687 along the length of each streamline. Edge weights were computed as the median along each  
688 streamline and the mean across streamlines by node pair. Voxel-wise measures of FA and RD  
689 were computed with a diffusion tensor model (Basser et al., 1994) and ICVF by applying the  
690 NODDI multi-compartment model (H. Zhang et al., 2012) to preprocessed DWI data (Daducci,  
691 Canales-Rodríguez, et al., 2015).

692

693 The 400-node Schaefer (Schaefer et al., 2018) cortical parcellation is used in all results.  
694 Subcortical ROIs corresponded to 7 bilateral regions (14 nodes) including the amygdala,  
695 thalamus, caudate, accumbens, putamen, hippocampus, and pallidum. A single static, zero-lag  
696 FC network was derived by product-moment pairwise Pearson cross-correlation of node-  
697 averaged time series. FC network edge weights were Fisher Z-transformed.

698

699

### 700 *Connectome post-processing*

701 COMMIT-weighted networks were used to filter all other weighted structural networks at the  
702 edge level. This was chosen as COMMIT-weighted networks had the lowest connection density  
703 to start, and all non-zero COMMIT edges were also non-zero in all other SC networks. All SC  
704 networks were thresholded at the edge level within subject by: (1) setting edges = 0 in all  
705 weighted SC networks if that edge had a COMMIT weight  $< 1e^{-12}$ ; and (2) applying a 50%  
706 uniform threshold mask to facilitate group-consensus averaging. This minimized differences in

707 binary structural network density across subjects and enforced a uniform binary connectivity  
708 map across weighted SC networks at the group level and within subject. Group-level networks  
709 were computed as the subject-wise mean at each edge excluding zero-valued edges.

710

711

### 712 *Network Analysis*

713 Network analysis was performed using tools (Rubinov & Sporns, 2010) based on graph theory  
714 (Fornito et al., 2013; Sporns, 2018). Measures of clustering coefficient and path length were  
715 normalized against 50 degree and strength preserving null networks. Clustering coefficient was  
716 normalized within node then averaged across nodes to obtain a scalar value per network. The  
717 following weight ( $W_{ij}$ ) to length ( $L_{ij}$ ) transform was used in path length computation:  $L_{ij} = -$   
718  $\log(W_{ij})$ . Weighted rich-club curves were normalized against 1000 degree and strength  
719 preserving null networks. The edges in all degree and strength preserving null networks were  
720 rewired  $1e^6$  times total, and the strength sequence was approximated using simulated annealing.  
721 Rich-club curves were normalized in binary networks against 1000 degree preserving null  
722 networks in which each edge was rewired 100 times. All edge rewiring followed the Maslov &  
723 Sneppen rewiring model (Maslov & Sneppen, 2002). Similar to (M. P. van den Heuvel et al.,  
724 2010), hubness scores (0-5) were computed as 1 point for all nodes showing top 20% strength,  
725 betweenness, closeness or eigenvector centrality; and lowest 20% clustering coefficient.

726

727

### 728 *Permutation Testing*

729 Statistical significance for the edgewise correlation of residual edge weights in NoS, SIFT2,  
730 COMMIT and R<sub>1</sub> with FC (**Figure S7**); as well as all connection-strength-weighted networks  
731 with R<sub>1</sub> (**Figure S8**) was quantified using permutation testing as described in supplementary  
732 material. One-sided p-values are reported in the main text figures as p<sub>perm</sub>.

733

734

## 735 **ACKNOWLEDGMENTS**

736 We acknowledge research support from the National Science and Engineering Research Council  
737 of Canada (NSERC Discovery-1304413, DGEGR-2018-00216 ), the CIHR (FDN-154298, PJT-  
738 174995), SickKids Foundation (NI17-039), Azrieli Center for Autism Research (ACAR-TACC),  
739 Brain Canada, Fonds de recherche du Québec – Santé (FRQ-S), Healthy Brains for Healthy  
740 Lives, and the Tier-2 Canada Research Chairs program.

741

742

## 743 **REFERENCES**

- 744 Alexander, D. C., Dyrby, T. B., Nilsson, M., & Zhang, H. (2019). Imaging brain microstructure with diffusion MRI: practicality and applications.  
745 *NMR in Biomedicine*, 32(4), 1–26. <https://doi.org/10.1002/nbm.3841>
- 746 Alexander, D. C., Hubbard, P. L., Hall, M. G., Moore, E. A., Ptito, M., Parker, G. J. M., & Dyrby, T. B. (2010). Orientationally invariant indices  
747 of axon diameter and density from diffusion MRI. *NeuroImage*, 52(4), 1374–1389. <https://doi.org/10.1016/j.neuroimage.2010.05.043>
- 748 Amico, E., & Goñi, J. (2018). The quest for identifiability in human functional connectomes. *Scientific Reports*, 8(1), 1–14.  
749 <https://doi.org/10.1038/s41598-018-25089-1>
- 750 Andersson, J. L. R., Skare, S., & Ashburner, J. (2003). How to correct susceptibility distortions in spin-echo echo-planar images: Application to  
751 diffusion tensor imaging. *NeuroImage*, 20(2), 870–888. [https://doi.org/10.1016/S1053-8119\(03\)00336-7](https://doi.org/10.1016/S1053-8119(03)00336-7)
- 752 Andersson, J. L. R., & Sotiropoulos, S. N. (2016). An integrated approach to correction for off-resonance effects and subject movement in  
753 diffusion MR imaging. *NeuroImage*, 125, 1063–1078. <https://doi.org/10.1016/j.neuroimage.2015.10.019>
- 754 Assaf, Y., Blumenfeld-Katzir, T., Yovel, Y., & Basser, P. J. (2008). AxCaliber: A method for measuring axon diameter distribution from  
755 diffusion MRI. *Magnetic Resonance in Medicine*, 59(6), 1347–1354. <https://doi.org/10.1002/mrm.21577>

- 756 Avants, B. B., Epstein, C. L., Grossman, M., & Gee, J. C. (2008). Symmetric diffeomorphic image registration with cross-correlation: Evaluating  
757 automated labeling of elderly and neurodegenerative brain. *Medical Image Analysis*, *12*(1), 26–41.  
758 <https://doi.org/10.1016/j.media.2007.06.004>
- 759 Barakovic, M., Girard, G., Schiavi, S., Romascano, D., Descoteaux, M., Granziera, C., Jones, D. K., Innocenti, G. M., Thiran, J.-P., & Daducci,  
760 A. (2021). Bundle-Specific Axon Diameter Index as a New Contrast to Differentiate White Matter Tracts. *Frontiers in Neuroscience*,  
761 *15*(June), 1–13. <https://doi.org/10.3389/fnins.2021.646034>
- 762 Barakovic, M., Tax, C. M. W., Rudrapatna, U., Chamberland, M., Rafael-Patino, J., Granziera, C., Thiran, J. P., Daducci, A., Canales-Rodríguez,  
763 E. J., & Jones, D. K. (2021). Resolving bundle-specific intra-axonal T2 values within a voxel using diffusion-relaxation tract-based  
764 estimation. *NeuroImage*, *227*(September 2020), 117617. <https://doi.org/10.1016/j.neuroimage.2020.117617>
- 765 Basser, P. J. (1995). Inferring microstructural features and the physiological state of tissues from diffusion- weighted images. *NMR in*  
766 *Biomedicine*, *8*(7), 333–344. <https://doi.org/10.1002/nbm.1940080707>
- 767 Basser, P. J., Mattiello, J., & Lebihan, D. (1994). Estimation of the Effective Self-Diffusion Tensor from the NMR Spin Echo. In *Journal of*  
768 *Magnetic Resonance, Series B* (Vol. 103, Issue 3, pp. 247–254). <https://doi.org/10.1006/jmrb.1994.1037>
- 769 Bassett, D. S., & Bullmore, E. (2006). Small-world brain networks. *Neuroscientist*, *12*(6), 512–523. <https://doi.org/10.1177/1073858406293182>
- 770 Bassett, D. S., & Bullmore, E. T. (2017). Small-World Brain Networks Revisited. *Neuroscientist*, *23*(5), 499–516.  
771 <https://doi.org/10.1177/1073858416667720>
- 772 Bells, S, Cercignani, M., Deoni, S., & Assaf, Y. (2011). “Tractometry” – comprehensive multi-modal quantitative assessment of white matter  
773 along specific tracts. *Proceedings of the International Society for Magnetic Resonance in Medicine*, *19*(2009), 678.  
774 <http://cds.ismrm.org/protected/11MProceedings/files/678.pdf>
- 775 Bells, Sonya, Lefebvre, J., Prescott, S. A., Dockstader, C., Bouffet, E., Skocic, J., Laughlin, S., & Mabbott, D. J. (2017). Changes in white matter  
776 microstructure impact cognition by disrupting the ability of neural assemblies to synchronize. *Journal of Neuroscience*, *37*(34), 8227–  
777 8238. <https://doi.org/10.1523/jneurosci.0560-17.2017>
- 778 Berthold, C. H., Nilsson, I., & Rydmark, M. (1983). Axon diameter and myelin sheath thickness in nerve fibres of the ventral spinal root of the  
779 seventh lumbar nerve of the adult and developing cat. *Journal of Anatomy*, *136*(Pt 3), 483–508.  
780 <https://pubmed.ncbi.nlm.nih.gov/6885614/>
- 781 Biswal, B., Zerrin Yetkin, F., Haughton, V. M., & Hyde, J. S. (1995). Functional connectivity in the motor cortex of resting human brain using  
782 echo-planar mri. *Magnetic Resonance in Medicine*, *34*(4), 537–541. <https://doi.org/10.1002/mrm.1910340409>
- 783 Bonilha, L., Gleichgerrcht, E., Fridriksson, J., Breedlove, J. L., Rorden, C., Nesland, T., Paulus, W., Helms, G., & Focke, N. K. (2015).  
784 Reproducibility of the structural brain connectome derived from diffusion tensor imaging. *PLoS ONE*, *10*(9), 1–17.  
785 <https://doi.org/10.1371/journal.pone.0135247>
- 786 Boshkovski, T., Kocarev, L., Cohen-Adad, J., Mišić, B., Lehericy, S., Stikov, N., & Mancini, M. (2021). The R1-weighted connectome:  
787 complementing brain networks with a myelin-sensitive measure. *Network Neuroscience*, *5*(2), 358–372.  
788 [https://doi.org/10.1162/netn\\_a\\_00179](https://doi.org/10.1162/netn_a_00179)
- 789 Bullmore, E., & Sporns, O. (2012). The economy of brain network organization. *Nature Reviews Neuroscience*, *13*(5), 336–349.  
790 <https://doi.org/10.1038/nrn3214>

- 791 Cabral, J., Kringelbach, M. L., & Deco, G. (2017). Functional connectivity dynamically evolves on multiple time-scales over a static structural  
792 connectome: Models and mechanisms. *NeuroImage*, 160(March), 84–96. <https://doi.org/10.1016/j.neuroimage.2017.03.045>
- 793 Caeyenberghs, K., Metzler-Baddeley, C., Foley, S., & Jones, D. K. (2016). Dynamics of the human structural connectome underlying working  
794 memory training. *Journal of Neuroscience*, 36(14), 4056–4066. <https://doi.org/10.1523/JNEUROSCI.1973-15.2016>
- 795 Calamante, F. (2017). Track-weighted imaging methods: extracting information from a streamlines tractogram. *Magnetic Resonance Materials in*  
796 *Physics, Biology and Medicine*, 30(4), 317–335. <https://doi.org/10.1007/s10334-017-0608-1>
- 797 Calamante, F., Tournier, J. D., Jackson, G. D., & Connelly, A. (2010). Track-density imaging (TDI): Super-resolution white matter imaging using  
798 whole-brain track-density mapping. *NeuroImage*, 53(4), 1233–1243. <https://doi.org/10.1016/j.neuroimage.2010.07.024>
- 799 Calamante, F., Tournier, J. D., Smith, R. E., & Connelly, A. (2012). A generalised framework for super-resolution track-weighted imaging.  
800 *NeuroImage*, 59(3), 2494–2503. <https://doi.org/10.1016/j.neuroimage.2011.08.099>
- 801 Christiaens, D., Reisert, M., Dhollander, T., Sunaert, S., Suetens, P., & Maes, F. (2015). Global tractography of multi-shell diffusion-weighted  
802 imaging data using a multi-tissue model. *NeuroImage*, 123, 89–101. <https://doi.org/10.1016/j.neuroimage.2015.08.008>
- 803 Chung, A. W., Seunarine, K. K., & Clark, C. A. (2016). NODDI reproducibility and variability with magnetic field strength: A comparison  
804 between 1.5 T and 3 T. *Human Brain Mapping*, 37(12), 4550–4565. <https://doi.org/10.1002/hbm.23328>
- 805 Collin, G., Sporns, O., Mandl, R. C. W., & Van Den Heuvel, M. P. (2014). Structural and functional aspects relating to cost and benefit of rich  
806 club organization in the human cerebral cortex. *Cerebral Cortex*, 24(9), 2258–2267. <https://doi.org/10.1093/cercor/bht064>
- 807 Cordero-Grande, L., Christiaens, D., Hutter, J., Price, A. N., & Hajnal, J. V. (2019). Complex diffusion-weighted image estimation via matrix  
808 recovery under general noise models. *NeuroImage*, 200(March), 391–404. <https://doi.org/10.1016/j.neuroimage.2019.06.039>
- 809 Cruces, R. R., Royer, J., Herholz, P., Larivière, S., Vos de Wael, R., Paquola, C., Benkarim, O., Park, B., Degré-Pelletier, J., Nelson, M. C.,  
810 DeKraker, J., Leppert, I. R., Tardif, C., Poline, J.-B., Concha, L., & Bernhardt, B. C. (2022). Micapipe: A pipeline for multimodal  
811 neuroimaging and connectome analysis. *NeuroImage*, 263(August), 119612. <https://doi.org/10.1016/j.neuroimage.2022.119612>
- 812 Daducci, A., Canales-Rodríguez, E. J., Zhang, H., Dyrby, T. B., Alexander, D. C., & Thiran, J. P. (2015). Accelerated Microstructure Imaging via  
813 Convex Optimization (AMICO) from diffusion MRI data. *NeuroImage*, 105, 32–44. <https://doi.org/10.1016/j.neuroimage.2014.10.026>
- 814 Daducci, A., Dal Palu, A., Lemkaddem, A., & Thiran, J. P. (2013). A convex optimization framework for global tractography. *Proceedings -*  
815 *International Symposium on Biomedical Imaging*, 524–527. <https://doi.org/10.1109/ISBI.2013.6556527>
- 816 Daducci, A., Dal Palù, A., Lemkaddem, A., & Thiran, J. P. (2015). COMMIT: Convex optimization modeling for microstructure informed  
817 tractography. *IEEE Transactions on Medical Imaging*, 34(1), 246–257. <https://doi.org/10.1109/TMI.2014.2352414>
- 818 Dale, A. M., Fischl, B., & Sereno, M. I. (1999). Cortical Surface-Based Analysis. *NeuroImage*, 9(2), 179–194.  
819 <https://doi.org/10.1006/nimg.1998.0395>
- 820 de Reus, M. A., & van den Heuvel, M. P. (2014). Simulated rich club lesioning in brain networks: A scaffold for communication and integration?  
821 *Frontiers in Human Neuroscience*, 8(AUG), 1–5. <https://doi.org/10.3389/fnhum.2014.00647>
- 822 De Santis, S., Assaf, Y., Jeurissen, B., Jones, D. K., & Roebroeck, A. (2016). T1 relaxometry of crossing fibres in the human brain. *NeuroImage*,  
823 141, 133–142. <https://doi.org/10.1016/j.neuroimage.2016.07.037>
- 824 De Santis, S., Drakesmith, M., Bells, S., Assaf, Y., & Jones, D. K. (2014). Why diffusion tensor MRI does well only some of the time: Variance  
825 and covariance of white matter tissue microstructure attributes in the living human brain. *NeuroImage*, 89, 35–44.



826 <https://doi.org/10.1016/j.neuroimage.2013.12.003>

827 Deligianni, F., Carmichael, D. W., Zhang, G. H., Clark, C. A., & Clayden, J. D. (2016). NODDI and tensor-based microstructural indices as  
828 predictors of functional connectivity. *PLoS ONE*, *11*(4), 1–17. <https://doi.org/10.1371/journal.pone.0153404>

829 Dhollander, T., Clemente, A., Singh, M., Boonstra, F., Civier, O., Duque, J. D., Egorova, N., Enticott, P., Fuelscher, I., Gajamange, S., Genc, S.,  
830 Gottlieb, E., Hyde, C., Imms, P., Kelly, C., Kirkovski, M., Kolbe, S., Liang, X., Malhotra, A., ... Caeyenberghs, K. (2021). Fixel-based  
831 Analysis of Diffusion MRI: Methods, Applications, Challenges and Opportunities. *NeuroImage*, *241*(November 2020), 118417.  
832 <https://doi.org/10.1016/j.neuroimage.2021.118417>

833 Dhollander, T., Mito, R., Raffelt, D., & Connelly, A. (2019). Improved white matter response function estimation for 3-tissue constrained  
834 spherical deconvolution. *Proc. Intl. Soc. Mag. Reson. Med*, *May 11-16*, 555.  
835 [https://www.researchgate.net/publication/331165168\\_Improved\\_white\\_matter\\_response\\_function\\_estimation\\_for\\_3-](https://www.researchgate.net/publication/331165168_Improved_white_matter_response_function_estimation_for_3-tissue_constrained_spherical_deconvolution)  
836 [tissue\\_constrained\\_spherical\\_deconvolution](https://www.researchgate.net/publication/331165168_Improved_white_matter_response_function_estimation_for_3-tissue_constrained_spherical_deconvolution)

837 Dhollander, T., Raffelt, D., & Connelly, A. (2016). Unsupervised 3-tissue response function estimation from single-shell or multi-shell diffusion  
838 MR data without a co-registered T1 image Predicting stroke impairment using machine learning techniques View project A novel sparse  
839 partial correlation method fo. *ISMRM Workshop on Breaking the Barriers of Diffusion MRI*, *35*(September), 1–2.  
840 <https://www.researchgate.net/publication/307863133>

841 Douglas Fields, R. (2015). A new mechanism of nervous system plasticity: activity-dependent myelination. *Nature Reviews Neuroscience*,  
842 *16*(12), 756–767. <https://doi.org/10.1007/s11065-015-9294-9>.Functional

843 Drakesmith, M., Harms, R., Rudrapatna, S. U., Parker, G. D., Evans, C. J., & Jones, D. K. (2019). Estimating axon conduction velocity in vivo  
844 from microstructural MRI. *NeuroImage*, *203*(March), 116186. <https://doi.org/10.1016/j.neuroimage.2019.116186>

845 Finn, E. S., Huber, L., Jangraw, D. C., Molfese, P. J., & Bandettini, P. A. (2019). Layer-dependent activity in human prefrontal cortex during  
846 working memory. *Nature Neuroscience*, *22*(10), 1687–1695. <https://doi.org/10.1038/s41593-019-0487-z>

847 Fischl, B., Sereno, M. I., & Dale, A. M. (1999). Cortical surface-based analysis: II. Inflation, flattening, and a surface-based coordinate system.  
848 *NeuroImage*, *9*(2), 195–207. <https://doi.org/10.1006/nimg.1998.0396>

849 Fischl, B., Sereno, M. I., Tootell, R. B. H., & Dale, A. M. (1999). High-resolution intersubject averaging and a coordinate system for the cortical  
850 surface. *Human Brain Mapping*, *8*(4), 272–284. [https://doi.org/10.1002/\(SICI\)1097-0193\(1999\)8:4<272::AID-HBM10>3.0.CO;2-4](https://doi.org/10.1002/(SICI)1097-0193(1999)8:4<272::AID-HBM10>3.0.CO;2-4)

851 Fornito, A., Zalesky, A., & Breakspear, M. (2013). Graph analysis of the human connectome: Promise, progress, and pitfalls. *NeuroImage*, *80*,  
852 426–444. <https://doi.org/10.1016/j.neuroimage.2013.04.087>

853 Fornito, A., Zalesky, A., & Breakspear, M. (2015). The connectomics of brain disorders. *Nature Reviews Neuroscience*, *16*(3), 159–172.  
854 <https://doi.org/10.1038/nrn3901>

855 Fornito, A., Zalesky, A., & Bullmore, E. T. (2016). Fundamentals of Brain Network Analysis. In *Fundamentals of Brain Network Analysis*.  
856 Elsevier. <https://doi.org/10.1016/C2012-0-06036-X>

857 Frigo, M., Deslauriers-Gauthier, S., Parker, D., Ismail, A. A. O., Kim, J. J., Verma, R., & Deriche, R. (2020). Diffusion MRI tractography  
858 filtering techniques change the topology of structural connectomes. *Journal of Neural Engineering*, *17*(6). [https://doi.org/10.1088/1741-](https://doi.org/10.1088/1741-2552/abc29b)  
859 [2552/abc29b](https://doi.org/10.1088/1741-2552/abc29b)

860 Friston, K. J. (2011). Functional and effective connectivity: a review. *Brain Connectivity*, *1*(1), 13–36. <https://doi.org/10.1089/brain.2011.0008>

- 861 Gibson, E. M., Geraghty, A. C., & Monje, M. (2018). Bad wrap: Myelin and myelin plasticity in health and disease. In *Developmental*  
862 *Neurobiology* (Vol. 78, Issue 2, pp. 123–135). John Wiley and Sons Inc. <https://doi.org/10.1002/dneu.22541>
- 863 Girard, G., Whittingstall, K., Deriche, R., & Descoteaux, M. (2014). Towards quantitative connectivity analysis: Reducing tractography biases.  
864 *NeuroImage*, 98, 266–278. <https://doi.org/10.1016/j.neuroimage.2014.04.074>
- 865 Gordon, E. M., Laumann, T. O., Gilmore, A. W., Newbold, D. J., Greene, D. J., Berg, J. J., Ortega, M., Hoyt-Drazen, C., Grattton, C., Sun, H.,  
866 Hampton, J. M., Coalson, R. S., Nguyen, A. L., McDermott, K. B., Shimony, J. S., Snyder, A. Z., Schlaggar, B. L., Petersen, S. E.,  
867 Nelson, S. M., & Dosenbach, N. U. F. (2017). Precision Functional Mapping of Individual Human Brains. *Neuron*, 95(4), 791–807.e7.  
868 <https://doi.org/10.1016/j.neuron.2017.07.011>
- 869 Greicius, M. D., Krasnow, B., Reiss, A. L., & Menon, V. (2003). Functional connectivity in the resting brain: A network analysis of the default  
870 mode hypothesis. *Proceedings of the National Academy of Sciences of the United States of America*, 100(1), 253–258.  
871 <https://doi.org/10.1073/pnas.0135058100>
- 872 Greve, D. N., & Fischl, B. (2009). Accurate and robust brain image alignment using boundary-based registration. *NeuroImage*, 48(1), 63–72.  
873 <https://doi.org/10.1016/j.neuroimage.2009.06.060>
- 874 Griffa, A., & Van den Heuvel, M. P. (2018). Rich-club neurocircuitry: function, evolution, and vulnerability. *Dialogues in Clinical Neuroscience*,  
875 20(2), 121–132. <https://doi.org/10.31887/DCNS.2018.20.2/agriffa>
- 876 Hampson, M., Driesen, N. R., Skudlarski, P., Gore, J. C., & Constable, R. T. (2006). Brain connectivity related to working memory performance.  
877 *Journal of Neuroscience*, 26(51), 13338–13343. <https://doi.org/10.1523/JNEUROSCI.3408-06.2006>
- 878 Harris, J. J., & Attwell, D. (2012). The energetics of CNS white matter. *Journal of Neuroscience*, 32(1), 356–371.  
879 <https://doi.org/10.1523/JNEUROSCI.3430-11.2012>
- 880 Heath, F., Hurley, S. A., Johansen-Berg, H., & Sampaio-Baptista, C. (2018). Advances in noninvasive myelin imaging. *Developmental*  
881 *Neurobiology*, 78(2), 136–151. <https://doi.org/10.1002/dneu.22552>
- 882 Hildebrand, C., & Hahn, R. (1978). Relation between myelin sheath thickness and axon size in spinal cord white matter of some vertebrate  
883 species. *Journal of the Neurological Sciences*, 38(3), 421–434. [https://doi.org/10.1016/0022-510X\(78\)90147-8](https://doi.org/10.1016/0022-510X(78)90147-8)
- 884 Hodgkin, A. L., & Huxley, A. F. (1952). A quantitative description of membrane current and its application to conduction and excitation in nerve.  
885 *The Journal of Physiology*, 117(4), 500–544. <https://doi.org/10.1113/jphysiol.1952.sp004764>
- 886 Honey, C. J., Sporns, O., Cammoun, L., Gigandet, X., Thiran, J. P., Meuli, R., & Hagmann, P. (2009). Predicting human resting-state functional  
887 connectivity from structural connectivity. *Proceedings of the National Academy of Sciences of the United States of America*, 106(6),  
888 2035–2040. <https://doi.org/10.1073/pnas.0811168106>
- 889 Huntenburg, J. M., Bazin, P. L., Goulas, A., Tardif, C. L., Villringer, A., & Margulies, D. S. (2017). A Systematic Relationship Between  
890 Functional Connectivity and Intracortical Myelin in the Human Cerebral Cortex. *Cerebral Cortex*, 27(2), 981–997.  
891 <https://doi.org/10.1093/cercor/bhx030>
- 892 Huxley, A. F., & Stämpfli, R. (1949). Evidence for saltatory conduction in peripheral myelinated nerve fibres. *The Journal of Physiology*, 108(3),  
893 315–339. <http://www.ncbi.nlm.nih.gov/pubmed/16991863>
- 894 Jenkinson, M., Beckmann, C. F., Behrens, T. E. J., Woolrich, M. W., & Smith, S. M. (2012). FSL. *NeuroImage*, 62(2), 782–790.  
895 <https://doi.org/10.1016/j.neuroimage.2011.09.015>

- 896 Jeurissen, B., Descoteaux, M., Mori, S., & Leemans, A. (2017). Diffusion MRI fiber tractography of the brain. *NMR in Biomedicine*, *32*(4), 1–22.  
897 <https://doi.org/10.1002/nbm.3785>
- 898 Jeurissen, B., Leemans, A., Tournier, J. D., Jones, D. K., & Sijbers, J. (2012). Investigating the prevalence of complex fiber configurations in  
899 white matter tissue with diffusion magnetic resonance imaging. *Human Brain Mapping*, *34*(11), 2747–2766.  
900 <https://doi.org/10.1002/hbm.22099>
- 901 Jeurissen, B., Tournier, J. D., Dhollander, T., Connelly, A., & Sijbers, J. (2014). Multi-tissue constrained spherical deconvolution for improved  
902 analysis of multi-shell diffusion MRI data. *NeuroImage*, *103*, 411–426. <https://doi.org/10.1016/j.neuroimage.2014.07.061>
- 903 Jones, D. K. (2010). Challenges and limitations of quantifying brain connectivity in vivo with diffusion MRI. *Imaging in Medicine*, *2*(3), 341–  
904 355. <https://doi.org/10.2217/iim.10.21>
- 905 Jones, D. K., Knösche, T. R., & Turner, R. (2013). White matter integrity, fiber count, and other fallacies: The do's and don'ts of diffusion MRI.  
906 *NeuroImage*, *73*, 239–254. <https://doi.org/10.1016/j.neuroimage.2012.06.081>
- 907 Kim, D. J., & Min, B. K. (2020). Rich-club in the brain's macrostructure: Insights from graph theoretical analysis. *Computational and Structural*  
908 *Biotechnology Journal*, *18*, 1761–1773. <https://doi.org/10.1016/j.csbj.2020.06.039>
- 909 Koch, P. J., Girard, G., Brügger, J., Cadic-Melchior, A. G., Beanato, E., Park, C.-H., Morishita, T., Wessel, M. J., Pizzolato, M., Canales-  
910 Rodríguez, E. J., Fisch-Gomez, E., Schiavi, S., Daducci, A., Piredda, G. F., Hilbert, T., Kober, T., Thiran, J.-P., & Hummel, F. C. (2022).  
911 Evaluating reproducibility and subject-specificity of microstructure-informed connectivity. *NeuroImage*, *258*(June), 119356.  
912 <https://doi.org/10.1016/j.neuroimage.2022.119356>
- 913 Larivière, S., Paquola, C., Park, B. yong, Royer, J., Wang, Y., Benkarim, O., Vos de Wael, R., Valk, S. L., Thomopoulos, S. I., Kirschner, M.,  
914 Lewis, L. B., Evans, A. C., Sisodiya, S. M., McDonald, C. R., Thompson, P. M., & Bernhardt, B. C. (2021). The ENIGMA Toolbox:  
915 multiscale neural contextualization of multisite neuroimaging datasets. *Nature Methods*, *18*(7), 698–700. <https://doi.org/10.1038/s41592-021-01186-4>
- 917 Lehmann, N., Aye, N., Kaufmann, J., Heinze, H. J., Düzel, E., Ziegler, G., & Taubert, M. (2021). Longitudinal Reproducibility of Neurite  
918 Orientation Dispersion and Density Imaging (NODDI) Derived Metrics in the White Matter. *Neuroscience*, *457*, 165–185.  
919 <https://doi.org/10.1016/j.neuroscience.2021.01.005>
- 920 Leppert, I. R., Andrews, D. A., Campbell, J. S. W., Park, D. J., Pike, G. B., Polimeni, J. R., & Tardif, C. L. (2021). Efficient whole-brain tract-  
921 specific T1 mapping at 3T with slice-shuffled inversion-recovery diffusion-weighted imaging. *Magnetic Resonance in Medicine*, *86*(2),  
922 738–753. <https://doi.org/10.1002/mrm.28734>
- 923 Leppert, I. R., Bontempi, P., Rowley, C. D., Campbell, J. S., Nelson, M. C., Schiavi, S., Pike, G. B., Daducci, A., & Tardif, C. L. (2023). Dual-  
924 encoded magnetization transfer and diffusion imaging and its application to tract-specific microstructure mapping. *ArXiv*, 1–26.  
925 <http://arxiv.org/abs/2303.03449>
- 926 Liégeois, R., Li, J., Kong, R., Orban, C., Van De Ville, D., Ge, T., Sabuncu, M. R., & Yeo, B. T. T. (2019). Resting brain dynamics at different  
927 timescales capture distinct aspects of human behavior. *Nature Communications*, *10*(1). <https://doi.org/10.1038/s41467-019-10317-7>
- 928 Liu, Z. Q., Vázquez-Rodríguez, B., Spreng, R. N., Bernhardt, B. C., Betzel, R. F., & Misisic, B. (2022). Time-resolved structure-function coupling  
929 in brain networks. *Communications Biology*, *5*(1), 1–10. <https://doi.org/10.1038/s42003-022-03466-x>
- 930 Maier-Hein, K. H., Neher, P. F., Houde, J. C., Côté, M. A., Garyfallidis, E., Zhong, J., Chamberland, M., Yeh, F. C., Lin, Y. C., Ji, Q., Reddick,

931 W. E., Glass, J. O., Chen, D. Q., Feng, Y., Gao, C., Wu, Y., Ma, J., Renjie, H., Li, Q., ... Descoteaux, M. (2017). The challenge of  
932 mapping the human connectome based on diffusion tractography. *Nature Communications*, 8(1). [https://doi.org/10.1038/s41467-017-](https://doi.org/10.1038/s41467-017-01285-x)  
933 01285-x

934 Mancini, M., Giulietti, G., Dowell, N., Spanò, B., Harrison, N., Bozzali, M., & Cercignani, M. (2018). Introducing axonal myelination in  
935 connectomics: A preliminary analysis of g-ratio distribution in healthy subjects. *NeuroImage*, 182, 351–359.  
936 <https://doi.org/10.1016/j.neuroimage.2017.09.018>

937 Mancini, M., Karakuzu, A., Cohen-Adad, J., Cercignani, M., Nichols, T. E., & Stikov, N. (2020). An interactive meta-analysis of MRI  
938 biomarkers of myelin. *ELife*, 9, 1–23. <https://doi.org/10.7554/eLife.61523>

939 Margulies, D. S., Ghosh, S. S., Goulas, A., Falkiewicz, M., Huntenburg, J. M., Langs, G., Bezgin, G., Eickhoff, S. B., Castellanos, F. X., Petrides,  
940 M., Jefferies, E., & Smallwood, J. (2016). Situating the default-mode network along a principal gradient of macroscale cortical  
941 organization. *Proceedings of the National Academy of Sciences of the United States of America*, 113(44), 12574–12579.  
942 <https://doi.org/10.1073/pnas.1608282113>

943 Marques, J. P., Kober, T., Krueger, G., van der Zwaag, W., Van de Moortele, P. F., & Gruetter, R. (2010). MP2RAGE, a self bias-field corrected  
944 sequence for improved segmentation and T1-mapping at high field. *NeuroImage*, 49(2), 1271–1281.  
945 <https://doi.org/10.1016/j.neuroimage.2009.10.002>

946 Maslov, S., & Sneppen, K. (2002). Specificity and stability in topology of protein networks. *Science*, 296(5569), 910–913.  
947 <https://doi.org/10.1126/science.1065103>

948 Messaritaki, E., Foley, S., Schiavi, S., Magazzini, L., Routley, B., Jones, D. K., & Singh, K. D. (2021). Predicting meg resting-state functional  
949 connectivity from microstructural information. *Network Neuroscience*, 5(2), 477–504. [https://doi.org/10.1162/netn\\_a\\_00187](https://doi.org/10.1162/netn_a_00187)

950 Moore, S., Meschkat, M., Ruhwedel, T., Trevisiol, A., Tzvetanova, I. D., Battefeld, A., Kusch, K., Kole, M. H. P., Strenke, N., Möbius, W., de  
951 Hoz, L., & Nave, K. A. (2020). A role of oligodendrocytes in information processing. *Nature Communications*, 11(1), 1–15.  
952 <https://doi.org/10.1038/s41467-020-19152-7>

953 Mottershead, J. P., Schmierer, K., Clemence, M., Thornton, J. S., Scaravilli, F., Barker, G. J., Tofts, P. S., Newcombe, J., Cuzner, M. L., Ordidge,  
954 R. J., McDonald, W. I., & Miller, D. H. (2003). High field MRI correlates of myelin content and axonal density in multiple sclerosis: A  
955 post-mortem study of the spinal cord. *Journal of Neurology*, 250(11), 1293–1301. <https://doi.org/10.1007/s00415-003-0192-3>

956 Mount, C. W., & Monje, M. (2017). Wrapped to Adapt: Experience-Dependent Myelination. *Neuron*, 95(4), 743–756.  
957 <https://doi.org/10.1016/j.neuron.2017.07.009>

958 Nave, K. A., & Werner, H. B. (2014). Myelination of the nervous system: Mechanisms and functions. *Annual Review of Cell and Developmental*  
959 *Biology*, 30, 503–533. <https://doi.org/10.1146/annurev-cellbio-100913-013101>

960 Patenaude, B., Smith, S. M., Kennedy, D. N., & Jenkinson, M. (2011). A Bayesian model of shape and appearance for subcortical brain  
961 segmentation. *NeuroImage*, 56(3), 907–922. <https://doi.org/10.1016/j.neuroimage.2011.02.046>

962 Pumphrey, R. J., & Young, J. Z. (1938). The Rates Of Conduction Of Nerve Fibres Of Various Diameters In Cephalopods. *Journal of*  
963 *Experimental Biology*, 15(4), 453–466. <https://doi.org/10.1242/jeb.15.4.453>

964 Raffelt, D., Smith, R., Ridgway, G., Tourmier, J. D., Vaughan, D., Rose, S., Henderson, R., & Connelly, A. (2015). Connectivity-based fixel  
965 enhancement: Whole-brain statistical analysis of diffusion MRI measures in the presence of crossing fibres. *NeuroImage*, 117, 40–55.

966 <https://doi.org/10.1016/j.neuroimage.2015.05.039>

967 Raffelt, D., Tournier, J. D., Smith, R., Vaughan, D., Jackson, G., Ridgway, G., & Connelly, A. (2017). Investigating white matter fibre density

968 and morphology using fixel-based analysis. *NeuroImage*, *144*, 58–73. <https://doi.org/10.1016/j.neuroimage.2016.09.029>

969 Royer, J., Rodríguez-Cruces, R., Tavakol, S., Larivière, S., Herholz, P., Li, Q., Vos de Wael, R., Paquola, C., Benkarim, O., Park, B., Lowe, A. J.,

970 Margulies, D., Smallwood, J., Bernasconi, A., Bernasconi, N., Frauscher, B., & Bernhardt, B. C. (2022). An Open MRI Dataset For

971 Multiscale Neuroscience. *Scientific Data*, *9*(1), 569. <https://doi.org/10.1038/s41597-022-01682-y>

972 Rubinov, M., & Sporns, O. (2010). Complex network measures of brain connectivity: Uses and interpretations. *NeuroImage*, *52*(3), 1059–1069.

973 <https://doi.org/10.1016/j.neuroimage.2009.10.003>

974 Salimi-Khorshidi, G., Douaud, G., Beckmann, C. F., Glasser, M. F., Griffanti, L., & Smith, S. M. (2014). Automatic denoising of functional MRI

975 data: Combining independent component analysis and hierarchical fusion of classifiers. *NeuroImage*, *90*, 449–468.

976 <https://doi.org/10.1016/j.neuroimage.2013.11.046>

977 Schaefer, A., Kong, R., Gordon, E. M., Laumann, T. O., Zuo, X.-N., Holmes, A. J., Eickhoff, S. B., & Yeo, B. T. T. (2018). Local-Global

978 Parcellation of the Human Cerebral Cortex from Intrinsic Functional Connectivity MRI. *Cerebral Cortex*, *28*(9), 3095–3114.

979 <https://doi.org/10.1093/cercor/bhx179>

980 Schiavi, S., Lu, P., Weigel, M., Lutti, A., Jones, D. K., Kappos, L., Granziera, C., & Daducci, A. (2022). Bundle Myelin Fraction (BMF)

981 Mapping of Different White Matter Connections Using Microstructure Informed Tractography. *NeuroImage*, 118922.

982 <https://doi.org/10.1016/j.neuroimage.2022.118922>

983 Schiavi, S., Petracca, M., Battocchio, M., El Mendili, M. M., Paduri, S., Fleysher, L., Inglese, M., & Daducci, A. (2020). Sensory-motor network

984 topology in multiple sclerosis: Structural connectivity analysis accounting for intrinsic density discrepancy. *Human Brain Mapping*,

985 *41*(11), 2951–2963. <https://doi.org/10.1002/hbm.24989>

986 Schilling, K. G., Daducci, A., Maier-Hein, K., Poupon, C., Houde, J. C., Nath, V., Anderson, A. W., Landman, B. A., & Descoteaux, M. (2019).

987 Challenges in diffusion MRI tractography – Lessons learned from international benchmark competitions. *Magnetic Resonance Imaging*,

988 *57*(November 2018), 194–209. <https://doi.org/10.1016/j.mri.2018.11.014>

989 Smith, R. E., Tournier, J. D., Calamante, F., & Connelly, A. (2012). Anatomically-constrained tractography: Improved diffusion MRI streamlines

990 tractography through effective use of anatomical information. *NeuroImage*, *62*(3), 1924–1938.

991 <https://doi.org/10.1016/j.neuroimage.2012.06.005>

992 Smith, R. E., Tournier, J. D., Calamante, F., & Connelly, A. (2015). SIFT2: Enabling dense quantitative assessment of brain white matter

993 connectivity using streamlines tractography. *NeuroImage*, *119*, 338–351. <https://doi.org/10.1016/j.neuroimage.2015.06.092>

994 Smith, S. M., Fox, P. T., Miller, K. L., Glahn, D. C., Fox, P. M., Mackay, C. E., Filippini, N., Watkins, K. E., Toro, R., Laird, A. R., &

995 Beckmann, C. F. (2009). Correspondence of the brain’s functional architecture during activation and rest. *Proceedings of the National*

996 *Academy of Sciences of the United States of America*, *106*(31), 13040–13045. <https://doi.org/10.1073/pnas.0905267106>

997 Smith, S. M., Jenkinson, M., Woolrich, M. W., Beckmann, C. F., Behrens, T. E. J., Johansen-Berg, H., Bannister, P. R., De Luca, M., Drobnjak,

998 I., Flitney, D. E., Niazy, R. K., Saunders, J., Vickers, J., Zhang, Y., De Stefano, N., Brady, J. M., & Matthews, P. M. (2004). Advances in

999 functional and structural MR image analysis and implementation as FSL. *NeuroImage*, *23*(SUPPL. 1), 208–219.

1000 <https://doi.org/10.1016/j.neuroimage.2004.07.051>

- 1001 Sorrentino, P., Petkoski, S., Sparaco, M., Troisi Lopez, E., Signoriello, E., Baselice, F., Bonavita, S., Pirozzi, M. A., Quarantelli, M., Sorrentino,  
1002 G., & Jirsa, V. (2022). Whole-Brain Propagation Delays in Multiple Sclerosis, a Combined Tractography-Magnetoencephalography  
1003 Study. *The Journal of Neuroscience : The Official Journal of the Society for Neuroscience*, *42*(47), 8807–8816.  
1004 <https://doi.org/10.1523/JNEUROSCI.0938-22.2022>
- 1005 Sotiropoulos, S. N., & Zalesky, A. (2019). Building connectomes using diffusion MRI: why, how and but. In *NMR in Biomedicine* (Vol. 32, Issue  
1006 4). <https://doi.org/10.1002/nbm.3752>
- 1007 Sporns, O. (2010). Networks of the Brain. In *Networks of the Brain*. The MIT Press. <https://doi.org/10.7551/mitpress/8476.001.0001>
- 1008 Sporns, O. (2011). The human connectome: A complex network. *Annals of the New York Academy of Sciences*, *1224*(1), 109–125.  
1009 <https://doi.org/10.1111/j.1749-6632.2010.05888.x>
- 1010 Sporns, O. (2018). Graph theory methods: applications in brain networks. *Dialogues in Clinical Neuroscience*, *20*(2), 111–120.  
1011 <https://doi.org/10.31887/DCNS.2018.20.2/osporns>
- 1012 Stikov, N., Campbell, J. S. W., Stroh, T., Lavelée, M., Frey, S., Novek, J., Nuara, S., Ho, M. K., Bedell, B. J., Dougherty, R. F., Leppert, I. R.,  
1013 Boudreau, M., Narayanan, S., Duval, T., Cohen-Adad, J., Picard, P. A., Gasecka, A., Côté, D., & Pike, G. B. (2015). In vivo histology of  
1014 the myelin g-ratio with magnetic resonance imaging. *NeuroImage*, *118*, 397–405. <https://doi.org/10.1016/j.neuroimage.2015.05.023>
- 1015 Stikov, N., Pery, L. M., Mezer, A., Rykhlevskaia, E., Wandell, B. A., Pauly, J. M., & Dougherty, R. F. (2011). Bound pool fractions complement  
1016 diffusion measures to describe white matter micro and macrostructure. *NeuroImage*, *54*(2), 1112–1121.  
1017 <https://doi.org/10.1016/j.neuroimage.2010.08.068>
- 1018 Suárez, L. E., Markello, R. D., Betzel, R. F., & Misisic, B. (2020). Linking Structure and Function in Macroscale Brain Networks. *Trends in*  
1019 *Cognitive Sciences*. <https://doi.org/10.1016/j.tics.2020.01.008>
- 1020 Thomas Yeo, B. T., Krienen, F. M., Sepulcre, J., Sabuncu, M. R., Lashkari, D., Hollinshead, M., Roffman, J. L., Smoller, J. W., Zöllei, L.,  
1021 Polimeni, J. R., Fisch, B., Liu, H., & Buckner, R. L. (2011). The organization of the human cerebral cortex estimated by intrinsic  
1022 functional connectivity. *Journal of Neurophysiology*, *106*(3), 1125–1165. <https://doi.org/10.1152/jn.00338.2011>
- 1023 Tournier, J.-D., Calamante, F., & Connelly, A. (2010). Improved probabilistic streamlines tractography by 2 nd order integration over fibre  
1024 orientation distributions. *Isrmr*, *88*(2003), 2010. [https://cds.ismrm.org/protected/10MProceedings/PDFfiles/1670\\_4298.pdf](https://cds.ismrm.org/protected/10MProceedings/PDFfiles/1670_4298.pdf)
- 1025 Tournier, J. Donald, Calamante, F., & Connelly, A. (2012). MRtrix: Diffusion tractography in crossing fiber regions. *International Journal of*  
1026 *Imaging Systems and Technology*, *22*(1), 53–66. <https://doi.org/10.1002/ima.22005>
- 1027 Tournier, J. Donald, Smith, R., Raffelt, D., Tabbara, R., Dhollander, T., Pietsch, M., Christiaens, D., Jeurissen, B., Yeh, C. H., & Connelly, A.  
1028 (2019). MRtrix3: A fast, flexible and open software framework for medical image processing and visualisation. *NeuroImage*, *202*.  
1029 <https://doi.org/10.1016/j.neuroimage.2019.116137>
- 1030 Tournier, Jacques Donald, Mori, S., & Leemans, A. (2011). Diffusion tensor imaging and beyond. *Magnetic Resonance in Medicine*, *65*(6),  
1031 1532–1556. <https://doi.org/10.1002/mrm.22924>
- 1032 Tustison, N. J., Avants, B. B., Cook, P. A., Zheng, Y., Egan, A., Yushkevich, P. A., & Gee, J. C. (2010). N4ITK: Improved N3 bias correction.  
1033 *IEEE Transactions on Medical Imaging*, *29*(6), 1310–1320. <https://doi.org/10.1109/TMI.2010.2046908>
- 1034 van den Heuvel, M. P., Mandl, R. C. W., Stam, C. J., Kahn, R. S., & Hulshoff Pol, H. E. (2010). Aberrant Frontal and Temporal Complex  
1035 Network Structure in Schizophrenia: A Graph Theoretical Analysis. *Journal of Neuroscience*, *30*(47), 15915–15926.

- 1036 <https://doi.org/10.1523/JNEUROSCI.2874-10.2010>
- 1037 Van Den Heuvel, Martijn P., Kahn, R. S., Goñi, J., & Sporns, O. (2012). High-cost, high-capacity backbone for global brain communication.
- 1038 *Proceedings of the National Academy of Sciences of the United States of America*, 109(28), 11372–11377.
- 1039 <https://doi.org/10.1073/pnas.1203593109>
- 1040 van den Heuvel, Martijn P., & Sporns, O. (2011). Rich-club organization of the human connectome. *Journal of Neuroscience*, 31(44), 15775–
- 1041 15786. <https://doi.org/https://doi.org/10.1523/JNEUROSCI.3539-11.2011>
- 1042 van den Heuvel, Martijn P., & Sporns, O. (2013). An anatomical substrate for integration among functional networks in human cortex. *Journal of*
- 1043 *Neuroscience*, 33(36), 14489–14500. <https://doi.org/10.1523/JNEUROSCI.2128-13.2013>
- 1044 Van Den Heuvel, Martijn P., Stam, C. J., Kahn, R. S., & Hulshoff Pol, H. E. (2009). Efficiency of functional brain networks and intellectual
- 1045 performance. *Journal of Neuroscience*, 29(23), 7619–7624. <https://doi.org/10.1523/JNEUROSCI.1443-09.2009>
- 1046 Veraart, J., Fieremans, E., & Novikov, D. S. (2016). Diffusion MRI noise mapping using random matrix theory. *Magnetic Resonance in*
- 1047 *Medicine*, 76(5), 1582–1593. <https://doi.org/10.1002/mrm.26059>
- 1048 Veraart, J., Novikov, D. S., Christiaens, D., Ades-aron, B., Sijbers, J., & Fieremans, E. (2016). Denoising of diffusion MRI using random matrix
- 1049 theory. *NeuroImage*, 142, 394–406. <https://doi.org/10.1016/j.neuroimage.2016.08.016>
- 1050 Vos de Wael, R., Benkarim, O., Paquola, C., Larivière, S., Royer, J., Tavakol, S., Xu, T., Hong, S. J., Langs, G., Valk, S., Masic, B., Milham, M.,
- 1051 Margulies, D. S., Smallwood, J., & Bernhardt, B. C. (2020). BrainSpace: a toolbox for the analysis of macroscale gradients in
- 1052 neuroimaging and connectomics datasets. *Communications Biology*, 3(1). <https://doi.org/10.1038/s42003-020-0794-7>
- 1053 Wang, P., Kong, R., Kong, X., Liégeois, R., Orban, C., Deco, G., van den Heuvel, M. P., & Thomas Yeo, B. T. (2019). Inversion of a large-scale
- 1054 circuit model reveals a cortical hierarchy in the dynamic resting human brain. *Science Advances*, 5(1).
- 1055 <https://doi.org/10.1126/sciadv.aat7854>
- 1056 Xia, M., Wang, J., & He, Y. (2013). BrainNet Viewer: A Network Visualization Tool for Human Brain Connectomics. *PLoS ONE*, 8(7).
- 1057 <https://doi.org/10.1371/journal.pone.0068910>
- 1058 Yeh, C. H., Smith, R. E., Liang, X., Calamante, F., & Connelly, A. (2016). Correction for diffusion MRI fibre tracking biases: The consequences
- 1059 for structural connectomic metrics. *NeuroImage*, 142, 150–162. <https://doi.org/10.1016/j.neuroimage.2016.05.047>
- 1060 Yeh, F. C., Badre, D., & Verstynen, T. (2016). Connectometry: A statistical approach harnessing the analytical potential of the local connectome.
- 1061 *NeuroImage*, 125, 162–171. <https://doi.org/10.1016/j.neuroimage.2015.10.053>
- 1062 Zalesky, A., Fornito, A., Cocchi, L., Gollo, L. L., van den Heuvel, M. P., & Breakspear, M. (2016). Connectome sensitivity or specificity: which
- 1063 is more important? *NeuroImage*, 142, 407–420. <https://doi.org/10.1016/j.neuroimage.2016.06.035>
- 1064 Zhang, H., Schneider, T., Wheeler-Kingshott, C. A., & Alexander, D. C. (2012). NODDI: Practical in vivo neurite orientation dispersion and
- 1065 density imaging of the human brain. *NeuroImage*, 61(4), 1000–1016. <https://doi.org/10.1016/j.neuroimage.2012.03.072>
- 1066 Zhang, Y., Brady, M., & Smith, S. (2001). Segmentation of brain MR images through a hidden Markov random field model and the expectation-
- 1067 maximization algorithm. *IEEE Transactions on Medical Imaging*, 20(1), 45–57. <https://doi.org/10.1109/42.906424>
- 1068

Figure 1

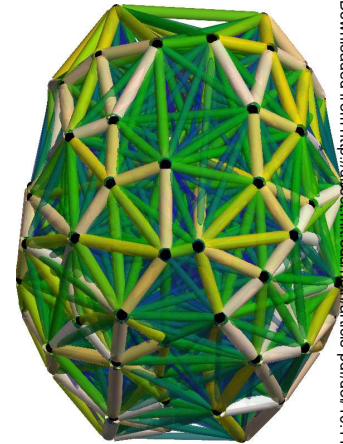
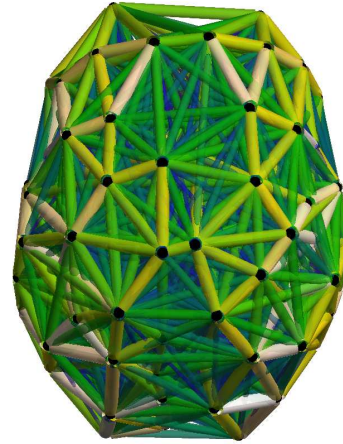
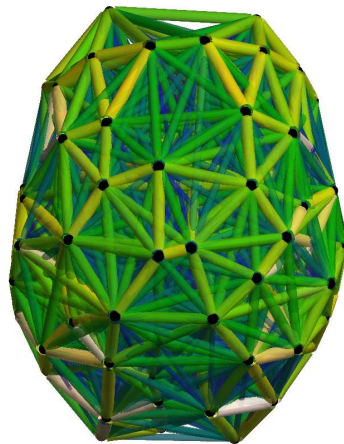
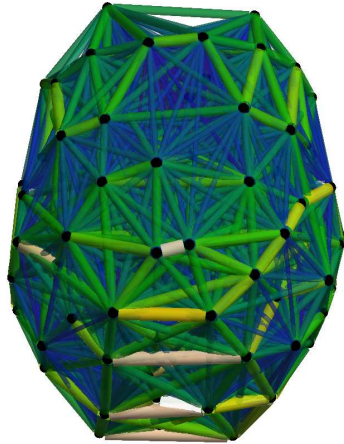
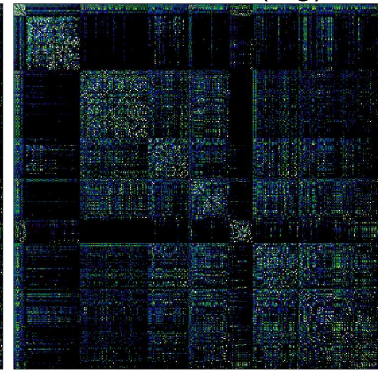
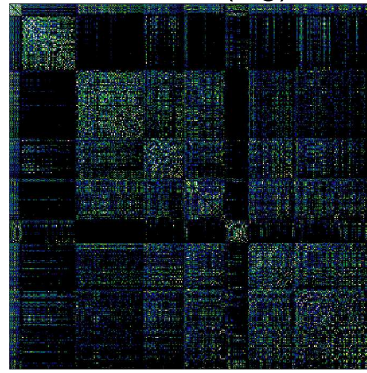
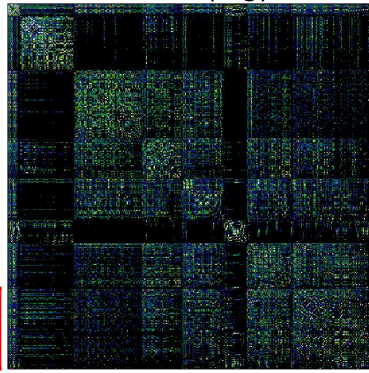
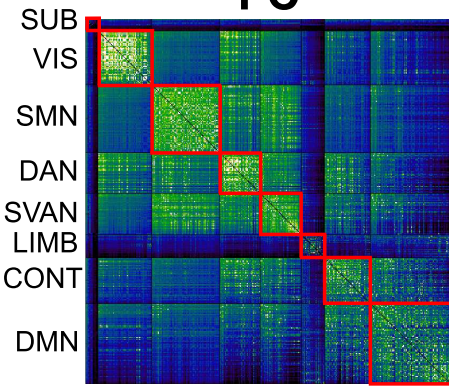
### Group Edge Weights

**FC**

**NoS(log)**

**SIFT2(log)**

**COMMIT(log)**

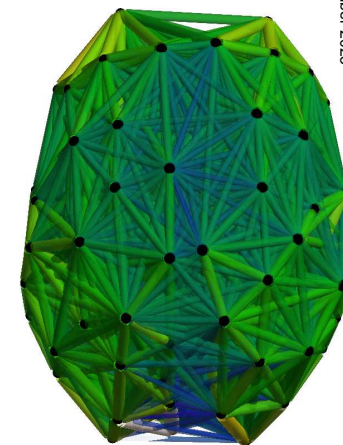
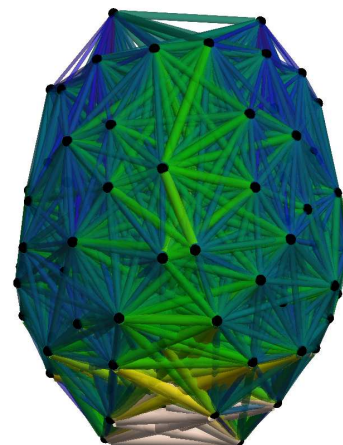
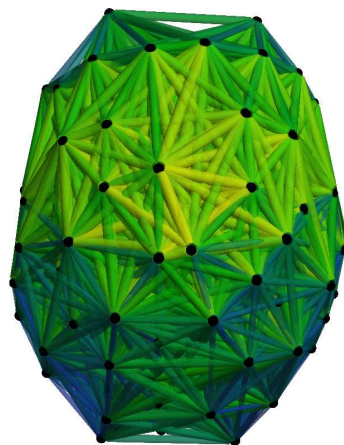
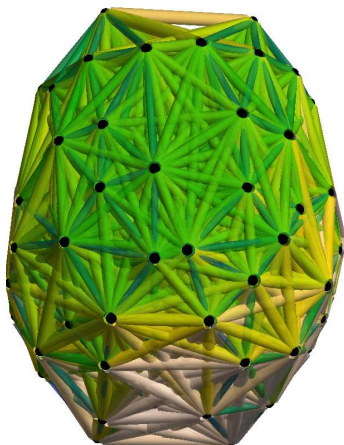
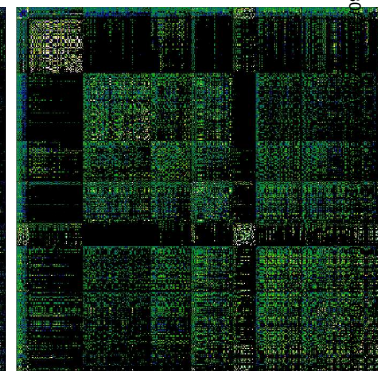
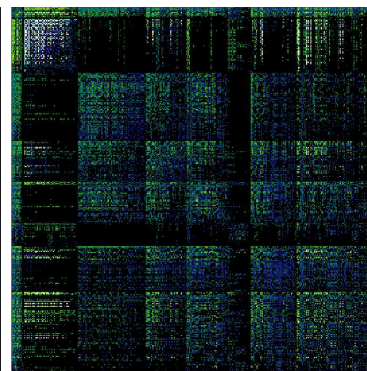
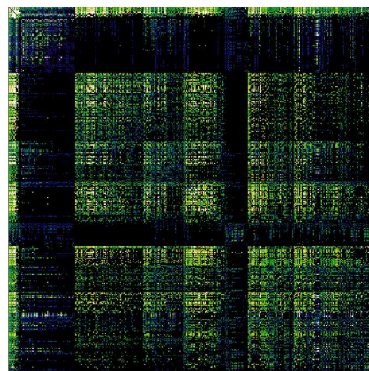
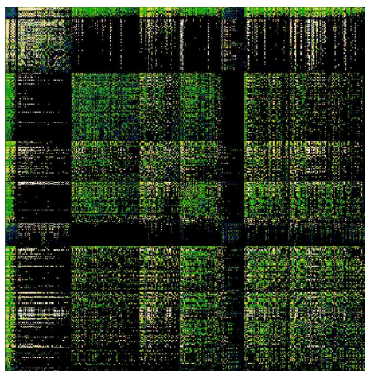


**R1**

**ICVF**

**FA**

**RD**

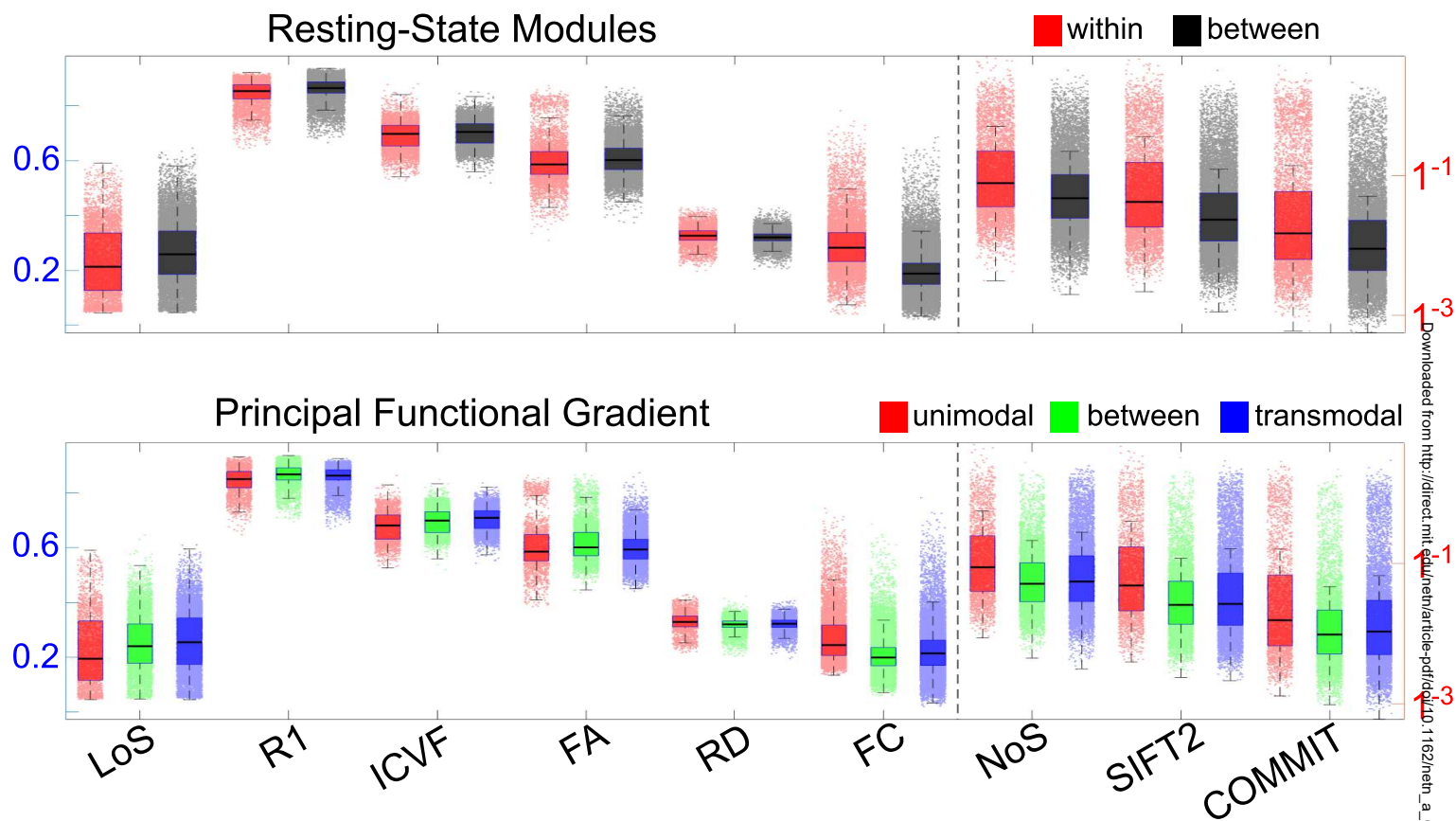


min  max

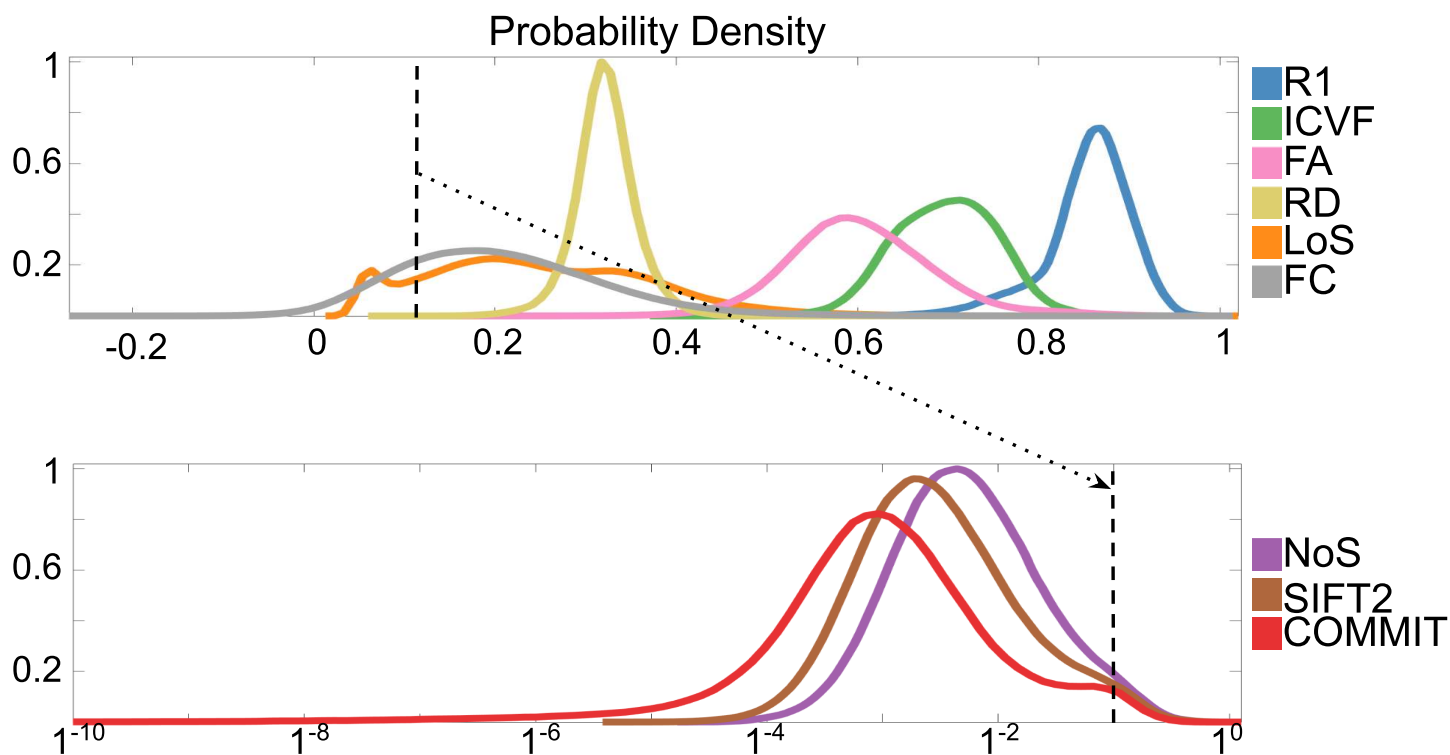


Figure 2

## A group edge weights



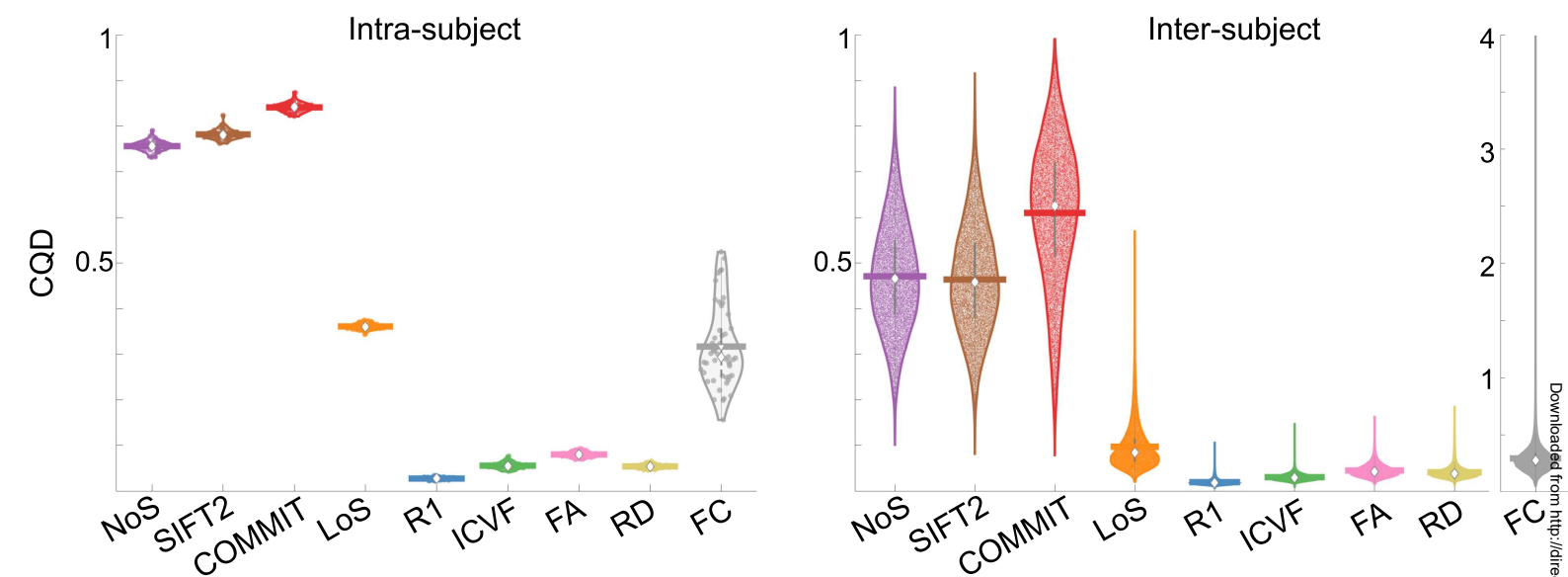
## B subject edge weights



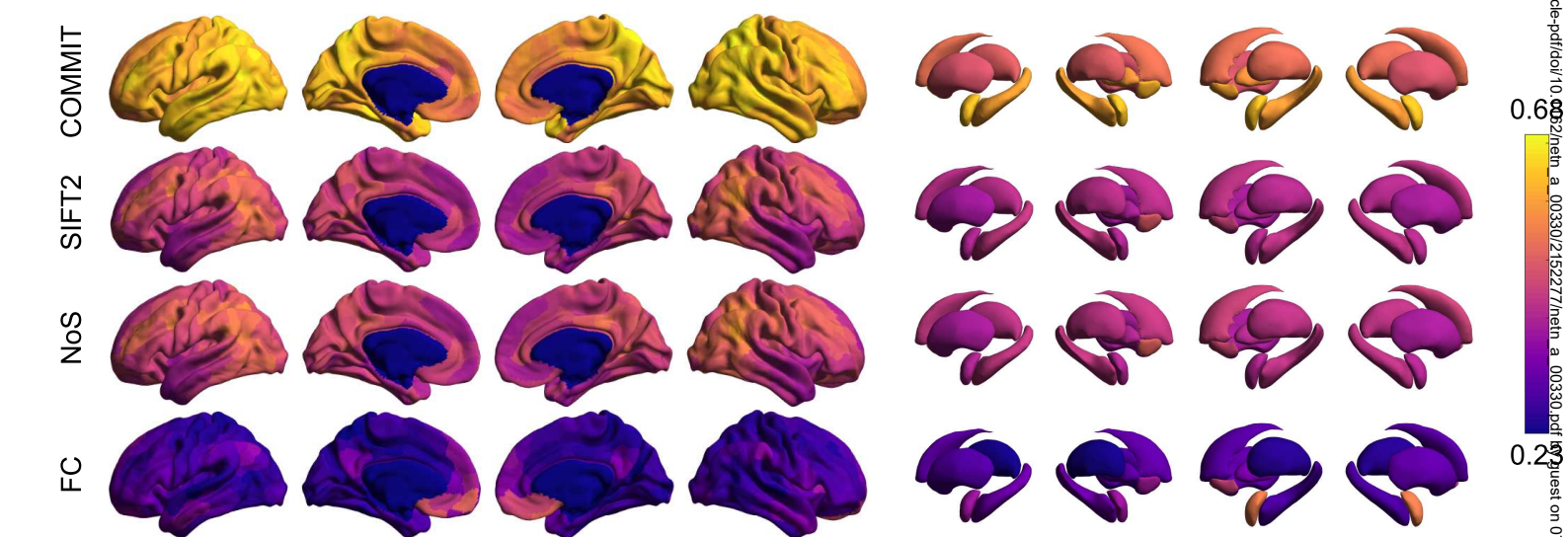
Downloaded from [http://direct.mit.edu/neh/article-pdf/d010\\_1162/neh\\_a\\_00330/215227/neh\\_a\\_00330.pdf](http://direct.mit.edu/neh/article-pdf/d010_1162/neh_a_00330/215227/neh_a_00330.pdf) by guest on 07 September 2023

Figure 3

**A** subject edge weight variability



**B** edgewise mean inter-subject variance



**C** group edge weight variance across edge length bins

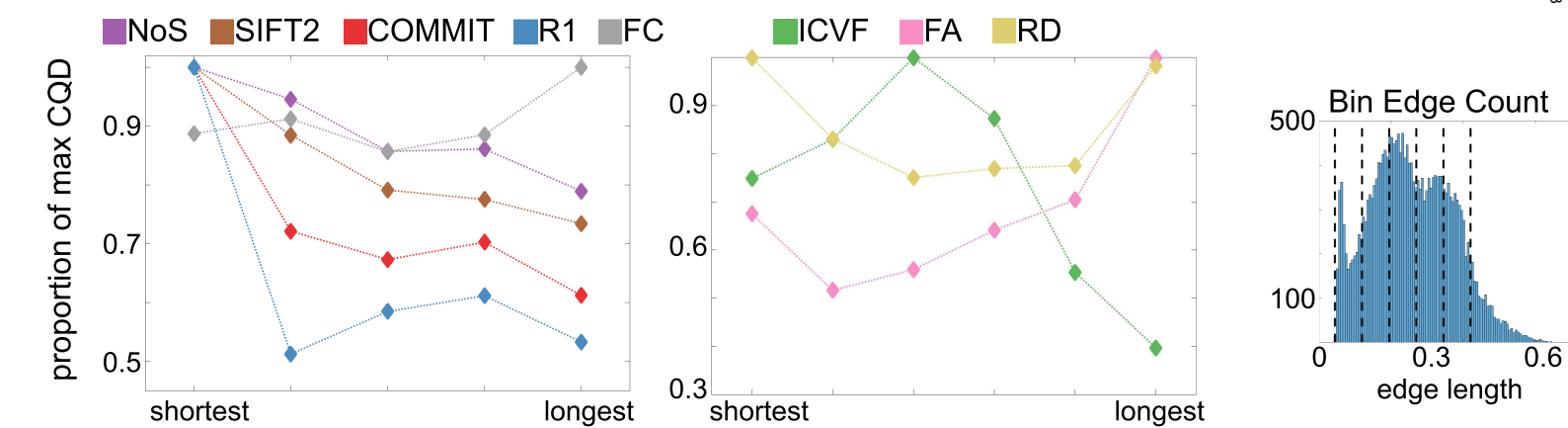
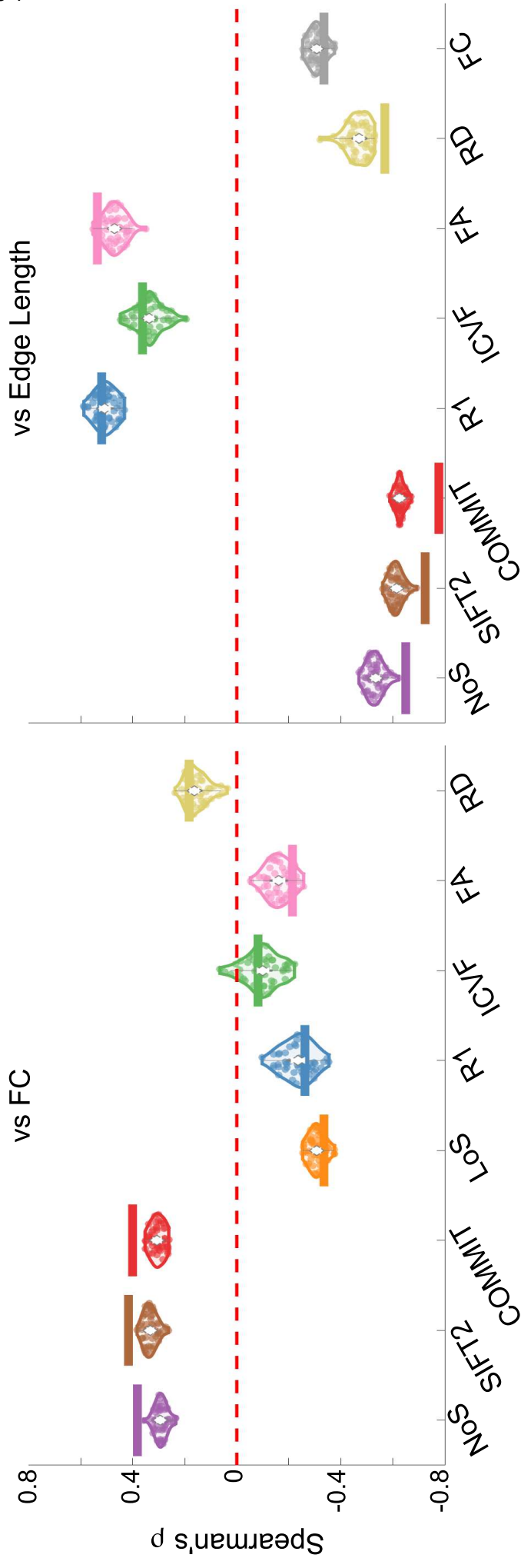


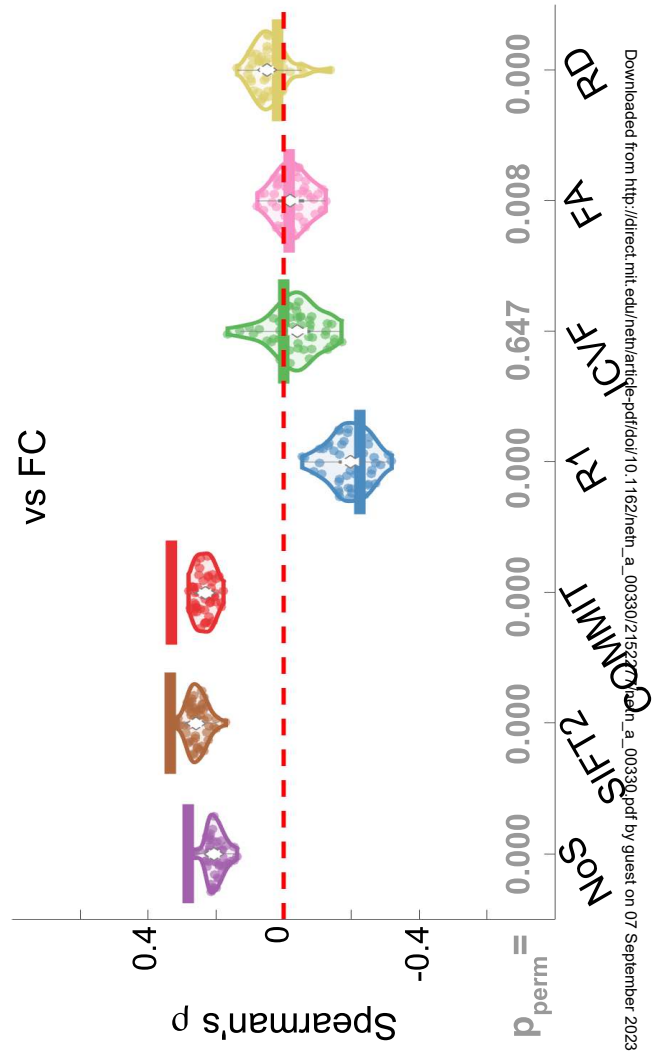
Figure 4

A edge weight correlations

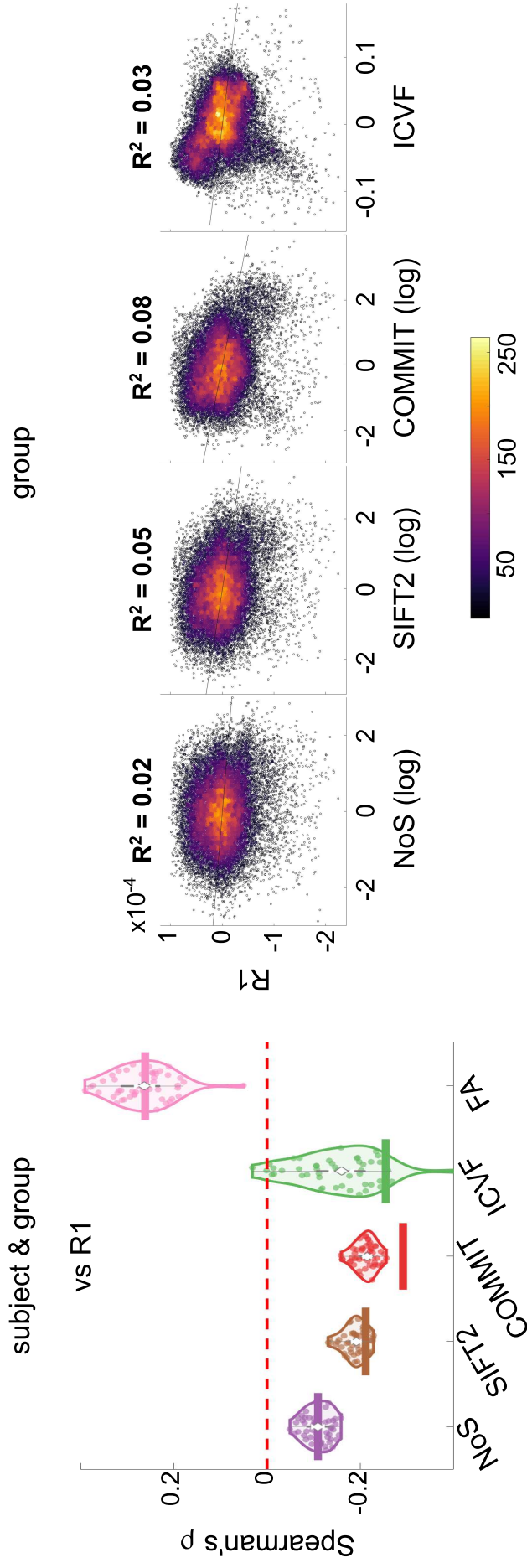


regress edge length

B residual edge weight correlations



**A** residual edge weight correlations



**B** R1 vs COMMIT across edge length bins

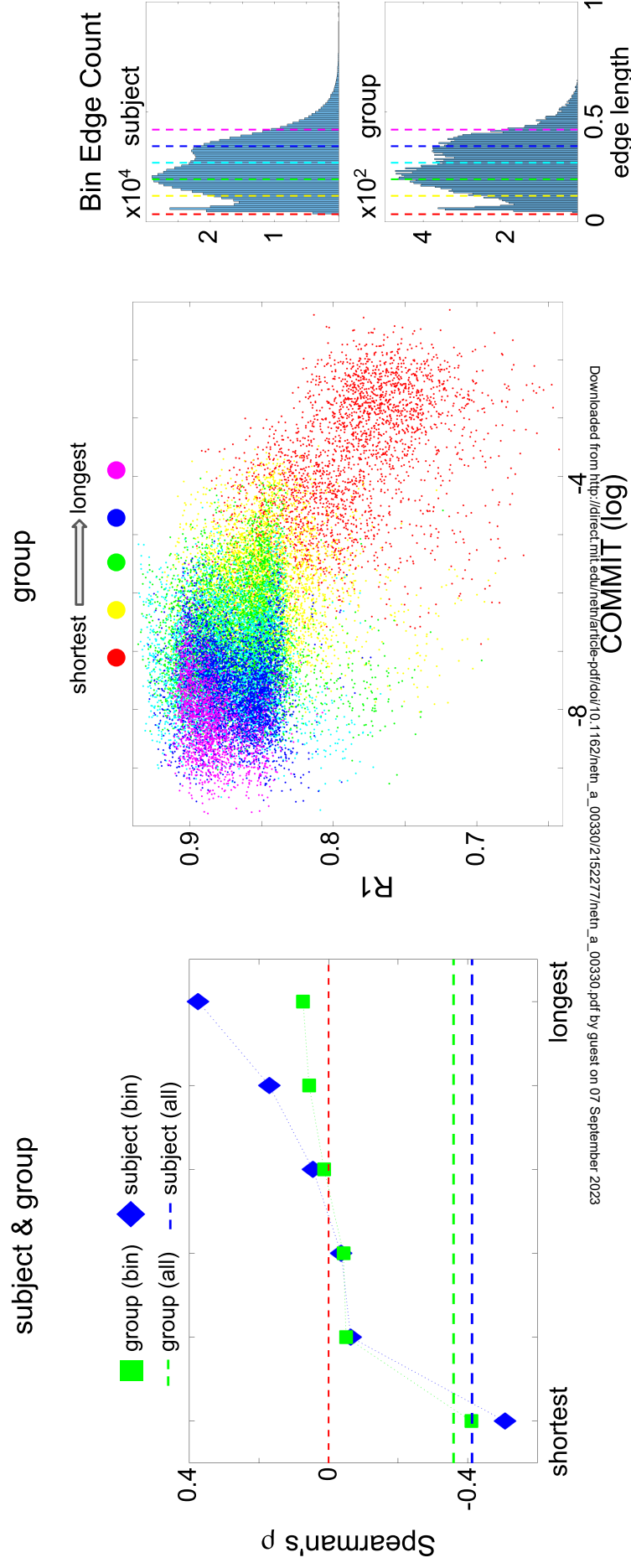
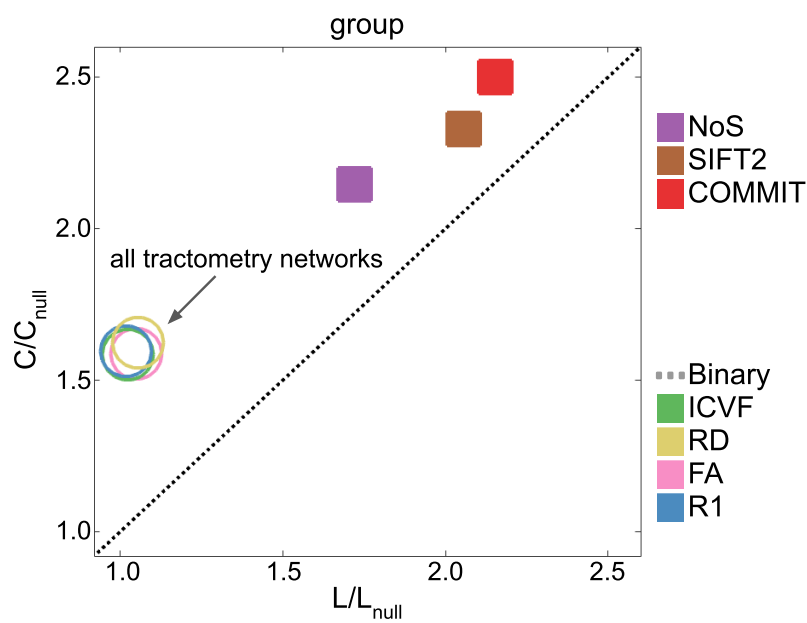
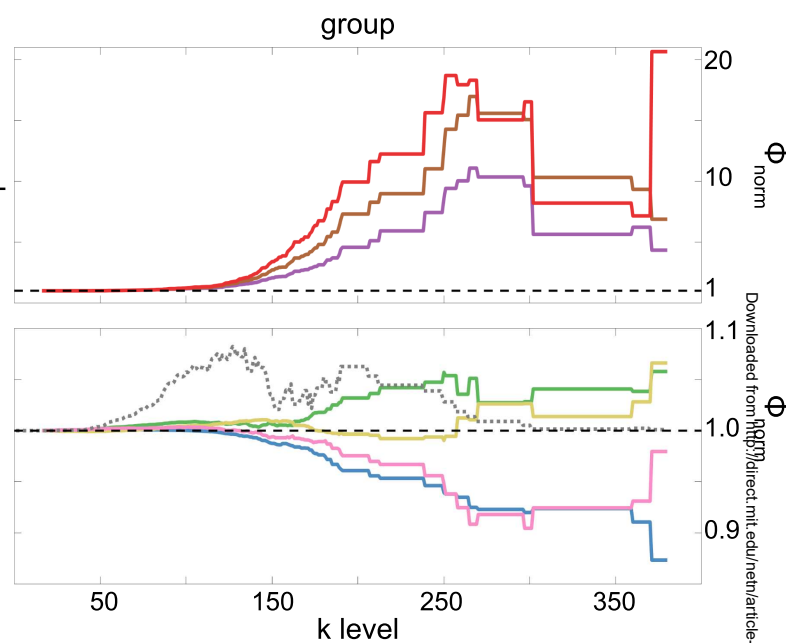


Figure 6

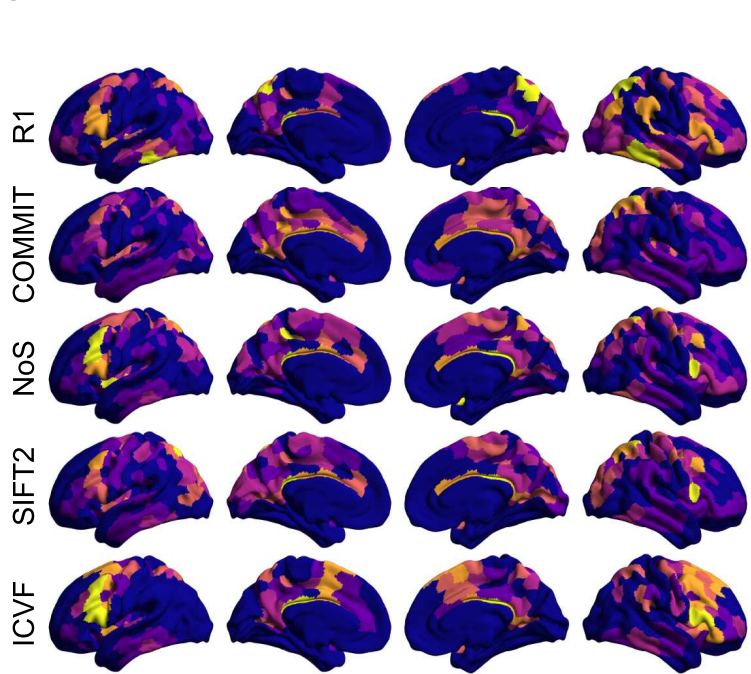
**A** normalized small-worldness



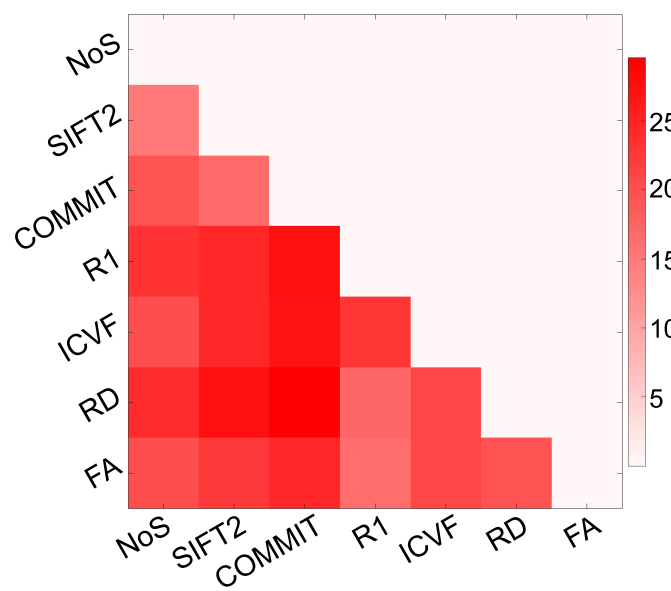
**B** normalized rich club



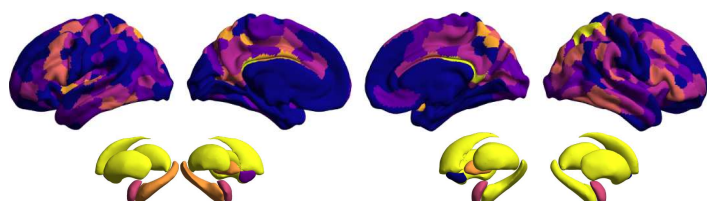
**C** normalized hubness



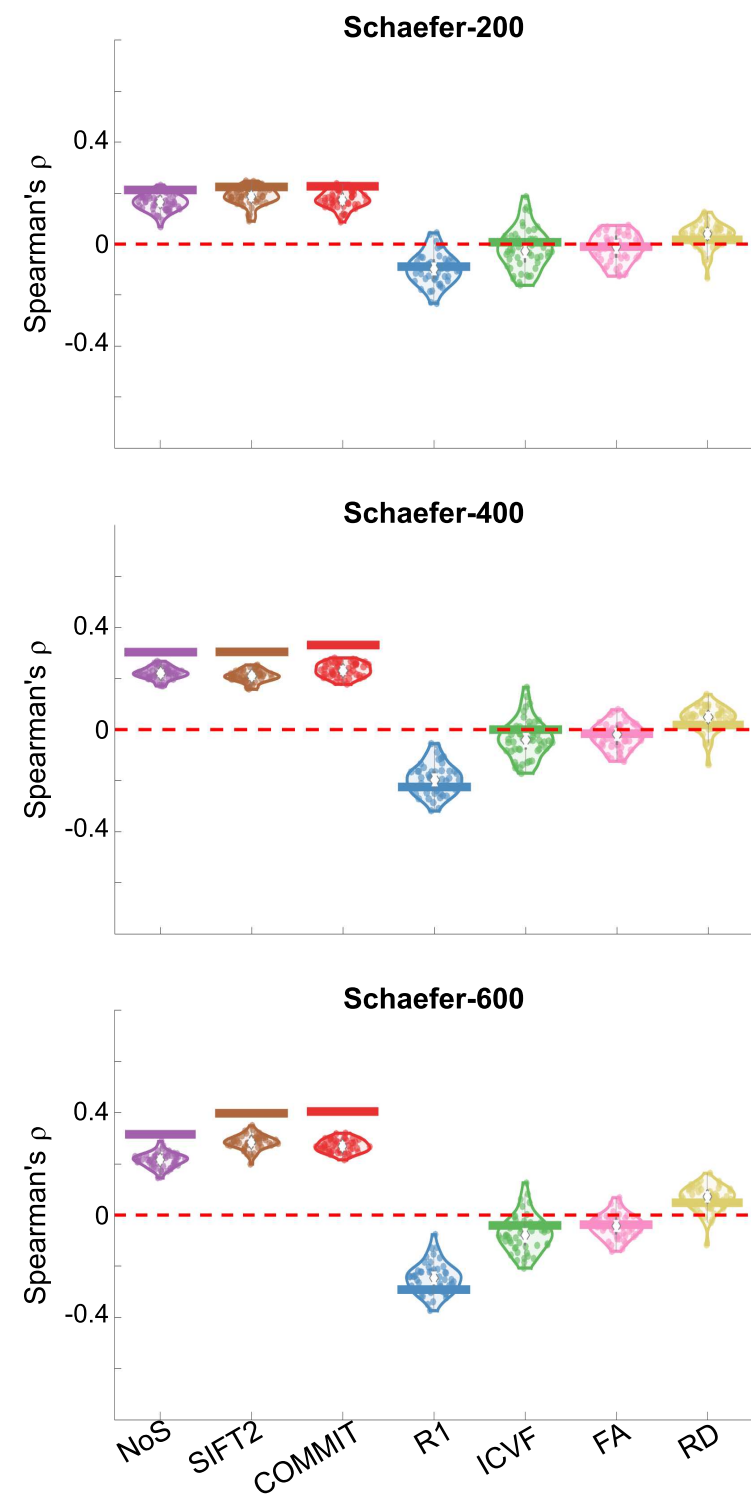
Hubness Euclidean Distance



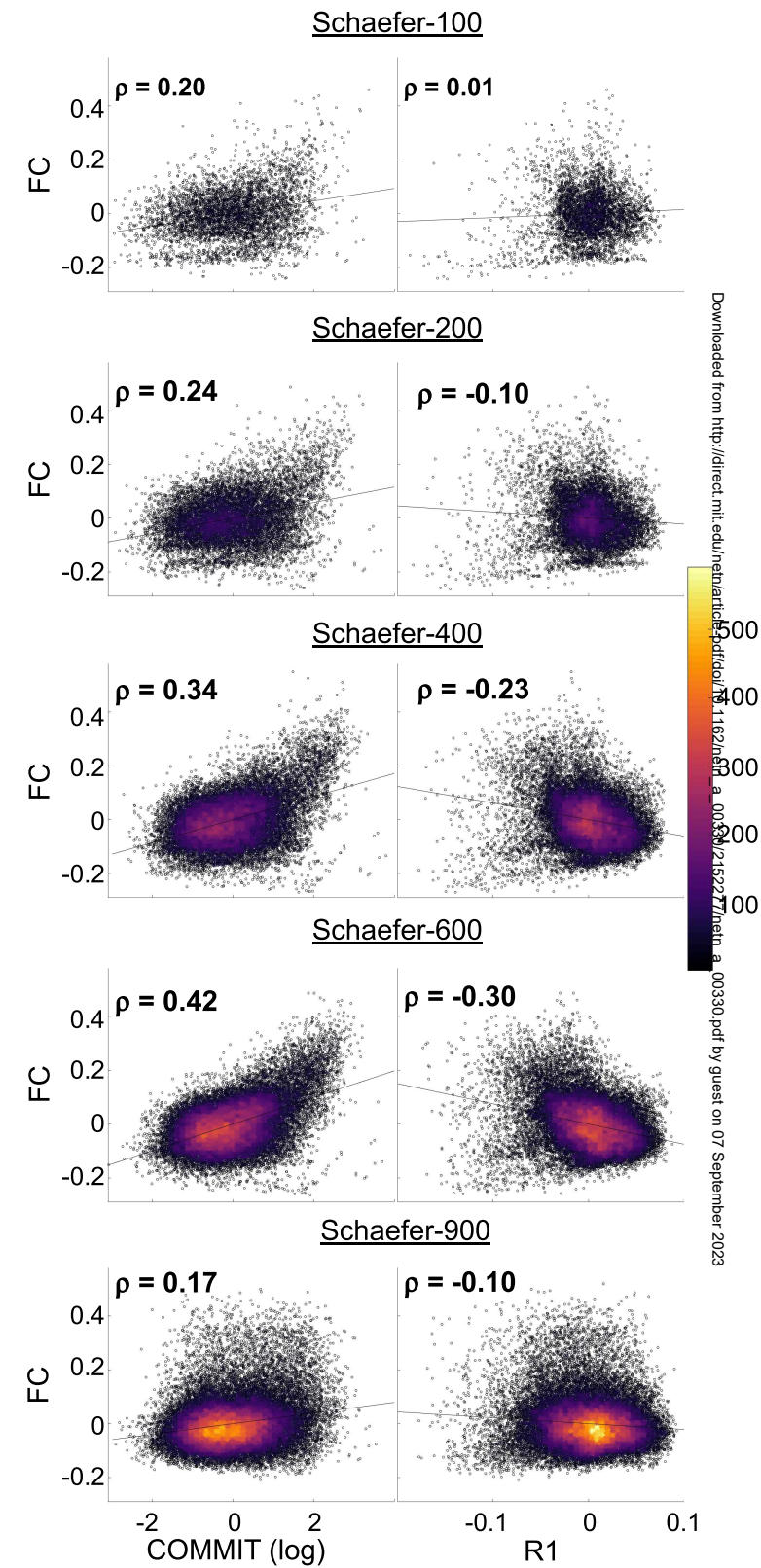
average COMMIT & R1



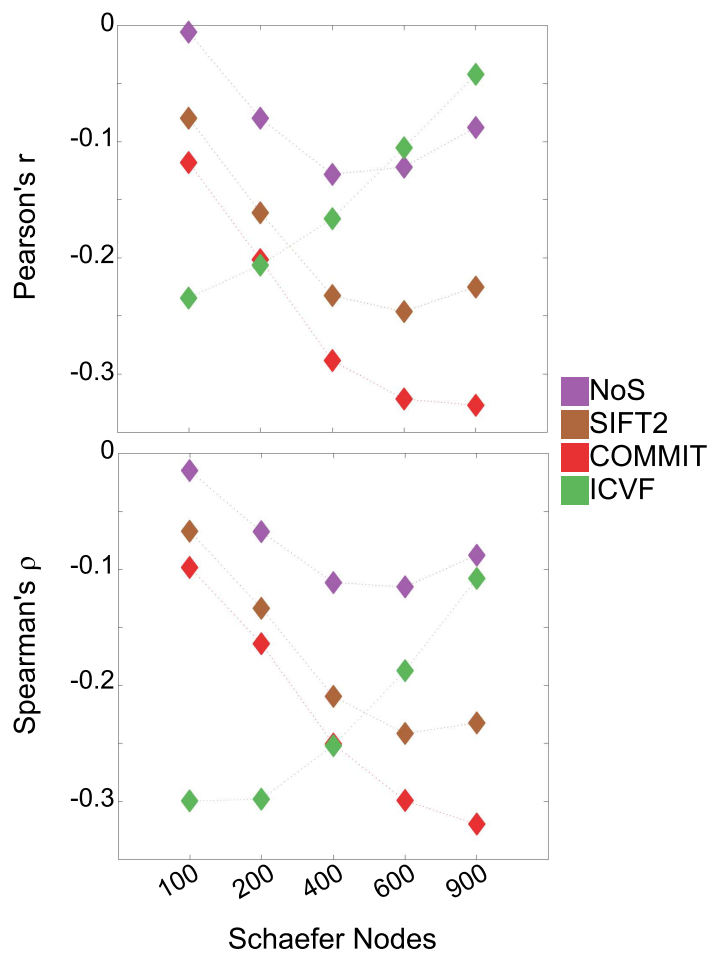
A group &amp; subject residual edge weight correlations with FC



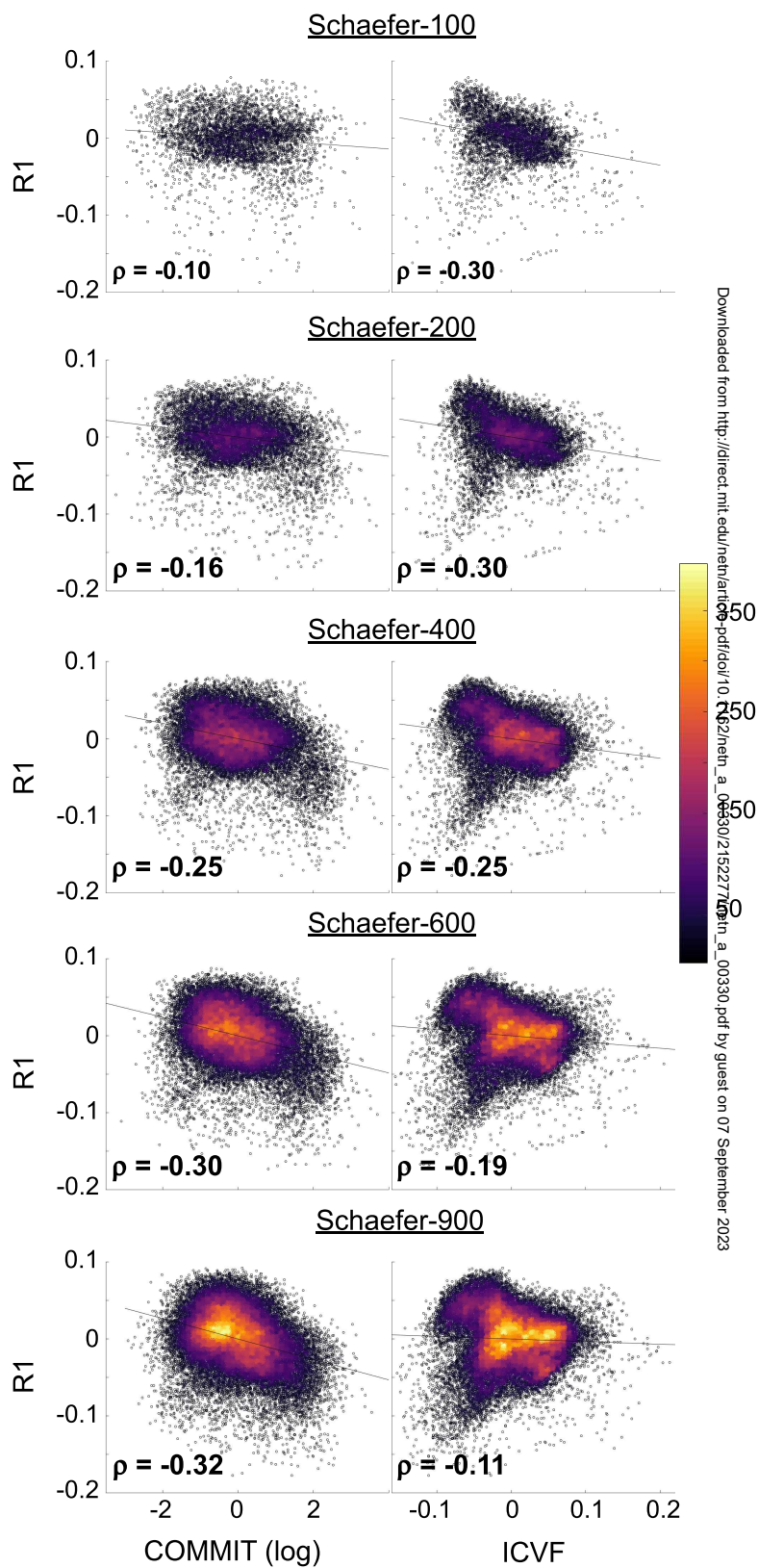
B group residual edge weights



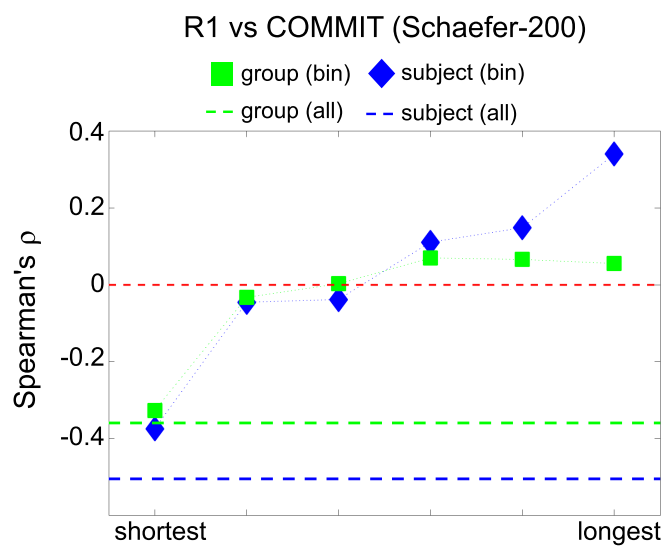
**A** group residual edge weight correlations with R1



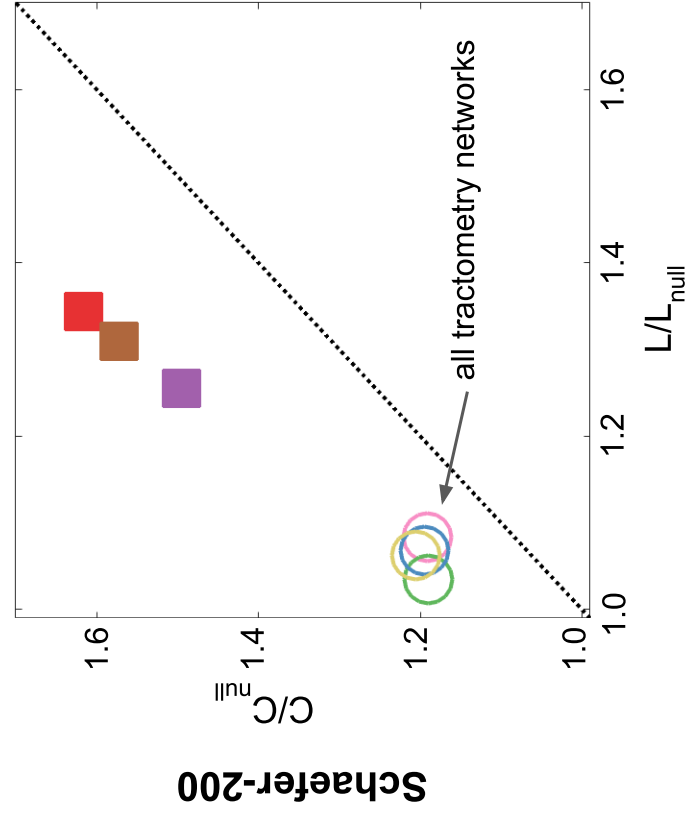
**B** group residual edge weights



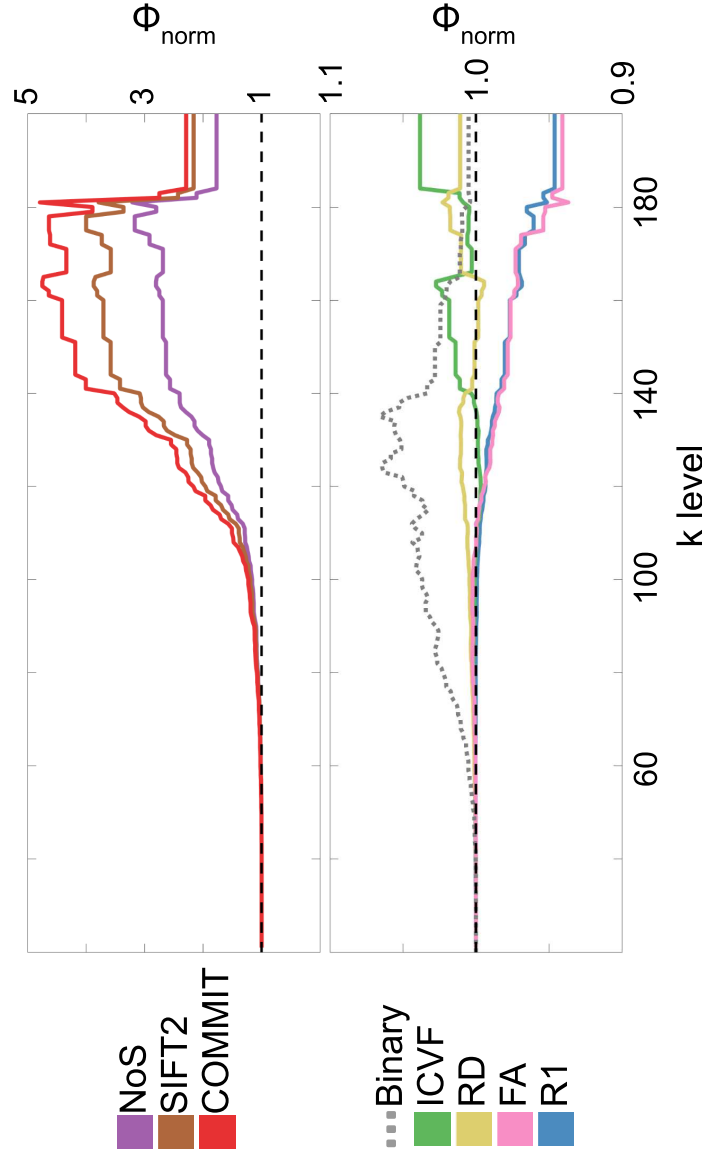
**C** edge weight correlations across edge length bins



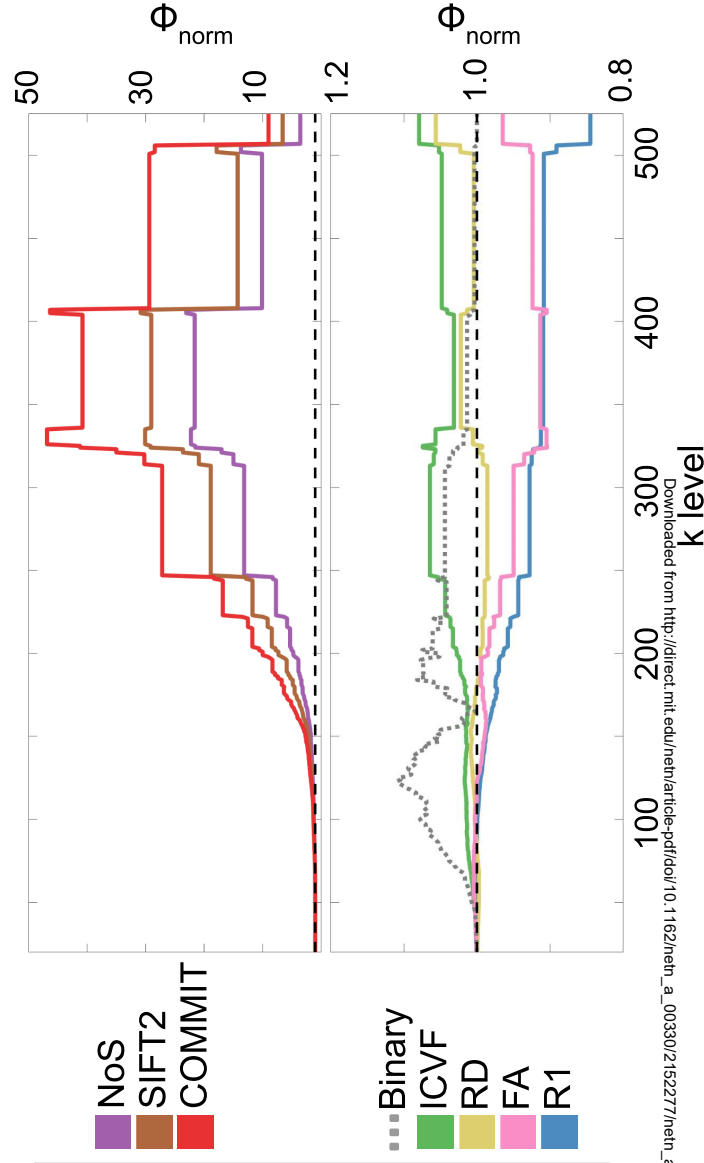
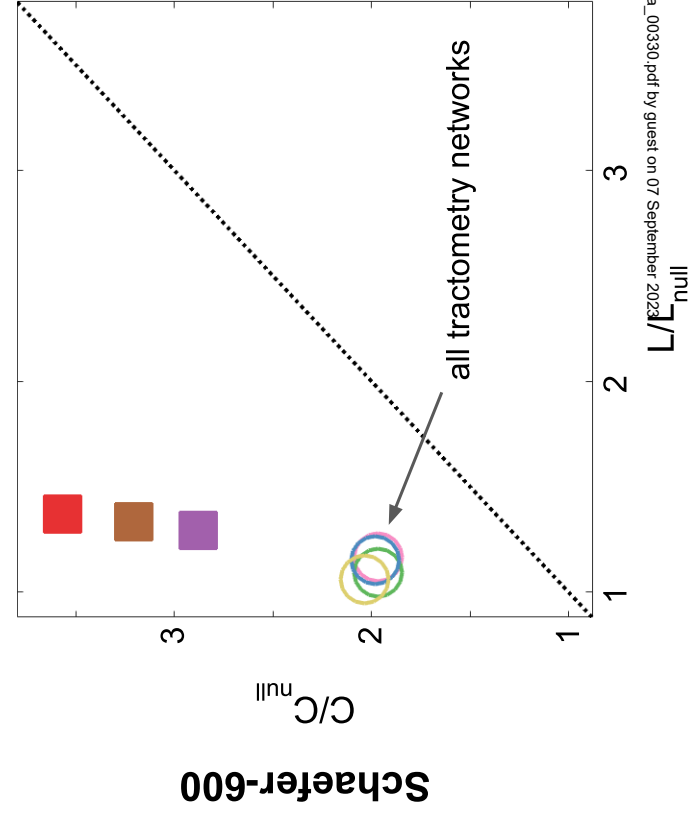
A group normalized small-worldness



B group normalized rich club



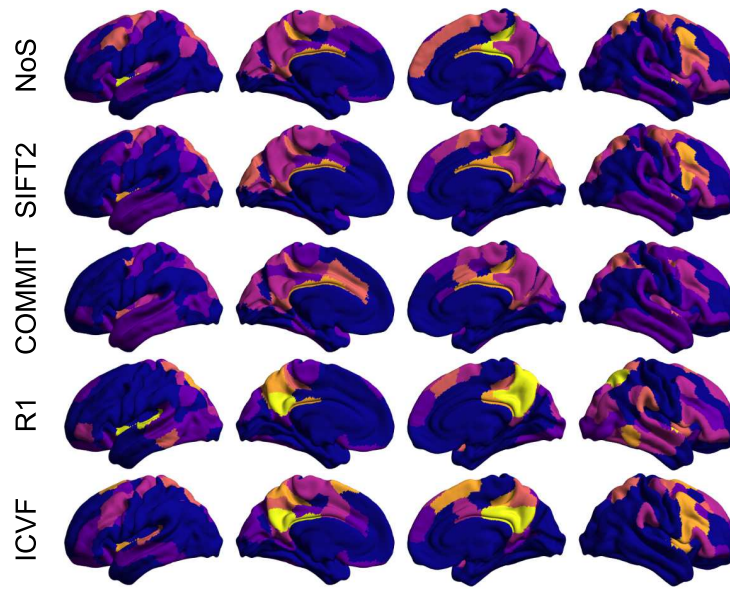
Schaefer-600



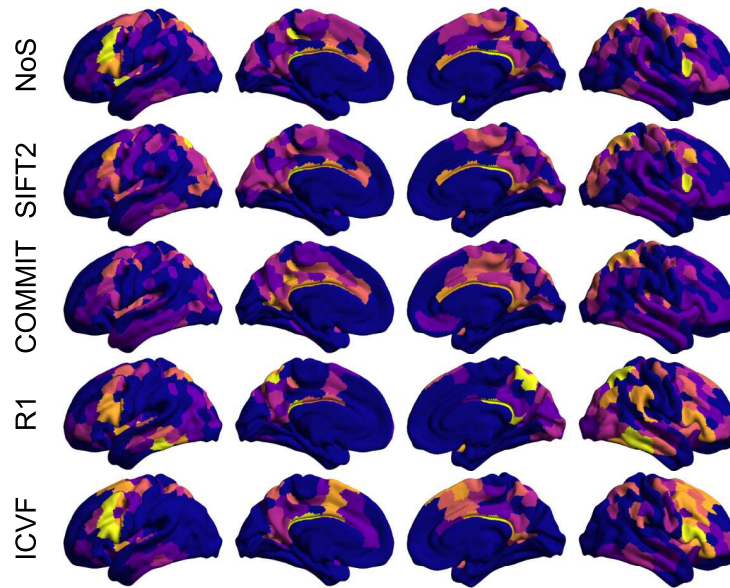


Group Normalized Hubness

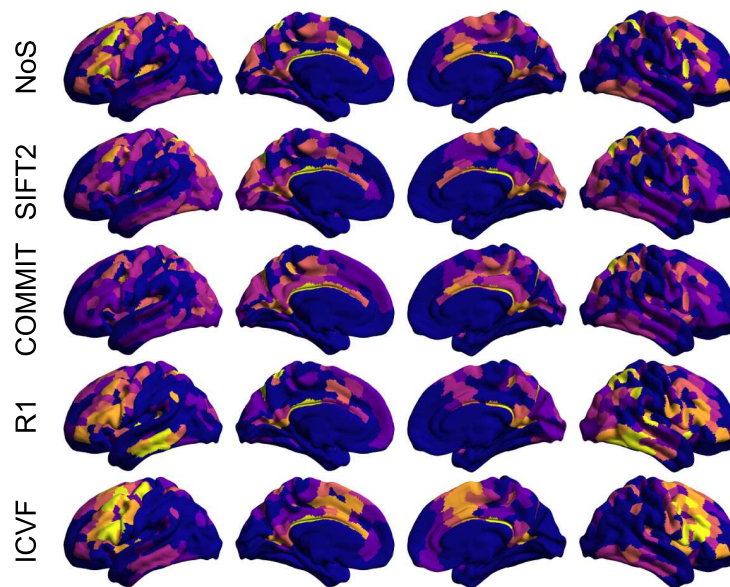
Schaefer-200



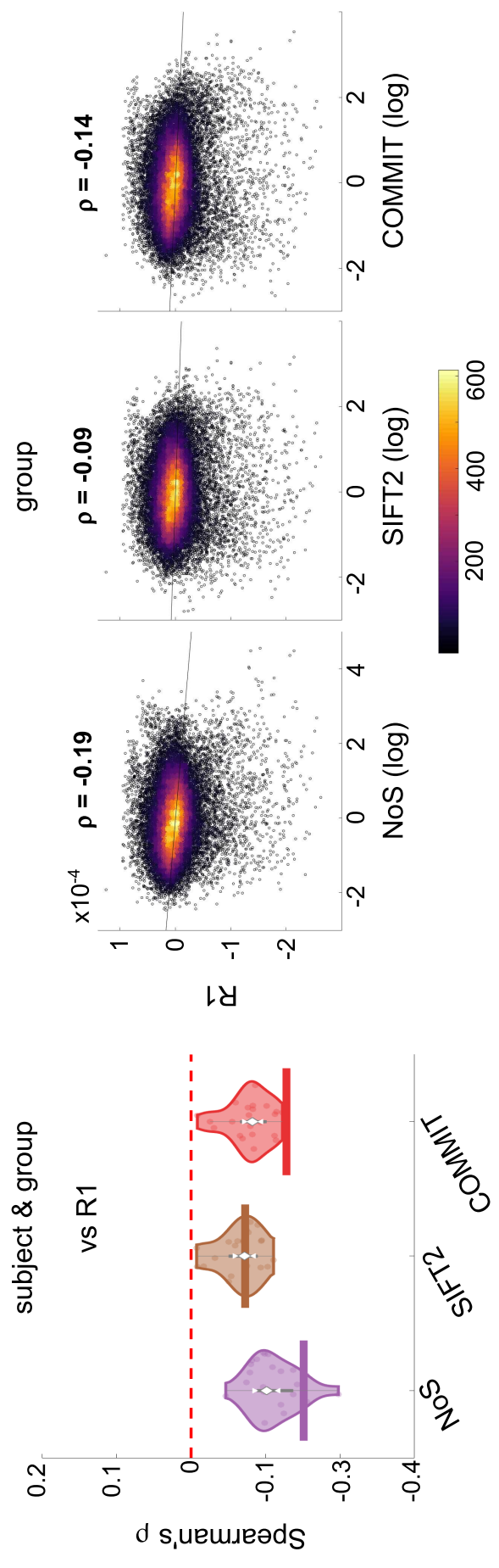
Schaefer-400



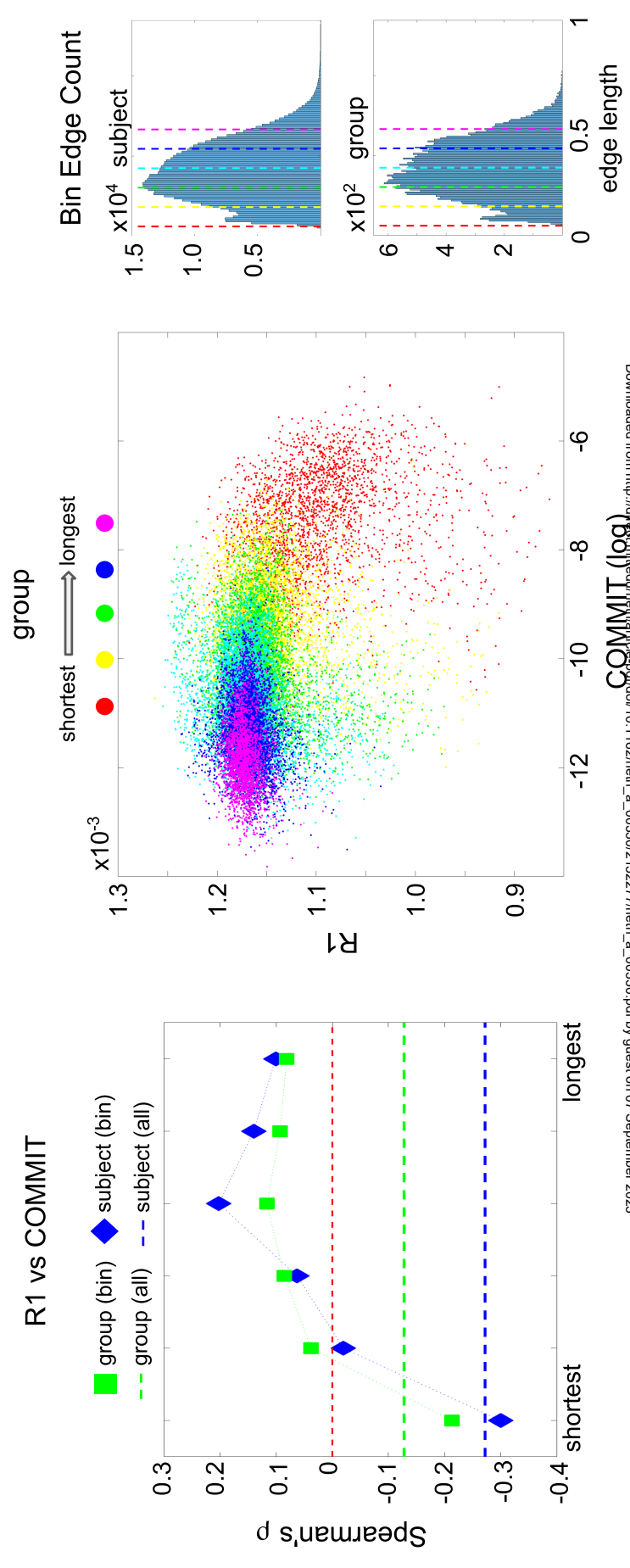
Schaefer-600



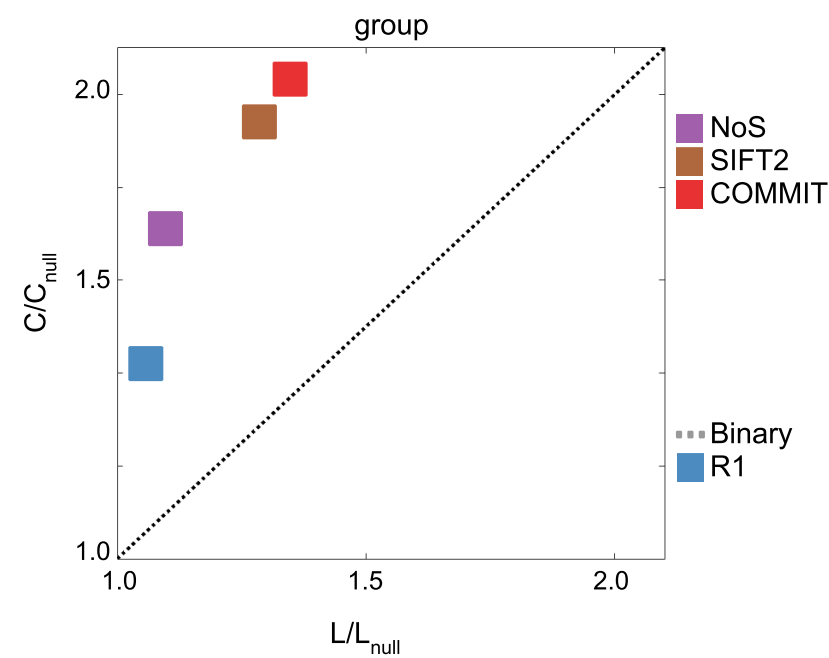
**A** residual edge weight correlations



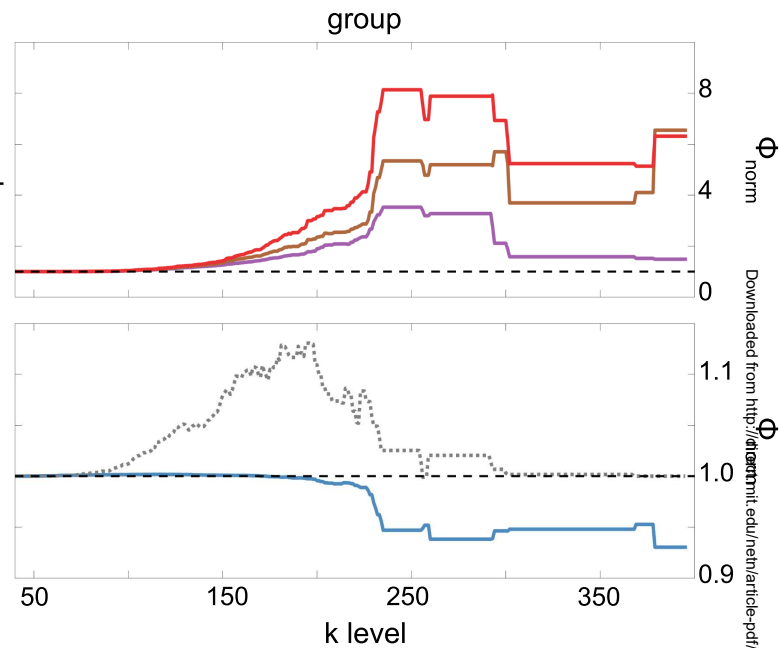
**B** edge weight correlations across edge length bins



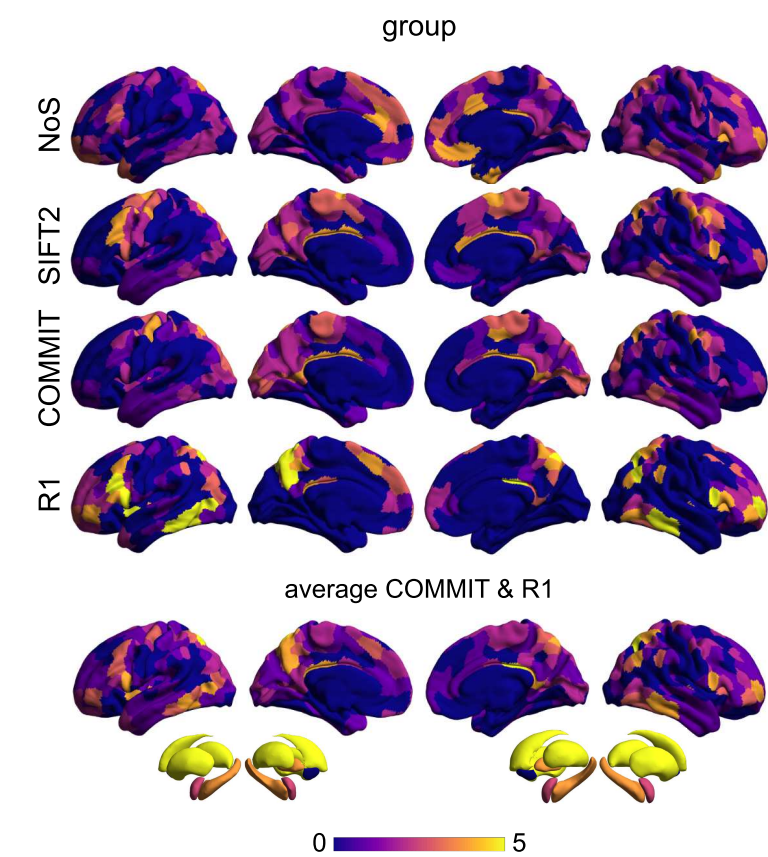
**A** normalized small-worldness



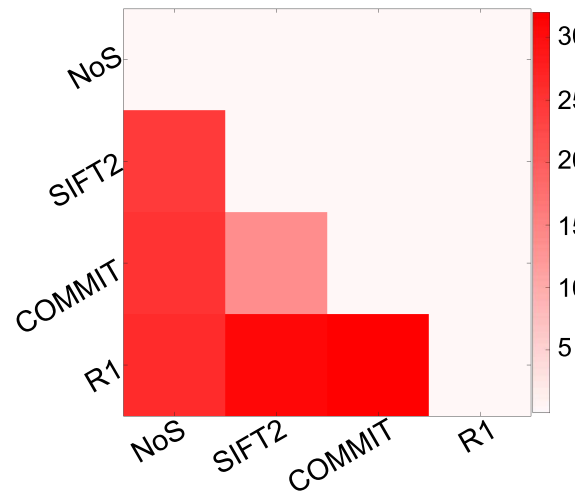
**B** normalized rich club



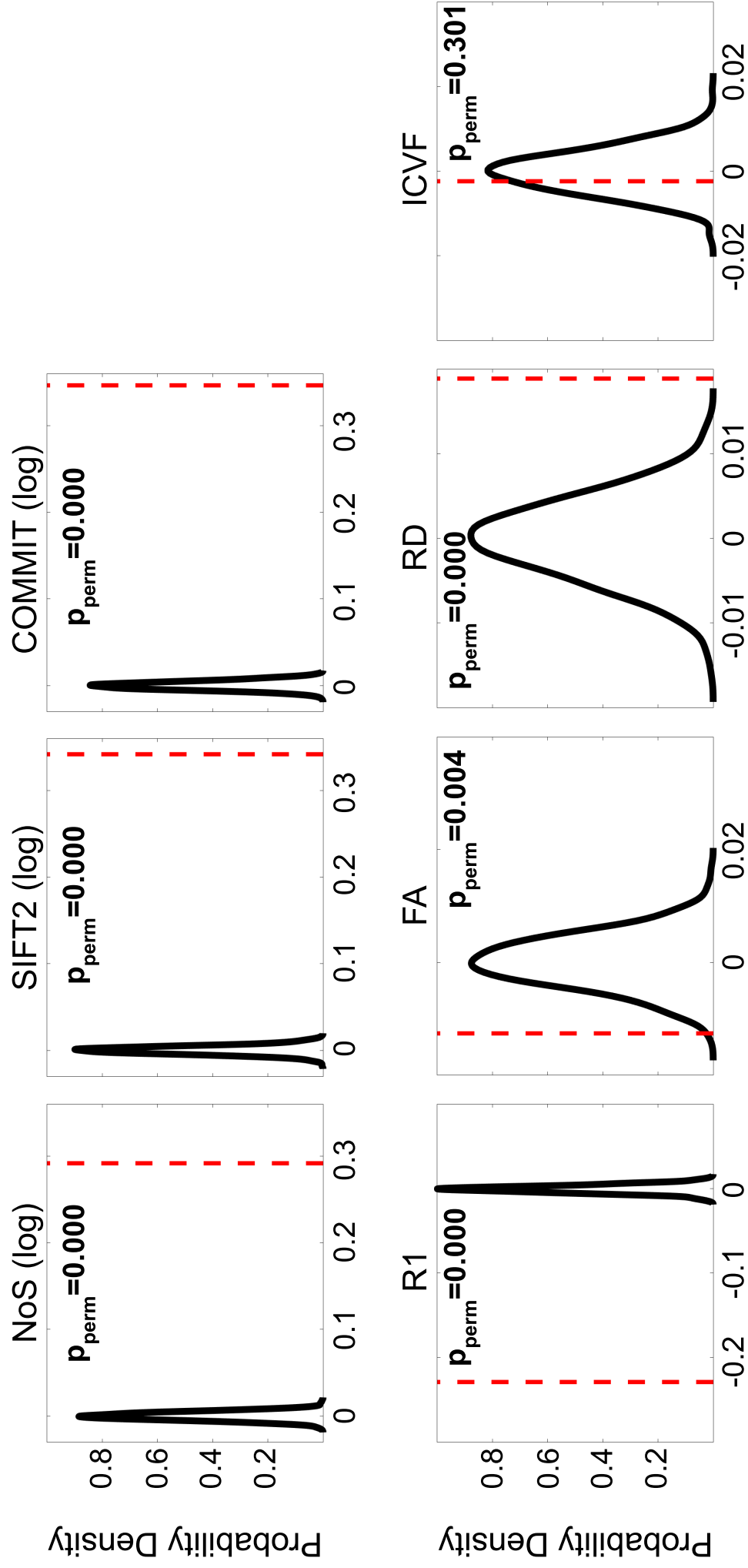
**C** normalized hubness



Hubness Euclidean Distance (group)

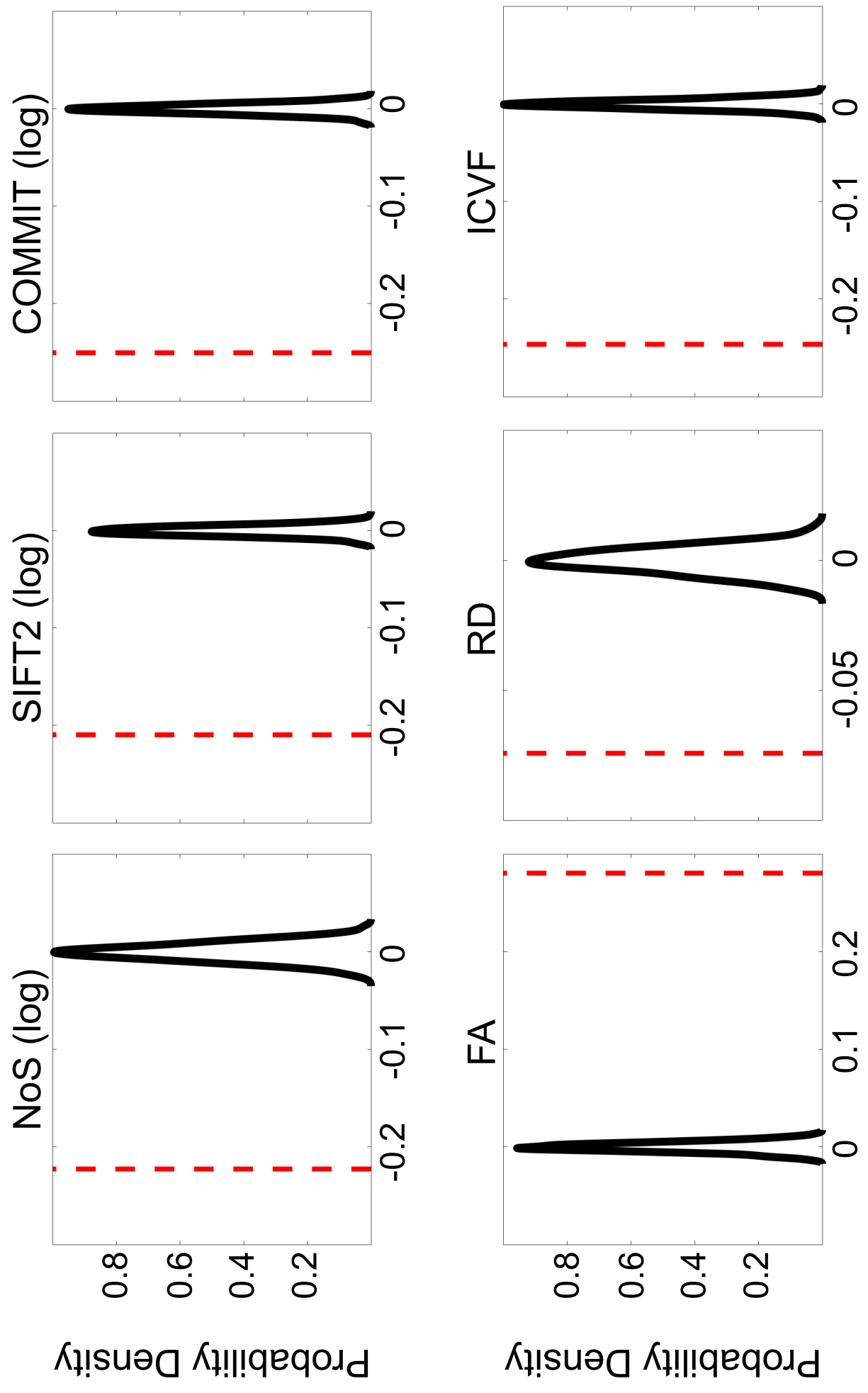


Group Permutation Testing  
Spearman's  $\rho$  with FC  
(edge-length regressed residuals)

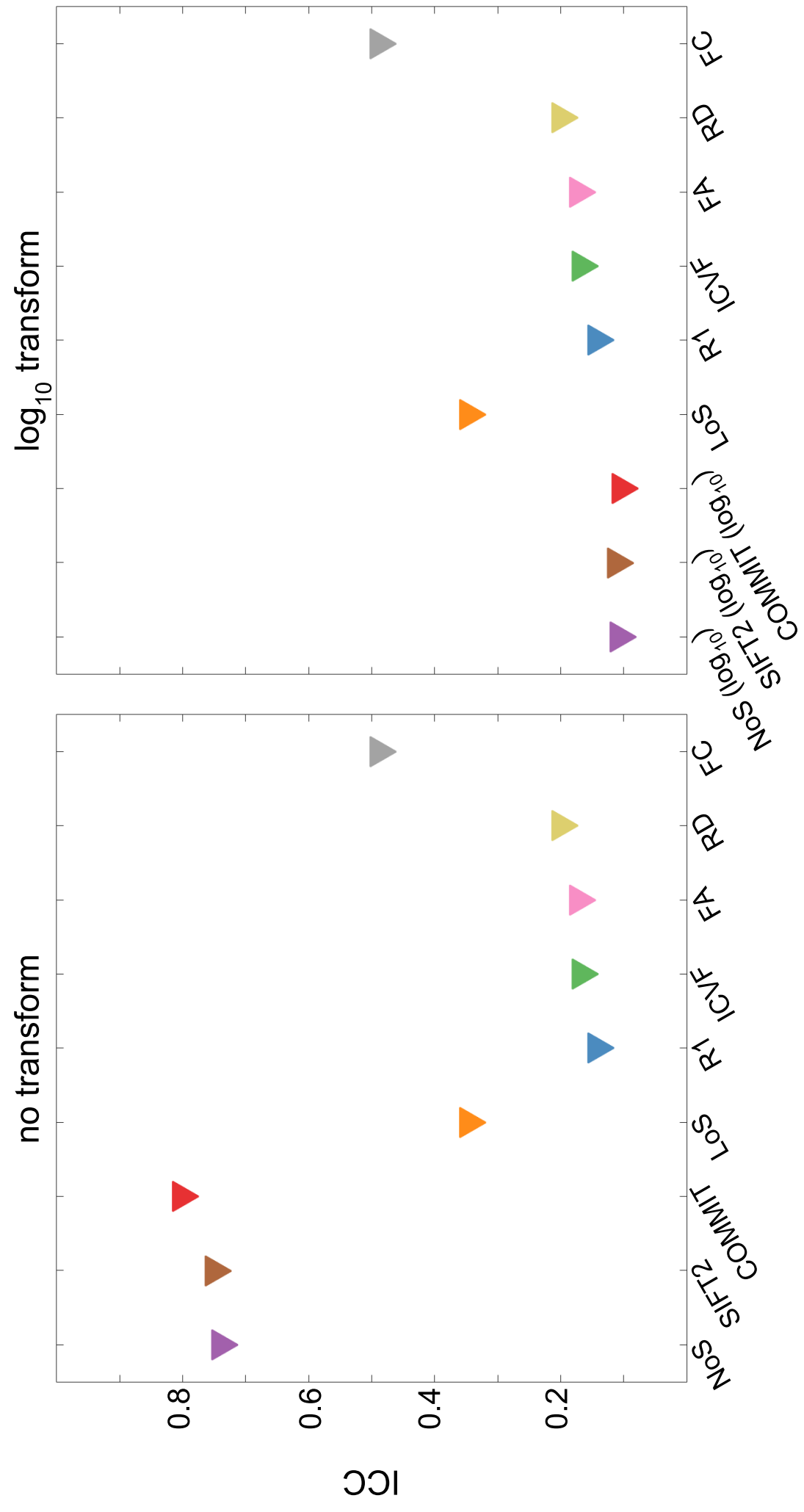


Group Permutation Testing  
Spearman's  $\rho$  with **R1**  
(edge-length regressed residuals)

**All  $p_{\text{perm}} = 0.000$**

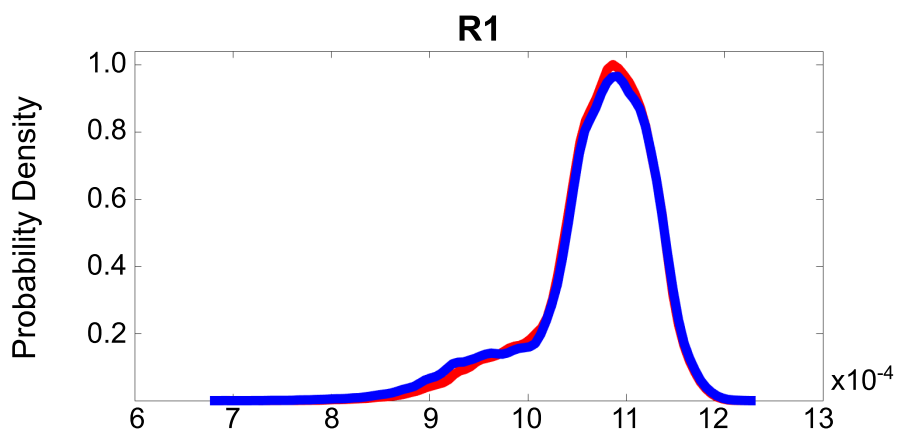
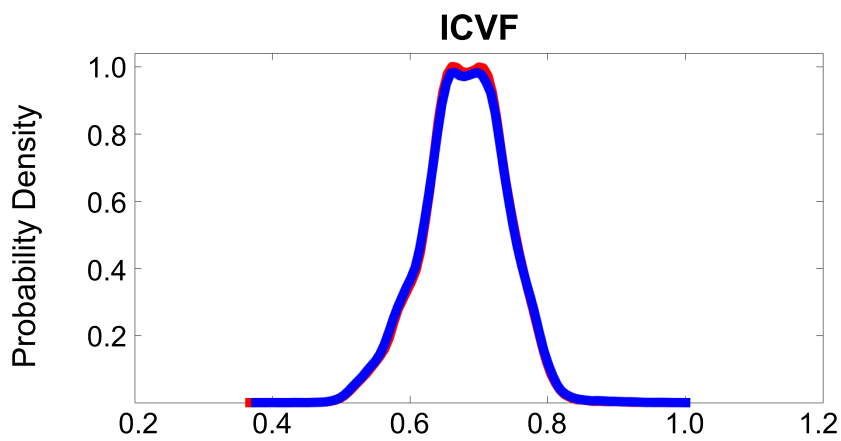
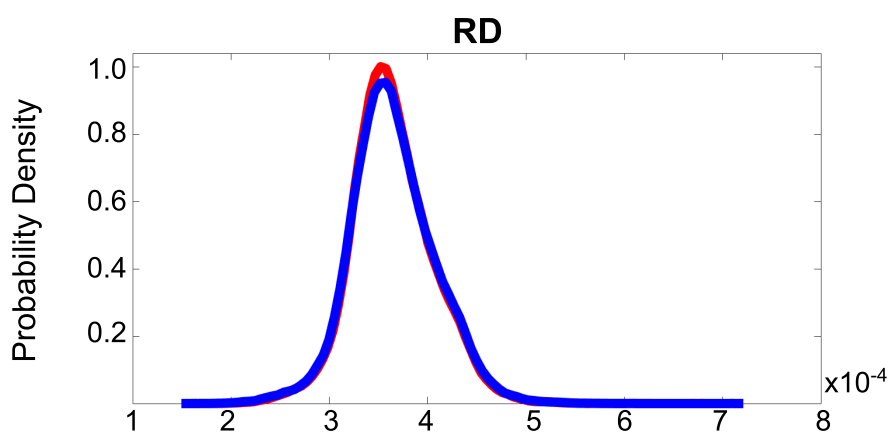
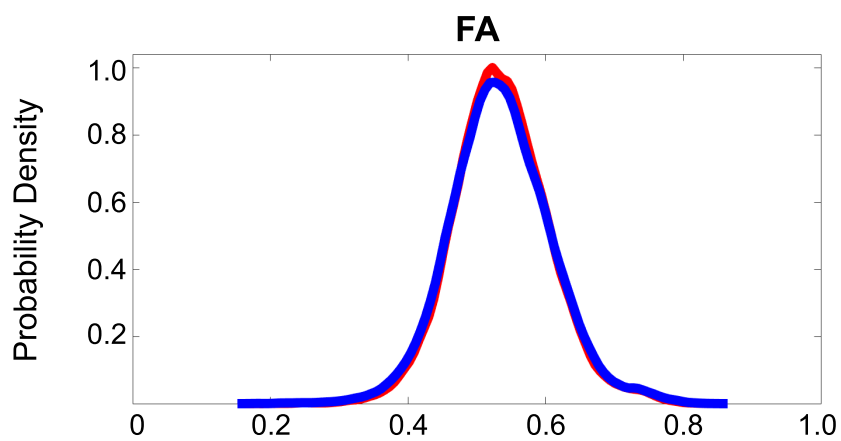


Intraclass Correlation

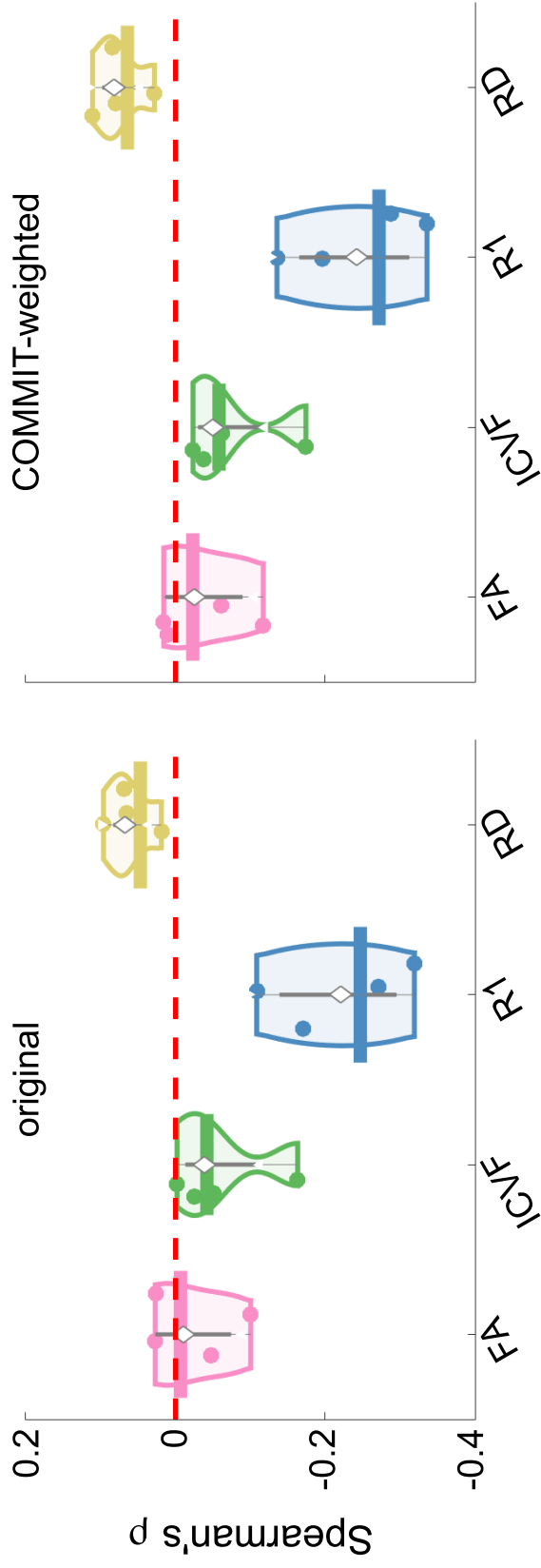


## Subject Edge Weight Distributions

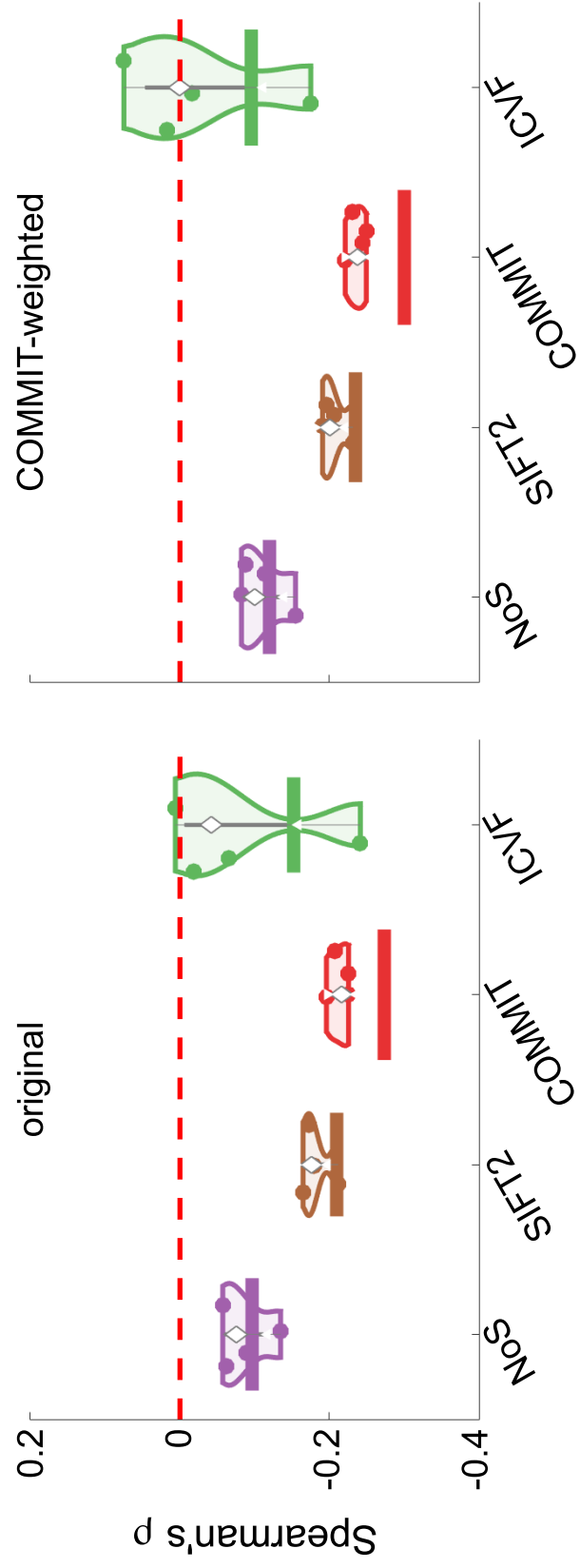
original COMMIT-weighted



**A** residual edge weight correlations with FC

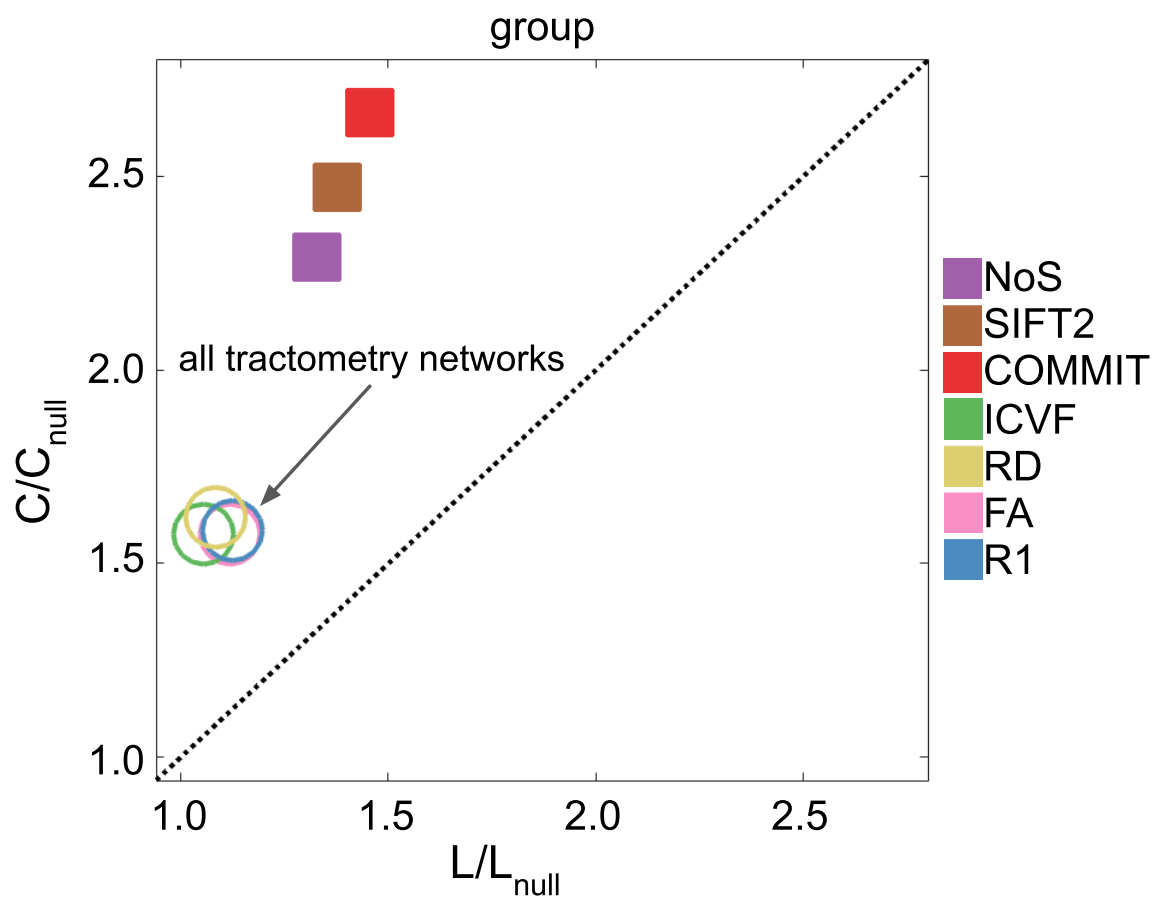


**B** residual edge weight correlations with R1

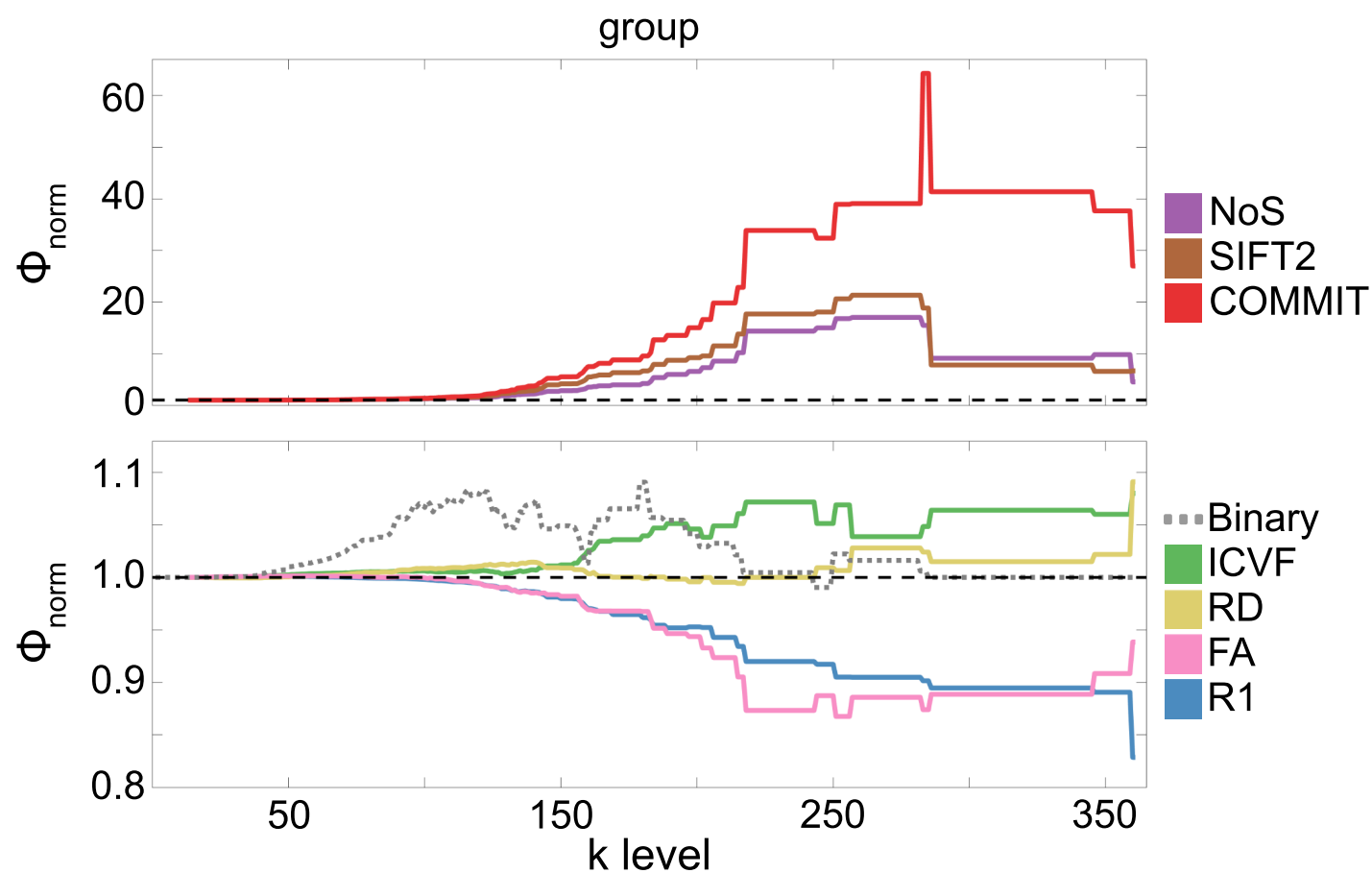




## A normalized small-worldness

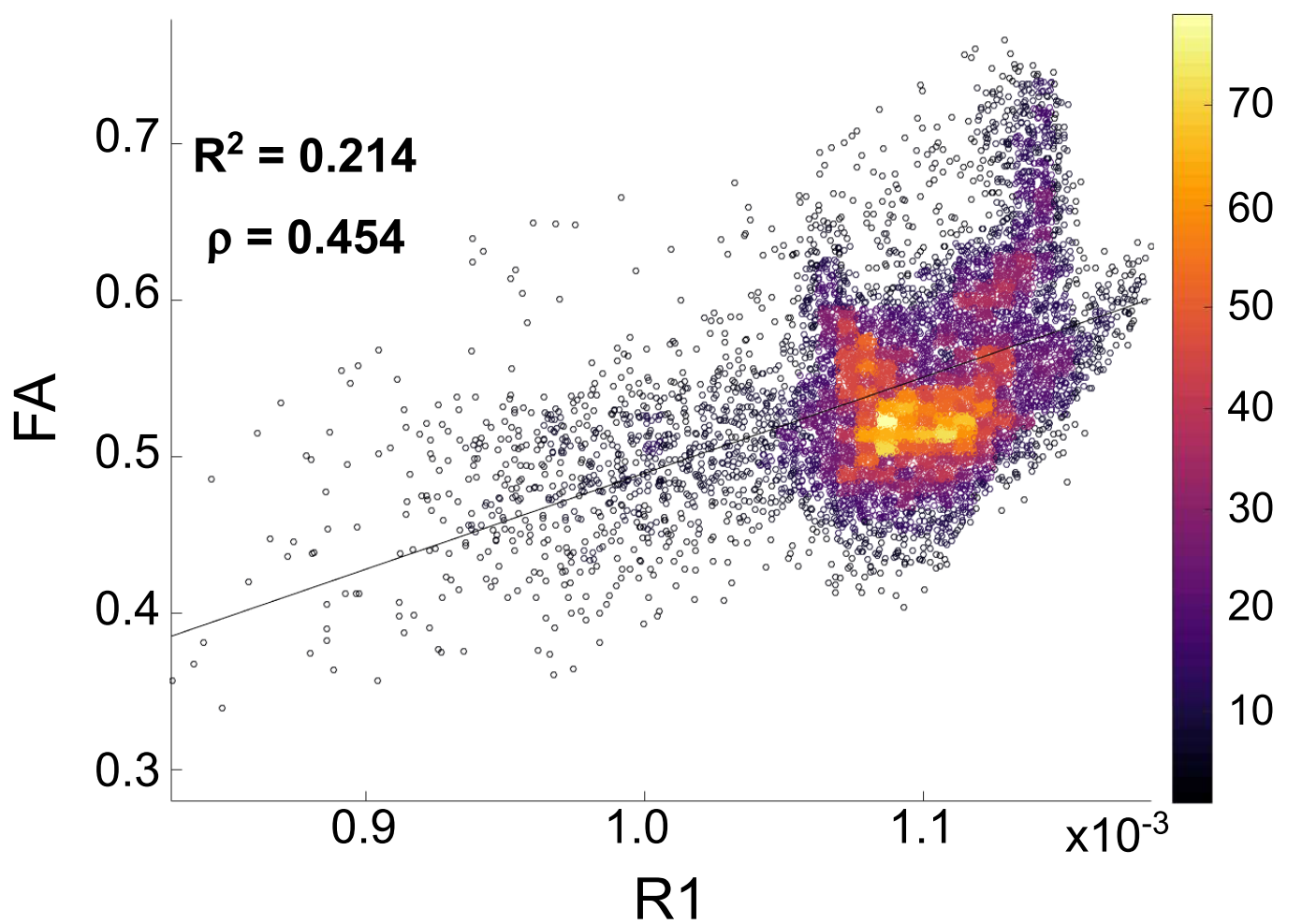
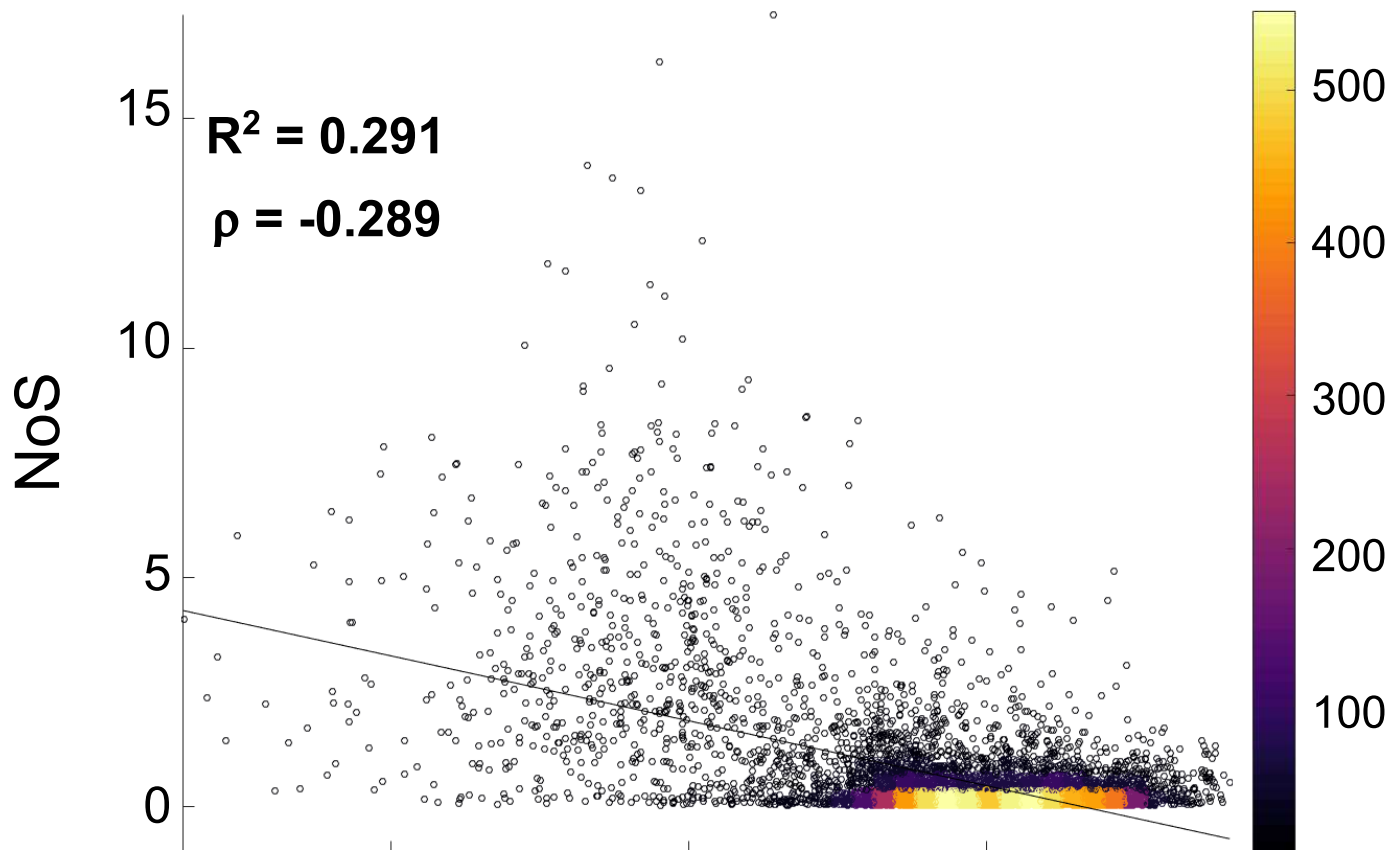


## B normalized rich club



# Edgewise Relationship of Edge Weights (not residuals)

group - Schaefer-200 - cortex only



<u>Short name</u>	<u>Long name</u>	<u>Method</u>	<u>Data source</u>	<u>Interpretation</u>
<b>LoS</b>	Length of Streamlines	streamline-specific	diffusion MRI	Mean length of all streamlines connecting two nodes
<b>NoS</b>	Number of Streamlines	streamline-specific	diffusion MRI	Number of streamlines connecting two nodes; connection strength
<b>SIFT2</b>	Spherical-deconvolution Informed Filtering of Tractograms	streamline-specific	diffusion MRI	Fiber density from spherical deconvolution summed across streamlines; connection strength
<b>COMMIT</b>	Convex Optimization Modeling for Microstructure Informed Tractography	streamline-specific	diffusion MRI	Total intra-axonal cross-sectional area summed across streamlines; connection strength
<b>R1</b>	longitudinal relaxation rate	tractometry	multi-modal (diffusion + relaxometry)	$R_1 = 1/T_1$ ; index of tissue myelin content
<b>FA</b>	Fractional Anisotropy	tractometry	diffusion MRI	Diffusion directional dependence
<b>RD</b>	Radial Diffusivity	tractometry	diffusion MRI	Diffusion perpendicular to the principal axis
<b>ICVF</b>	Intra-Cellular Volume Fraction	tractometry	diffusion MRI	Neurite density

## AUTHOR SUMMARY

For computational network models to provide mechanistic links between brain structure and function, they must be informed by networks in which edge weights quantify structural features relevant to brain function. Here, we characterized several weighted structural networks capturing multiscale features of white matter connectivity including total intra-axonal cross-sectional area and myelin density. We describe these networks in terms of edge weight distribution, variance and network topology, as well as their relationships with each other, edge length and function. Overall, these findings support the joint use of structural networks weighted by the total intra-axonal cross-sectional area and myelin content of white matter tracts in structure-function models. This thorough characterization serves as a benchmark for future investigations of weighted structural brain networks.